Dissertation

submitted to the

Combined Faculty of Mathematics, Engineering and Natural Sciences

of Heidelberg University, Germany

for the degree of

Doctor of Natural Sciences

Put forward by

Daniel Alberto García Calderón

born in: Acapulco, México

Oral examination: 15.05.2024

Investigating Hydrogen Peroxide Production under Different Radiation Modalities in non-small-cell Lung Cancer Cell Lines

Referees:

Prof. Dr. Joao Seco

Prof. Dr. Christian Karger

Abstract

Radiotherapy plays a pivotal role in cancer treatment, mainly relying on reactive oxygen species (ROS) production to induce cell death. This thesis investigates the role of ROS in cellular responses to radiation, focusing specifically on H_2O_2 production. A novel method utilizing NucPE1 fluorescent marker validated H_2O_2 assessment during irradiation. A cell line-dependent variation in H2O2 production were observed for lung cancer cells, correlating with DNA damage and radiosensitivity. Furthermore, the evaluation of H_2O_2 production under different conditions revealed expected trends. Despite encountering challenges, notables advances were made in implementing a high dose rate (HDR) delivery platform. Analysis of cellular redox state demonstrated an inverse correlation with radioresistance, highlighting the complex ROS-cellular response interplay. The investigation also hinted at the potential involvement of the SOD enzyme in radioresistance mechanisms. Looking ahead, future research efforts will explore live-cell imaging techniques, extending predictive potential to diverse conditions, and investigating the role of ROS in FLASH radiotherapy, aiming to advance cancer treatment strategies.

Zusammenfassung

Radiotherapie spielt eine essenzielle Rolle in der Krebstherapie, deren Wirkung hauptsächlich auf dem durch produzierte reaktive Sauerstoffspezies (ROS) induzierten Zelltod basiert. In dieser Dissertation wird die Rolle von ROS in der Zellantwort auf Bestrahlung mit einem Fokus auf die H2O2 Produktion untersucht. Dabei wird mit einer neuartigen Methode mithilfe von NucPE1-Fluoreszenzmarker die H_2O_2 Produktion während der Bestrahlung bestimmt. Es wurden dabei zelllinienabhängige Variationen der H202 Produktion bei Lungenkrebszellen beobachtet, die mit DNS-Schäden und der Radiosensitivität korrelieren. Ebenso zeigte die Auswertung der H_2O_2 Produktion unter verschiedenen Bedingungen erwartete Ergebnisse. Trotz großer Herausforderungen wurden bedeutende Fortschritte bei der Implementierung einer Plattform zur Bestrahlung mit hohen Dosisraten (HDR) erzielt. Die Analyse des zellulären Redoxstatus wies auf eine inverse Korrelation zur Strahlenresistenz hin und unterstreicht das komplexe Wechselspiel zwischen den ROS und der zellulären Antwort. Weitere Untersuchungen deuten auf einen Einfluss des SOD-Enzyms auf die Radioresistenz. Mithilfe der zukünftigen Entwicklung von Echtzeit-Bildgebung auf Zellebene werden die Vorhersagemöglichkeiten unter verschiedenen Bedingungen erweitert und die Rolle von ROS in FLASH Radiotherapie kann tiefgründiger untersucht werden, mit dem Ziel, Krebsbehandlungen zu verbessern.

Contents

Chapter 1

Theoretical Background

Radiotherapy (RT), also referred to as radiation therapy, is a critical component of cancer treatment. RT uses various forms of ionizing radiation such as photons, electrons, protons, carbon, and, recently, helium ions to induce localized damage in biological targets through direct interaction with target molecules or indirect production of reactive species from water radiolysis or other molecules. This Chapter lays the foundation for a comprehensive exploration of radiotherapy, which will be structured according to the time-scale of the different effects of the radiation in biological systems: physical, chemical, and biological (Figure 1.1). Within this framework, the basic concepts involved in radiation effects in biological systems will be presented, divided into three distinct components: radiotherapy physics, radiotherapy chemistry, and radiation biology. Additionally, in the last part of this section, a few modern topics in radiotherapy will be discussed, particularly the current popular topic of FLASH RT.

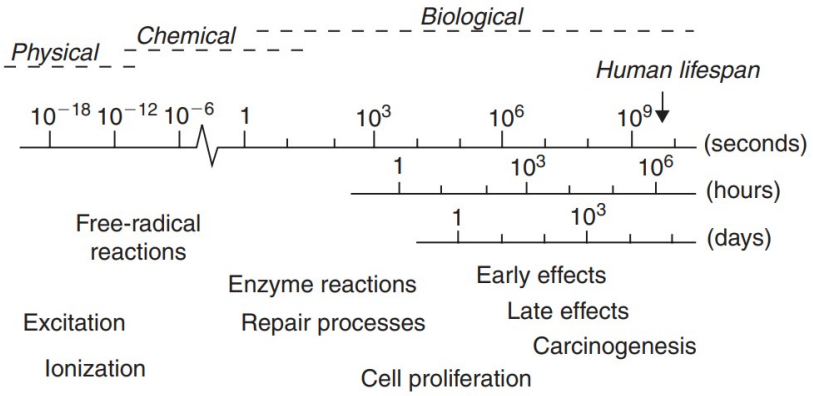

Figure 1.1: Chronology of the radiation induced effects on biological systems. Image was taken from [1].

1.1 Radiotherapy Physics

1.1.1 Interactions of Radiation with Matter

Photons

Photons utilized in cancer treatment are primarily generated through electron linear accelerators (LINACs). These high-energy beams, upon interaction with bodily tissues or other absorbing materials, undergo complex processes resulting in the deposition of energy within the target.

The primary interaction occurs when photons collide with electrons within the material, leading to phenomena such as scattering and electrons ejected from the atomic orbits. As these liberated electrons traverse through the absorber, they induce ionization, excitation of atoms, and disruption of molecular bonds. These interactions contribute to the biological damage inflicted on tissues.

Four primary processes govern photon interactions with matter: coherent Rayleigh scattering, photoelectric absorption, Compton scattering, and pair production.

Regardless of the interaction mechanism, the intensity I of the photon beam diminishes exponentially with increasing depth (d) within the target material, as described by the Lambert-Beer Law [2]:

$$I = I_0 e^{-\mu d}, \tag{1.1}$$

where, μ represents the total attenuation coefficient. This coefficient is the sum of the individual cross-sections of the interaction processes:

$$\mu = \sigma_{coh} + \tau + \sigma_c + \pi, \tag{1.2}$$

here, σ_{coh}, τ, σ_c, π are attenuation coefficients for coherent Rayleigh scattering, photoelectric absorption, Compton scattering and pair production, respectively. In Figure 1.2, the contributions of the individual cross-sections can be seen.

The Coherent Rayleigh scattering involves an electromagnetic wave passing close to an electron, causing the electron to briefly oscillate. This phenomenon requires that the electron's size is considerably smaller than the wavelength (λ) of the incoming radiation. Subsequently, the oscillating electron emits radiation of the same wavelength as the

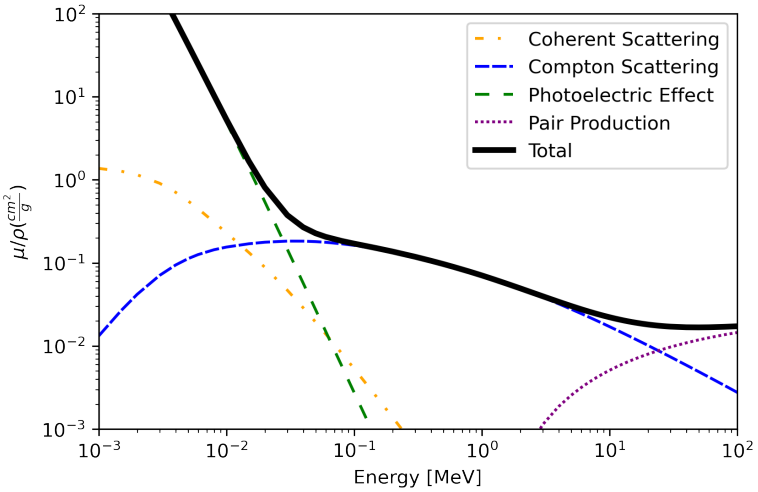

Figure 1.2: Mass attenuation coefficients (μ/ρ in water. Data taken from [3]

incident radiation. Therefore, during this process no photon energy is converted into kinetic energy; instead, all of it is scattered.

In the photoelectric effect, a photon interacts with an inner shell electron of a target atom. If the energy of the photon exceeds the binding energy of the electron, the electron is released from the atom, leaving behind a positively charged atom. Following the release of the electron from the atom, a vacancy is generated within the shell, thereby placing the atom in an excited state. This vacancy can be filled by an electron from an outer orbital, leading to the emission of a characteristic x-ray.

In Compton scattering, a photon interacts with an atomic electron, weakly bound to the atom, causing the electron to absorb energy and be emitted at an angle θ, while the photon is scattered at an angle ϕ. This process occurs when the photon energy (E_γ) greatly exceeds the binding energy (E_B) of the electron. Unlike in the photoelectric effect, where the photon energy is entirely absorbed, only a fraction of it is transferred to the electron in Compton scattering, resulting in the emission of an electron with kinetic energy (E_{kin}). Consequently, Compton interaction ionizes the atom, potentially leading to further electron rearrangements within its shells.

The energy of the scattered photon (E'_γ) is described by the formula:

$$E'_\gamma = \frac{E_\gamma}{1 + \frac{E_\gamma}{m_e c^2}(1 - \cos\theta)}, \tag{1.3}$$

where m_e represents the electron mass, c is the speed of light, and θ denotes the scattering angle.

Pair production refers to the process in which a photon generates the creation of an electron-positron pair e^-e^+ near a nucleus X. To initiate this process, the energy of the photon must exceed a threshold of $E_\gamma \geq 2m_ec^2 = 1.022$ MeV. The excess energy beyond $2m_ec^2$ is distributed between the kinetic energies of the resulting positron and electron. Following the production, the ejected positron can traverse the medium and undergo annihilation with an electron, emitting two 511 keV photons.

Charged Particles

When charged particles travel through a material, they interact via Coulomb forces with the shell electrons or nuclei of the target, predominantly through elastic or inelastic collisions. Additionally, scattering phenomena within the nuclear field may occur, potentially resulting in bremsstrahlung emission, especially observed in lighter charged particles like electrons. Direct nuclear interactions with the nucleons of the target are also possible. Charged particles traversing a material travel a finite distance, determined by the gradual dissipation of their energy. This loss is quantified by the stopping power, defined as the expected rate of kinetic energy loss per unit path length, denoted as $S = \frac{dE}{dx}$, measured in J/m or MeV/cm.

For heavy charged particles with β in the range from 0.02 to 0.99, where $\beta = \frac{v}{c}$, moving through an absorber material characterized the atomic number Z, atomic weight A, and mean excitation energy I the stopping power is described by the Bethe-Bloch formula:

$$-\frac{dE}{dx} = Kz^2\frac{1}{\beta}\frac{Z}{a}\left[\frac{1}{2}ln\left(\frac{2m_ec^2\beta^2W_{max}}{I^2}\right) - \beta^2 - \frac{C}{Z} - \frac{\delta}{2}\right] \tag{1.4}$$

where $K = \frac{4\pi e^4}{m_ec^2}N_A = 0.31$ MeV $\frac{cm^2}{g}$, involving the particle parameters charge z, velocity β, and maximal possible energy transfer $W_{\max}$. Additionally, the formula includes two correction terms: the $\frac{C}{Z}$-term, addressing interactions with inner-shell electrons at various excitation potentials, and the δ-term, rectifying for the density effect attributable to dipole distortion of atoms near the trajectory of the projectile.

When the incident particles are electrons, the Bethe-Bloch formula cannot be directly applied and instead, energy transfers to atomic electrons are described by the Møller cross section [4]. In addition, electrons are extremely light, therefore the energy loss due

to radiative processes like bremsstrahlung during deceleration within the nuclear field cannot be ignored. Thus, the stopping power of electrons includes both collisional and radiative components:

$$S_{total} = -\left(\frac{dE}{dx}\right)_{total} = \left(\frac{dE}{dx}\right)_{col} + \left(\frac{dE}{dx}\right)_{rad} \tag{1.5}$$

1.1.2 Physical Quantities in Radiotherapy

Dose

In RT, an essential physical quantity is the absorbed dose (D). According to the International Commission on Radiation Units Measurements [5], the absorbed dose is defined as the mean energy imparted ($d\bar{\epsilon}$) by ionizing radiation to matter of mass dm:

$$D = \frac{d\bar{\epsilon}}{dm}, \tag{1.6}$$

given in the unit Gray (Gy, 1 Gy = 1 J/kg).

Therefore, dose rate ($\dot{D}$) is given by the time derivative:

$$\dot{D} = \frac{dD}{dt} = \frac{d}{dt}\left(\frac{d\epsilon}{dm}\right) \tag{1.7}$$

The absorbed dose represents a non-stochastic quantity applicable for both indirectly and directly ionizing radiations [2]. In the case of indirectly ionizing radiations, the energy deposition occurs initially to secondary charged particles. Subsequently, these charged particles transfer some of their kinetic energy to the surrounding medium, resulting in absorbed dose, while also experiencing energy loss in the form of radiative losses.

LET

Linear Energy Transfer (LET) is a quantity that characterizes the interaction of radiation with matter. It quantifies the mean energy lost by the charged particles due to electronic interactions in traversing a distance dl, minus the mean sum of the kinetic energies in excess of Δ of all the electrons released by the charged particles [5]:

$$LET_{\Delta} = \frac{dE_{\Delta}}{dl} \tag{1.8}$$

The LET can be expressed in units of kilo-electron volts per micrometer (keV/μm). The concept of LET is useful in understanding the ionization density induced by radiation in a target.

The LET value varies depending on the radiation quality and the material traversed. For instance, densely ionizing radiation creates compact and dense particle tracks of ionization, resulting in higher LET values. Conversely, sparsely ionizing radiation produces spread-out particle tracks, leading to lower LET values. Radiation with low LET, such as x-rays, has a relatively low energy transfer rate per unit length of the particle track. On the other hand, high LET radiation, like alpha particles and heavy ions, exhibit a higher energy transfer rate, resulting in more efficient ionization and increased biological damage potential.

It is important to note that the definition of LET differs slightly depending on the context. In the case of charged particles,the LET is straightforwardly defined as the energy transfer rate along the particle track. However, when considering photons, the LET is expressed as the average of the secondary electrons produced by photon interactions.

1.1.3 Percentage Depth Dose

The difference in energy deposition between various particles becomes evident when examining their energy loss characteristics while traversing a material. This phenomenon is best illustrated through depth dose curves, which showcases the dependence in absorbed dose as a function of depth (Figure 1.3).

Photons interact with matter via indirect ionization processes, mainly by producing secondary electrons that are responsible for the energy deposition. Due to the predominance of secondary electron interactions, photons exhibit an exponential attenuation of dose with increasing depth. The exponential decrease in dose with increasing depth is accompanied by a characteristic buildup effect near the surface. The dose buildup occurs because high-energy photon beams eject high-speed electrons from the medium's surface and the subsequent layers. These electrons deposit their energy as they travel until they are stopped, resulting in an increase in absorbed dose with depth until a maximum is

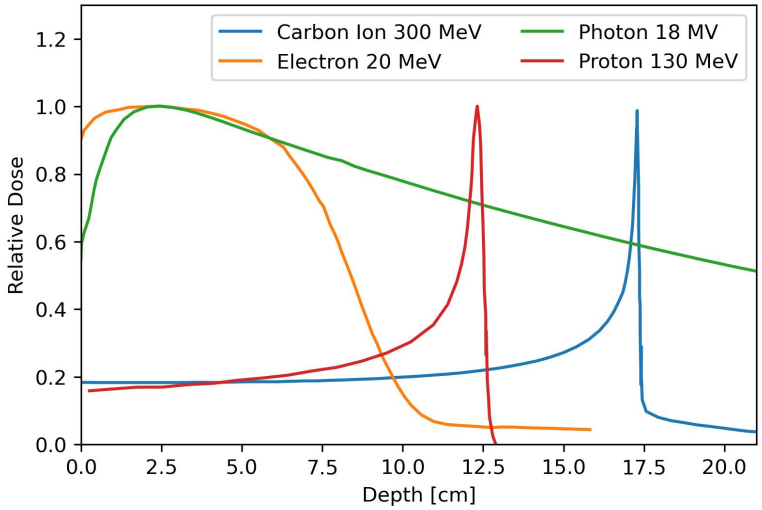

Figure 1.3: Depth dose curves for different radiation qualities. Dose distributions as a function of depth in water. Modified from [6].

reached. After this point the dose starts to decrease due to the diminishing production of electrons [7].

In contrast to photons, electrons interact directly with the atoms of the medium. Contrary to photon beams, the skin-sparing effect of clinical electron beams is minimal or non-existent. This difference is primarily because the surface dose percentage for electron beams increases with their energy [7]. This behavior can be traced back to the electrons scattering characteristics. At lower energies, electrons scatter more easily and at larger angles. Therefore, the dose accumulation occurs more rapidly and within a shorter distance from the surface. Consequently, the surface dose to maximum dose ratio is lower for lower-energy electrons than for those with higher energies.

Protons and carbon ions both exhibit a Bragg peak [8] where they deposit the majority of their energy, causing a significant increase in dose that sharply decreases afterward, thus limiting the radiation dose to healthy tissues beyond this position. Carbon ions, due to their heavier nature, also have a fragmentation tail beyond the Bragg peak, where they break into smaller particles that continue to deposit energy. Additionally, carbon ions experience less multiple Coulomb scattering and have a narrower lateral penumbra and Bragg peak compared to protons [9], which improves their precision in delivering the dose.

1.2 Radiotherapy Chemistry

The chemical stage (Figure 1.1) encompasses the time-frame during which the atoms and molecules in the medium undergo rapid chemical reactions with other components within the cell. The process of ionization and excitation results in the damage of chemical bonds, creating unstable molecules known as *free radicals* [1]. Given that approximately 80% of the cell mass is composed by water, the chemical reactions triggered by radiation are described by the water radiolysis (Figure 1.4).

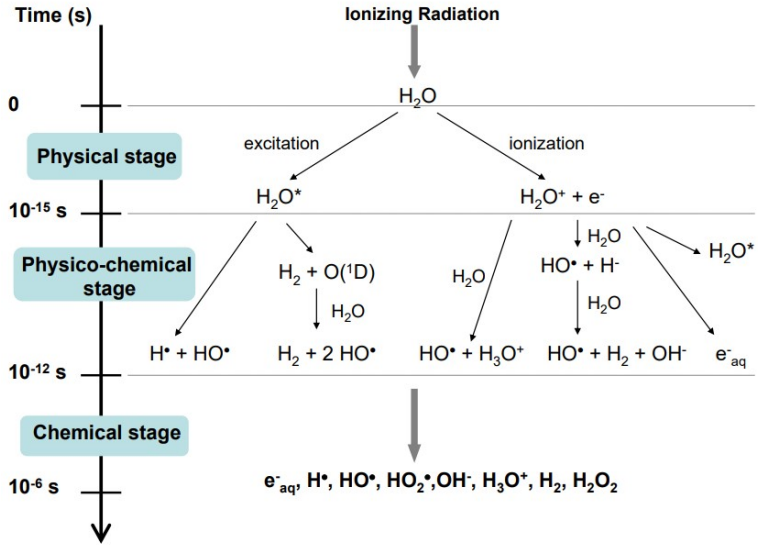

Figure 1.4: Chemical reactions following irradiation in water. The image was taken from [6]

1.2.1 Water Radiolysis

Water radiolysis starts by the ionization and excitation of the water molecules [10]:

$$H_2O \xrightarrow{IR} H_2O^+ + e^- \tag{1.9}$$

$$H_2O \xrightarrow{IR} H_2O^*, \tag{1.10}$$

next, the water radical cation loses a proton to the surrounding water molecules:

$$H_2O^+ + H_2O \longrightarrow H_3O^+ + \cdot OH, \tag{1.11}$$

meanwhile, the electron becomes solvated very rapidly:

$$e^- + nH_2O \longrightarrow e^-_{aq}, \tag{1.12}$$

then the excited water molecules formed in reaction 1.10 can break up into hydrogen atoms and OH radicals:

$$H_2O^* \longrightarrow H\cdot + \cdot OH, \tag{1.13}$$

these reactive species react with each other within the spur or diffuse into the rest of the solution, followed by the reaction of the solvated electrons with protons to produce H-atoms:

$$e^-_{aq} + H^+ \longrightarrow H\cdot. \tag{1.14}$$

Hydrogen molecules (H_2) and hydrogen peroxide (H_2O) are then produced by the following reactions:

$$H\cdot + H\cdot \longrightarrow H_2 \tag{1.15}$$

$$e^-_{aq} + e^-_{aq} + H_2O \longrightarrow H_2 + 2\,OH^- \tag{1.16}$$

$$\cdot OH + \cdot OH \longrightarrow H_2O_2. \tag{1.17}$$

Most of the radicals formed in the spur are then converted to water, following:

$$H\cdot + \cdot OH \longrightarrow H_2O, \tag{1.18}$$

and to hydroxide ions,

$$e^-_{aq} + \cdot OH \longrightarrow OH^- \tag{1.19}$$

and protons and hydroxide ions eventually neutralize each other:

$$H^+ + OH^- \longrightarrow H_2O \tag{1.20}$$

All the reactions described above are diffusion driven [10]; further information about reaction rates can be found in Table 1.1. If these radicals reach the cells sensitive targets,

such as the DNA, it can lead to cell death, this effect is called indirect action of radiation, and will be described in the next section.

Table 1.1: Rate constants of some of the reactions described in the water radiolysis description. Reaction rates (k) extracted from [10].

Reactants	Product	k [$10^{10} dm^3 mol^{-1} s{-}1$]
$e^-_{aq} + H^+$	$H\cdot$	2.2
$H\cdot + H\cdot$	H_2	1
$e^-_{aq} + e^-_{aq} + H_2O$	$H_2 + 2\,OH^-$	0.5
$H\cdot OH + \cdot OH$	H_2O_2	0.6
$H\cdot + \cdot OH$	H_2O	2
$e^-_{aq} + \cdot OH$	OH^-	3

1.3 Radiation Biology

The cell is the fundamental unit of life [11]. Mammalian cells are eukaryotic cells, this kind of cells are encased by a membrane consisting of two layers of lipids (Figure 1.5). Inside the cell, different membrane-bound regions, referred to as organelles, organize the cellular interior.

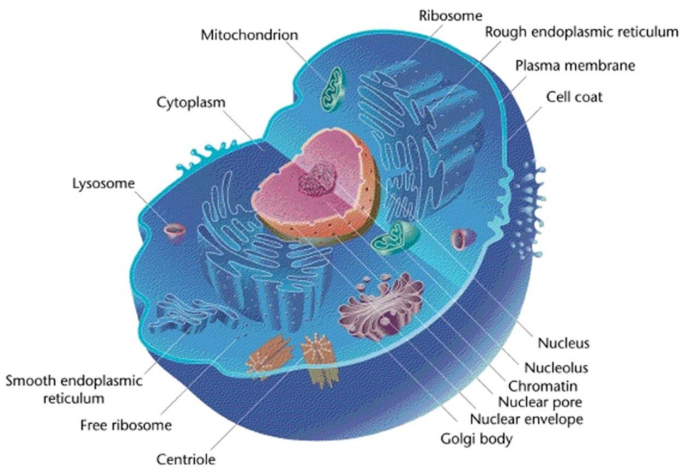

Figure 1.5: Illustratoin of a eukaryotic cell. Image credits: Eukaryotic Cell, Mediran, CC BY-SA 3.0

The nucleus is especially crucial for radiotherapy, given that is where most of the deoxyribonjucleic acid (DNA) is located. The DNA consists of two long helical strands twisted around a shared axis, creating a double helix shape. The strands of DNA are built from monomers known as nucleotides, which are frequently referred to as bases due to their composition, which includes cyclic organic bases.

Near the nucleus is the Endoplasmic Reticulum (ER), a network of membranes that comes in two forms: smooth and rough. The smooth ER is mainly involved in the production of lipids, which are necessary for creating new cell membranes. In contrast, the rough ER, named after the ribosomes attached to its surface, is connected to the nuclear membrane and is responsible for the production, folding, and modification of various proteins [12].

Another crucial organelle for the cell is the mitocondrion. In them the adenosine triphosphate (ATP) is generated, effectively functioning as the cell's power plant.

1.3.1 Radiation induced cell damage

All organelles are susceptible to radiation induced damage. Nevertheless, the impact of radiation on cells is primarily attributed to DNA damage. Ionizing radiation has the capability to directly interact with the atoms of the target, leading to ionization and triggering a sequence of events that result in biological damage. This process, known as the direct action (Figure 1.6) of radiation [13], is predominant in radiations with high LET. Additionally, ionizing radiation can interact with cellular molecules (especially water), generating free radicals. These free radicals, characterized by their unpaired electrons and high chemical reactivity, can travel some distance to interact with vital biological targets, causing the indirect damage [14].

Additionally, cells contain small amounts of metals like iron and copper. Copper has been found in proteins that form the structure of the DNA, however, it has not been detected freely inside the cell. The amount of labile iron inside cells is very small. There is still no consensus whether iron, copper, or both contribute to DNA damage when cells are exposed to [15]. A key process in this context is the Fenton reaction, where iron acts as a catalyst in the presence of H_2O, leading to the production of hydroxyl radicals, which are highly reactive and damaging species [14]. The hydroxyl radicals generated can attack DNA, proteins, and lipids, causing significant cellular damage [15]. Copper is also involved in reactions that can lead to oxidative stress and subsequent DNA damage. Copper can participate in redox cycling, where it alternates between its oxidized (Cu(II))) and reduced (Cu(I)) states. In the presence of H_2O, this redox cycling can produce hydroxyl radicals similarly to the Fenton reaction, albeit less efficiently.

It is established that radiation can cause a broad range of DNA damage, including

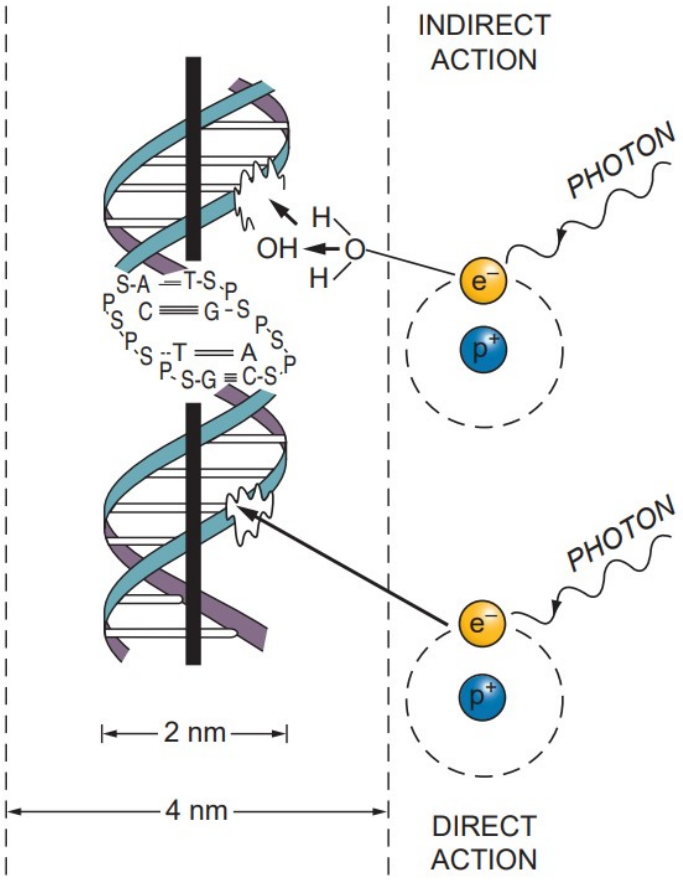

Figure 1.6: Direct and indirect actions of radiation. Image taken from [13]

alterations to nucleotide bases, single-strand breaks (SSBs), and double-strand breaks (DSBs) [10]. It is estimated that the number of DNA lesions per cell immediately after 1 Gy is approximately 1000 SSBs and 40 DSBs [13]. These types of radiation-induced DNA damage are crucial for understanding how radiation leads to cell death, changes in cell properties, and cancer, by causing mutations in genes and abnormalities in chromosomes.

The study of the effect of radiation on DNA suggests a contrast in the relevance of single-strand breaks and double-strand breaks to cellular viability. SSBs, often resulting from interactions with deoxyribose hydrogens and further facilitated by the presence of oxygen, are usually not critical in mammalian cells due to the their ability to repair most SSBs via DNA ligation [10]. However, DSBs represent a far more severe threat. DSBs challenge genomic integrity significantly. Unrepaired or improperly repaired DSBs lead to chromosomal abnormalities, potentially causing gene disruption, cell malfunction, and death [16]. Unlike SSBs, DSBs are considered the most severe radiation-induced lesions due to their potential to trigger mutations and cancer. Furthermore, DSBs occur not

only from external insults but also naturally during cellular processes such as oxidative metabolism, DNA replication, and the production of antibodies, emphasizing the critical need for effective repair mechanisms to maintain cellular and genetic stability [17].

1.3.2 Damage repair pathways

Cells possess an array of sophisticated repair mechanisms to protect their genetic information and ensure their proper functioning. These mechanisms are crucial for repairing various forms of DNA damage, ranging from single and double-strand breaks to base damage.

Homologous recombination (HR) and nonhomologous end joining (NHEJ) are the primary strategies employed to repair DSBs. HR is a precise repair process that uses a matching DNA sequence from an undamaged chromosome or sister chromatid as a template to accurately repair the break, ensuring genetic fidelity is maintained [13]. On the other hand, NHEJ offers a quicker but more error-prone solution for rejoining DSBs without the need for a template, making it the preferred method in mammalian cells for its balance between speed and accuracy [17].

For addressing base damage, cells rely on the Base Excision Repair (BER) pathway. BER targets incorrect or damaged bases, initiating repair with the removal of the faulty base by a specific enzyme, followed by the extraction of the sugar fragment, insertion of the correct nucleotide by DNA polymerase, and ligating the strand by DNA ligase III–XRCC1 [13]. This pathway is crucial for correcting single-base errors, efficiently preventing mutation accumulation.

Similarly, Nucleotide Excision Repair (NER) focuses on removing bulky DNA adducts that distort the DNA helix, like pyrimidine dimers [13]. NER is divided into global genome repair (GGR), which patrols the entire genome for lesions, and transcription-coupled repair (TCR), targeting lesions in actively transcribed genes. This dual approach ensures comprehensive coverage, safeguarding both coding and non-coding DNA regions from significant damage that could compromise cellular integrity.

1.3.3 Effect of Reactive Oxygen Species in the cell

Reactive oxygen species (ROS) have a complex role in how cells behave. At low levels, ROS help in cell signaling processes, but at high levels, they can damage cells via oxidative stress. In the context of radiotherapy, ROS levels increase to a point where it can cause damage to the cells by shaking the balance of oxidation and reduction (redox balance) and promoting cell death pathways [18, 19]. At the same time, cancer cells enhance their oxidative stress defenses to better manage this oxidative challenge, which could make them more resistant to RT. This defense includes enzymes like glutathione peroxidase (GPX), catalase (CAT), and superoxide dismutase (SOD), and other antioxidants like glutathione (GSH) and thioredoxin (TRX).

The Nuclear erythroid 2-related factor (NRF2) is key in controlling how cells defend themselves against damage from oxidation. When NRF2 is turned on, it boosts the cell's production of important defense genes, including those that lead to the production of antioxidants like glutathione peroxidase, superoxide dismutase, and catalase [20].

The enzyme GPX reduces ROS by converting GSH to its oxidized form, GSSG, through the reaction

$$2\text{GSH} + 2H_2O_2 \rightarrow \text{GSSG} + 2H_2O.$$

Following this, Glutathione Reductase (GR) uses NADPH to convert GSSG back into GSH, as shown by

$$\text{GSSG} + \text{NADPH} + H^+ \rightarrow 2\text{GSH} + \text{NADP}^+.$$

In parallel, Peroxiredoxin (PRDX) acts to remove ROS and is restored to its active state by Thioredoxin (TRX) and Thioredoxin Reductase (TrxR), ensuring a steady defense against ROS. These enzymes play a crucial role in clearing excess ROS from the cell, including H_2O. Moreover, Catalase (CAT) directly converts high concentrations of H_2O into water and oxygen, as indicated by

$$2H_2O_2 \rightarrow O_2 + 2H_2O,$$

1.3.4 Cell Survival and the Linear Quadratic Model

Clonogenic cell survival is a basic tool that was described in the 1950s for the study of radiation effects on mammalian cells [21]. It is still considered the gold standard method for assessing radiosensitivity in vitro [22]. Historic data suggest that the radiosensitivity of cancer cells measured in clonogenic assays is associated with the clinical response of a tumor to radiotherapy [23, 24, 25, 26].

The relationship between the radiation dose and the proportion of surviving cells after irradiation, is described by a cell survival curve [13]. The procedure to obtain the survival curve for a specific cell type after irradiation, consists on seeding a known number of cells in a vessel, exposing them to radiation, and finally counting the number of colonies formed after a certain time (Figure 1.7). This number of colonies that survived, has to be corrected by a factor called platting efficiency (PE). This factor takes into account possible mishandling or errors and uncertainties in counting cells before seeding [13]. The platting efficiency is defined as:

$$PE = \frac{\text{Number of surviving colonies}}{\text{Numbers of cells seeded}}, \tag{1.21}$$

and the survival fraction as:

$$SF[\%] = \frac{\text{Colonies Counted}}{\text{Cells seeded } \times PE} \cdot 100. \tag{1.22}$$

In order to obtain a survival curve as a function of dose, this procedure must be carried out across a variety of dose levels.

Figure 1.7: Colonies obtained with A549 cells culturesd in vitro.

Figure 1.8 illustrates the standard cell survival curve on a log-linear graph. The behavior of the survival curve in response to radiation can be summarized based on the dose level and the type of radiation. For low-linear energy transfer radiations like x-rays, the curve initially appears as a straight line indicating that cell survival decreases exponentially with increasing dose. As the dose increases, the curve begins to bend over a range of a few grays. Then, at extremely high doses, the curve may straighten out again, suggesting that cell survival once more follows an exponential decrease with dose [13].

On the other hand, with high-LET radiations such as alpha particles or low-energy neutrons, the cell survival curve remains a straight line from the start, showing that cell survival decreases exponentially with dose [13].

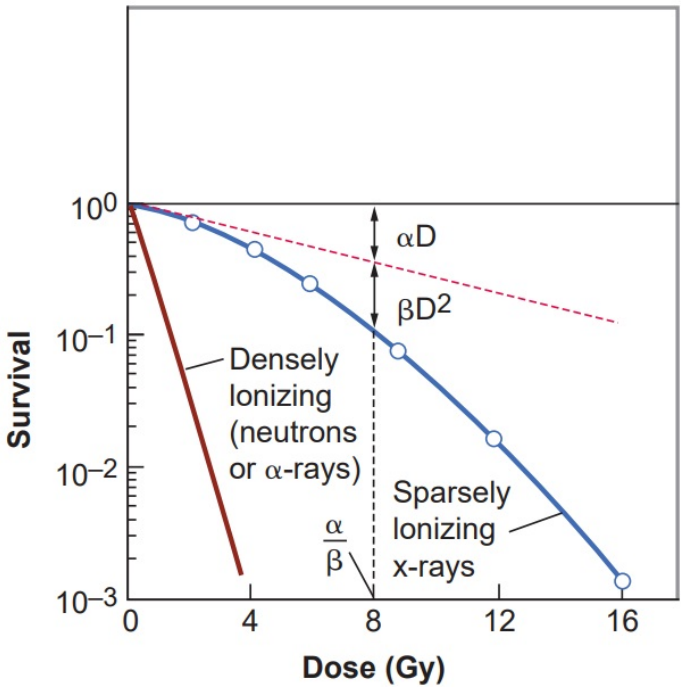

Figure 1.8: Colonies obtained with A549 cells culturesd in vitro. Image taken from [13].

Currently, many biophysical models have been proposed and can explain the shape of the survival curves [27]. However, it's difficult to conclude which model is the best one. This difficulty arises because the biological data available is not precise enough, and the predictions made by the different models do not vary enough from one another to make a clear choice possible [13].

Currently, the model of choice to describe survival curves is the Linear-Quadratic

Model (LQM) [13, 28]. The LQM takes inspiration from the linear-quadratic dependence that the chromosomal aberrations have as a function of dose [29, 30]. In this model, the survival curve is described as:

$$SF = e^{-\left(\alpha D + \beta D^2\right)}, \tag{1.23}$$

where two different types of lethal hits are accounted for. The single-hit kill, represented by the parameter α, refers to cell damage that is permanent and cannot be repaired. On the other hand, the two-hit kill, denoted by β, involves damage that cells have the potential to repair.

A key aspect of this model is that both contributions, linear and quadratic, are equal if the dose is equal to $\frac{\alpha}{\beta}$.

1.3.5 Relative Biological Effectiveness

The Relative Biological Effectiveness (RBE) is defined as a ratio between two absorbed doses delivered with two radiation qualities, one of which is a *reference radiation*, that result in the same effect in a given biological system, under identical conditions [31]:

$$RBE = \frac{D_{ref}}{D} \tag{1.24}$$

Typically, for reference radiation, a low-LET radiations like 250 keV photons or gamma rays emitted by Cobalt-60 are used.

1.4 The FLASH Effect

FLASH radiotherapy, represents one of the most promising approaches involving the reduction of risk of complications that are present in radiation treatments [32, 33]. This technique makes use of ultra-high dose rates of radiation ($\geq$ 40 Gy/s) significantly higher than those used in conventional radiotherapy ($\leq$ 0.03 Gy/s) [34].

The unique aspect of FLASH radiotherapy lies in its ability to minimize damage to healthy tissue while preserving tumor control [34]. This differential effect is what is called *the FLASH Effect*, and it is attributed to the ultra-high dose rates, which are believed to induce distinct biological mechanisms compared to conventional radiation therapy.

The concept of using high dose rates for radiation therapy is not entirely new; initial observations of its potential benefits date back over 50 years, when experiments in bacteria exposed to ultra-high dose rates, ranging from 10 to 20 kilorads [1] within a 2-microsecond span, exhibited a radioprotective effect when compared to those irradiated at standard dose rates [35].

The increase of interest in FLASH radiotherapy over the past decade s driven by a growing amount of experimental evidence suggesting its potential to reduce side effects associated with radiation therapy. In particular, the study reported in 2014 by Favaudon and colleagues [33] showed a significant reduction in normal tissue injury with electron FLASH RT in a mouse model of lung fibrosis.

By now, the FLASH Effect has been reported in a variety of tissues, including brain [36, 37, 38, 39, 40], blood [41, 42] and skin [43, 44, 45]. These findings were observed in experiments using different radiation types, highlighting the broad applicability of FLASH radiotherapy.

Possible Mechanisms

Given the rapid knowledge development of FLASH RT, several hypothesis to explain the FLASH Effect have been explored. In this section we will focus on those proposing a physical-chemical mediated mechanism. Therefore, the oxygen depletion hypothesis, the free radical recombination and the metabolism of peroxidized compounds and Fenton chemistry hypotheses will be discussed. While these represent a subset of the proposed mechanisms, they are of interest within the topic of this thesis. For a comprehensive review, readers are encouraged to consult existing literature on the subject [34, 46, 47, 48].

Oxygen plays a crucial role as a radiation sensitizer [13], making oxygen-rich tissues more susceptible to radiation than hypoxic ones. The Oxygen depletion hypothesis proposes that FLASH RT rapidly consumes oxygen in tissues faster than it can be replenished by blood flow. The large amount of oxygen reduction, compared to the one experienced in conventional radiotherapy, contributes to the spearing of normal tissue [49]. This theory is inspired in the results of early studies on bacteria and mammalian cells, where it was observed that hypoxia increases resistance to ultra-high dose rates

[1] The rad is a unit of absorbed radiation dose defined in 1953 as 1 rad = 0.01 Gy.

[35, 50].

It is now recognized that the oxygen depletion hypothesis does not entirely account for the protective effects on normal tissues by the FLASH effect. Oxygen depletion measurements during irradiation performed by Jansen and colleagues [51], showed that while irradiation at UHDR consumes more oxygen than at conventional dose rates, it does not deplete enough oxygen to induce an hypoxic environment. In addition, *in vitro* studies have found the radioprotective contribution of the FLASH Effect even in normoxic conditions [52], challenging the idea that oxygen depletion alone explains the differential effects on tumor versus normal tissues.

Afterwards, Spitz [53] suggested that the differential metabolism of peroxidized compounds and the different amount of labile iron between normal and tumor tissues could explain the differential ability to reduce damage to normal tissue while maintaining antitumor efficacy. Unlike tumor tissues, normal tissues can metabolize peroxidized compounds more effectively and have lower levels of labile iron, reducing the potential for damage through Fenton chemistry. Although this theory offers a compelling explanation, it remains hypothetical until further validated by experimental studies.

The radical-radical recombination hypothesis suggests an explanation for the different effects observed between FLASH and conventional radiation therapies on tissues. According to this theory, the ultra-high dose rates characteristic of FLASH RT lead to a significant increase in free radical concentrations. Consequently, this rise enhances the probability of radicals combining with each other, thereby decreasing the pool of radicals that could potentially engage in harmful interactions. The involved reactions are:

$$\mathrm{R}\cdot + \mathrm{R}\cdot \longrightarrow \mathrm{R}-\mathrm{R} \tag{1.25}$$

$$\mathrm{R}\cdot + \mathrm{O}_2 \longrightarrow \mathrm{ROO}\cdot \tag{1.26}$$

The first reaction illustrates the addition of two radicals to form a stable molecule, thus diminishing the pool of free radicals. The second reaction, however, outlines how a radical could interact with oxygen to form a peroxyl radical, a known agent of cellular damage.

This hypothesis suggests that the increased rate of radical recombination in FLASH

radiation decreases the probability of harmful radical interactions with oxygen, resulting in reduced oxidative stress and subsequently less damage to healthy tissues. It also considers the role of labile iron and oxygen metabolism. Under high dose rates, the presence of labile metal ions is thought to increase oxygen depletion, impacting tumor cells more due to their higher levels of reactive ROS. This differential impact is believed to be fundamental in the capacity of FLASH RT to protect normal tissues while effectively targeting tumor cells [54].

Recent investigation have raised questions about the comprehensive validity of the radical recombination hypothesis. Studies using Comet assays to measure DNA damage post-FLASH irradiation did not find an expected increase in DNA crosslinking, suggesting that while radical-radical recombination may contribute to FLASH radiation's effects, other factors are likely at play in protecting healthy tissue [55].

Chapter 2

Motivation

Cellular redox state refers to the dynamic equilibrium between oxidants and antioxidants within cells, which plays a fundamental role in maintaining cellular function and response to various stressors, such as ionizing radiation. Numerous biological processes, including metabolism, immunological responses, cell death, differentiation and development and others, are regulated by redox interactions [56]. Therefore, the shift in redox status driven by radiation-induced reactive oxygen species (ROS) generation influences immediate cellular responses and impacts downstream signalling pathways, DNA repair mechanisms, and cellular fate, significantly contributing to the overall cellular response to radiation exposure [57]. The toxic hazard of this phenomenon, known as oxidative stress, depends on the ROS identity, concentration, and subcellular localization [58]. It is very well known that radiation energy deposition, characterized by LET and dose rate, influences ROS production: higher LET results in increased ROS production [36]; meanwhile, higher dose rates decrease ROS production [59]. The main objective of this project is to study the radiobiological response of different cell lines with different inherent redox status to radiation. To this purpose, the hydrogen peroxide production in nuclei in different conditions (using different irradiation particles, increasing the dose rate) was assessed and the cellular redox status was perturbed by using a Superoxide Dismutase (SOD) inhibitor.

Chapter 3

Materials and Methods

In this chapter all protocols used in this project are described. Three main studies were performed as part of this work: *i*) Hydrogen Peroxide production assessment during irradiation, *ii*) Oxidation Reduction Potential measurements of cell cytosolic extract and *iii*) a high dose rate study in the context of FLASH radiotherapy.

3.1 Cell Culture

Human non-small cancer cell lines, H460, A549 and Calu-1 cells were kindly provided by Dr. Ina Kurt at DKFZ. Cells were cultured at 37°C in a humidified atmosphere containing 5% CO_2 and 21% O_2. Passaging of the cells was carried out using phosphate buffer saline solution (PBS)(Sigma Aldrich) for washing, and TrypLE Express (Thermo Fischer Scientific)for detachment of cells, when the cells reached 80% - 90% confluency.

Calu-1 cells were cultured in McCoy's 5A (Modified) Medium, A549 cells in F12K Medium, and H460 cells in Gibco RPMI Medium. All media were purchased from Thermo Fischer Scientific, Germany. All culture media were supplemented with 10% Fetal Bovine Serum (FBS) (Thermo Fisher Scientific) and 1% PenStrep (10,000 U/mL), Thermo Fisher Scientific).

3.2 Hydrogen Peroxide Assessment

Given the relevance of Hydrogen Peroxide in the cell environment, several methods to measure H_2O inside and outside cells have been used. Ranging from traditional tech-

niques like high-performance liquid chromatography to more modern approaches [60]. Among these, small-molecule-based fluorescent sensors offer distinct advantages. They are noninvasive and compatible with live-cell experiments. Additionally, these sensors provide higher sensitivity and precise spatial resolution, enabling real-time observation of cellular processes. Compared to other methods like electron spin resonance, small-molecule fluorescent probes offer flexibility in adjusting properties, robust functionality, and simplified sample preparation [61].

In this work the fluorescent marker called Nuclear Peroxy Emerald 1 (NucPE1) (ENAMINE LTD, Ukraine) was used to score hydrogen peroxide production during irradiation. Given that the dye selectively localizes in the cell nucleus, it is possible to obtain direct measurement of H_2O levels within the cell nucleus. NucPE1 was serendipitously discovered by Chang's group [58]. It exhibits specific absorption peaks at $\lambda_{abs} = 468$ nm and 490 nm, alongside a weak emission at $\lambda_{em} = 530$ nm. When interacting with H_2O, its fluorescence increases, and the absorption band shifts to $\lambda_{abs} = 505$ nm, coinciding with an enhancement in the emission band ($\lambda_{em} = 530$ nm) [58].

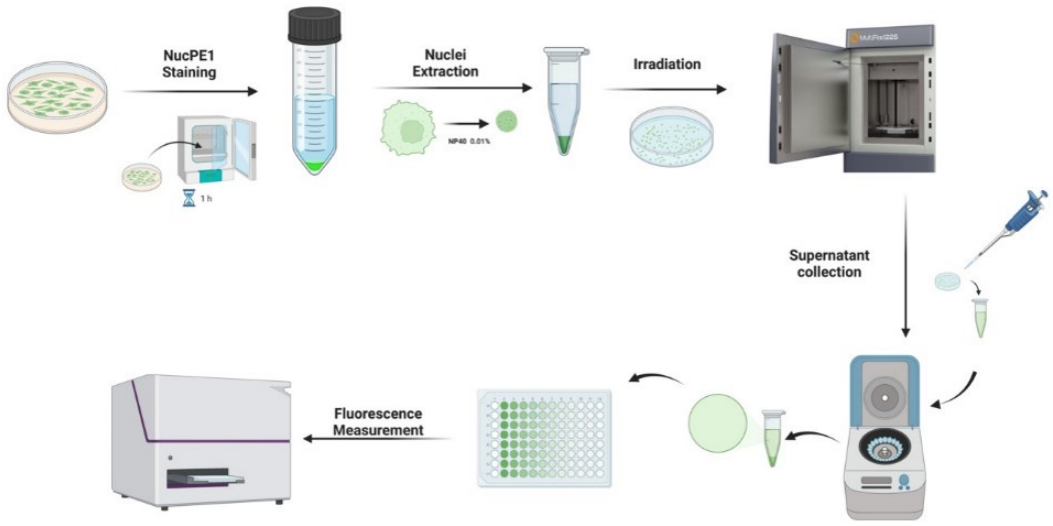

Figure 3.1: Schematic layout of the hydrogen peroxide assessment protocol. See text for detailed explanation. Image created with BioRender.com .

Figure 3.1 illustrates the protocol used to measure H_2O production during irradiation. The experiment began by seeding 1.6 million cells into six 100 mm Petri dishes (Greier Bio-One, Germany) a day before irradiation.

NucPE1 staining

The following day, cells were stained while attached using a 10 μM NucPE1 solution in Hanks' balanced salt solution (HBSS) (Thermo Fisher) and incubated for 1 hour (hr) in a dark environment at 37°C. Subsequently, cells were washed twice with PBS and detached using TryPLE Express. After detachment, cells were collected into a 50 mL tube (Greiner bio-One), and centrifuged (1200 rpm for 5 min).

Nuclei extraction

The subsequent step involved nuclei extraction: the cells were transferred to a pre-chilled 1.5 mL tube and centrifuged again (1200 rpm for 5 min). The supernatant was carefully removed, leaving the cell pellet behind. The pellet was then resuspended in 1 mL of cold-ice PBS containing 0.1% Nonidet P40 and triturated by pipetting up and down 5 times [62]. The sample was centrifuged for 10 seconds at 10,000 rpm. This process was repeated twice. Following the third centrifugation, the supernatant was discarded, and a final wash with 1 mL of PBS was performed, followed by another centrifugation. The supernatant was discarded, and the pellet was resuspended in 1.4 mL of PBS to obtain the final solution containing all the nuclei. After resuspension, the solution was divided into six different 1.5 mL tubes (Eppendorf) and transferred to a suited container for irradiation. One part of this solution was used to obtain the nuclei density employed in each experiment repetition.

Irradiation

After transferring the nuclei solution into the appropriate container, samples were irradiated with doses ranging from 0 to 35 Gy, depending on the specific experiment. This thesis employed at least three types of radiation. Detailed information regarding the exact dose and radiation type will be provided in the relevant sections.

Fluorescence measurement

After all samples were irradiated, the solution from each dose was transferred to a 1.5 mL tube and centrifuged at 10,000 rpm for 5 min. Subsequently, 100 μL of the supernatant was transferred to a well in a black 96-well plate (Greiner Bio-One). Each sample

was measured in sextuplet using a ClarioStar plate reader (BMG LABTECH) with an excitation wavelength of 497 ± 15 nm and a emission wavelength of 540 ± 20 nm .

The raw fluorescent signal was then normalized by the number of nuclei used in the irradiation step, to obtain the quantity referred from now on as *Fluorescence Intensity per nucleus*.

To further investigate the protocol, an additional study was conducted to compare three different approaches: (i)irradiating nuclei after extraction and subsequently measuring the supeirradiating both nuclei and supernatant together and then measuring the nuclei and supernatant together, and (iii)irradiating supernatant alone followed by its measurement. A detailed description of these comparison is described in Appendix B. It was concluded that methods (i) and (ii) provide similar information, however method (i) has allowed us to compare different cell lines without correcting by nucleus size differences.

3.2.1 Cell line dependence on H_2O production

In order to compare the production of H_2O in nuclei during irradiation, and obtain insights into potential differential responses to radiation, the cell lines H460, A549 and Calu-1 were used.

In this experiment the radiation source used was an x-ray tube (220 kV, 5 mm Cu filter) contained in a MultiRad225 irradiator (Faxitron Biotics, USA) . Doses of 1, 2, 4, 8 and 16 Gy were applied in each experiment.

Table 3.1: Non-small lung carcinoma cells used in this work. Alpha and beta values according to the LQM obtained in a previous work [63].

Cell line	Description	α	β
H460	Pleural Carcinoma	0.156 ± 0.047	0.0606 ± 0.0069
A549	Epithelial Carcinoma	0.234 ± 0.006	0.0364 ± 0.0009
Calu-1	Epidermoid Carcinoma	0.202 ± 0.013	0.0463 ± 0.0019

The Fluorescence intensity per nucleus was then compared with the results of the damage marker γH2AX obtained in [63], where the radioresistance of hypoxic tumors was studied for same cell lines that were used in the current work (Table 3.1). From [63], the α and β parameters from the LQM (shown in table 3.1) were also extracted. Clonogenic assays and γH2AX experiments were performed under the same irradiation

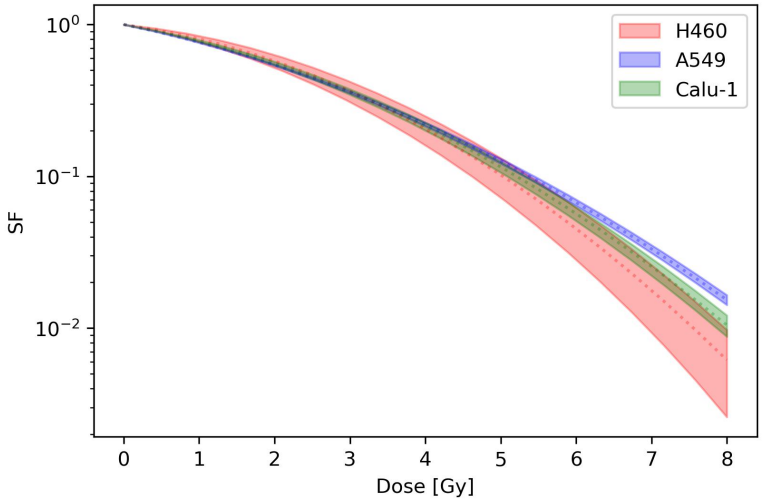

Figure 3.2: Survival curves obtained by plotting the LQM using alpha and beta parameters showed in table 3.1. The errorband was calculated using error propagation for the LQM (k = 1).

conditions as in the described in this thesis. The overall radioresistance of these cell lines is shown in Figure 3.2.

3.2.2 LET dependence on H_2O production

The generation of hydrogen peroxide through radiation-induced water radiolysis is acknowledged to rely on the Linear Energy Transfer of the particles [64, 65]. Therefore, it was natural to validate the method proposed in this work and reproduce the expected phenomena. For this purpose, samples were prepared as described in section 3.2 and irradiated using protons and helium ions.

Irradiations were carried out at Heidelberg Ion-Beam Therapy Center (HIT) utilizing raster scanning beams. Samples were irradiated using 1, 2, 4, and 8 Gy in a 9.0 cm × 9.0 cm field. Treatment plans were created for protons and helium ions (^{4}He) using TRiP version 1310. These plans underwent optimization in terms of physical dose to deliver 1.0 Gy on a 5.0 cm spread-out Bragg peak (SOBP) within the range of 10 to 15 cm in water. As a result, 18 energies for protons and 17 for helium-ions, ranging from 117.50 to 146.56 MeV/u and 119.78 to 147.93 MeV/u, were used, respectively.

In addition to the described experiment, an independent study was conducted involving protons and ^{4}He. This study included LET measurements using fluorescent nuclear track detectors (FNTDs) and clonogenic survival data for different LET spectra using

A549 cells.

For this purpose, cells were seeded in 25 cm^2 flasks (Greier Bio-One) 12 hrs before irradiation. For the irradiation, cells were placed with the bottom of the flask perpendicular to the beam, behind RW3 slabs, in the same positions as the FNTDs for the LET measurements. However, corrections were applied to account for the flask's bottom thickness. After irradiation, cells were kept at 37°C and 5% CO_2 for 11 days, followed by fixation with 100% ethanol and staining using crystal violet. Surviving colonies were manually counted under a microscope, taking 50 cells as the minimum to be considered a colony.

Detailed information about FNTDs handling can be found in the work of Muñoz et al. [66, 67] This study contributed complementary results into radiation effects in the same configuration as the nuclei were irradiated.

3.2.3 Dose rate dependence

To investigate the H_2O production during irradiation in nuclei with varying dose rates using the MultiRad225, the irradiation protocol was adapted from [51]. To increase the dose rate, the Cu filter has to be removed and the target positioned closer to the beam exit (Figure 4.7). Given the change in irradiation setup, new dosimetry had to be implemented by using EBT XD radiochromic films. Detailed information about radiochromic film handling and usage can be found in Appendix A.1.

3.3 Oxidation Reduction Potential

The ORP measurements were performed in cell cytosolic lysates. At least two day before the experiment cells were seeded in T175 flasks. When cells reached 80-90% confluency, cells were detached using TrypLE Express and collected in 50 mL tubes, followed by a centrifugation (1200 rpm for 5 minutes). Once the cell pellet was obtained, the supernatant was carefully removed and 500 μL of the lysis buffer (0.1% Nonidet P40 solution in PBS) was added, and followed by a trituration step (pipetting up and down 5 times). After trituration, the resultant solution was centrifuged for 5 minutes at 10,000 rpm. After centrifugation, the supernatant, at this point cytosolic extract, was carefully placed on another tube. From the 500 μL sample, at least 5 dilutions by adding PBS

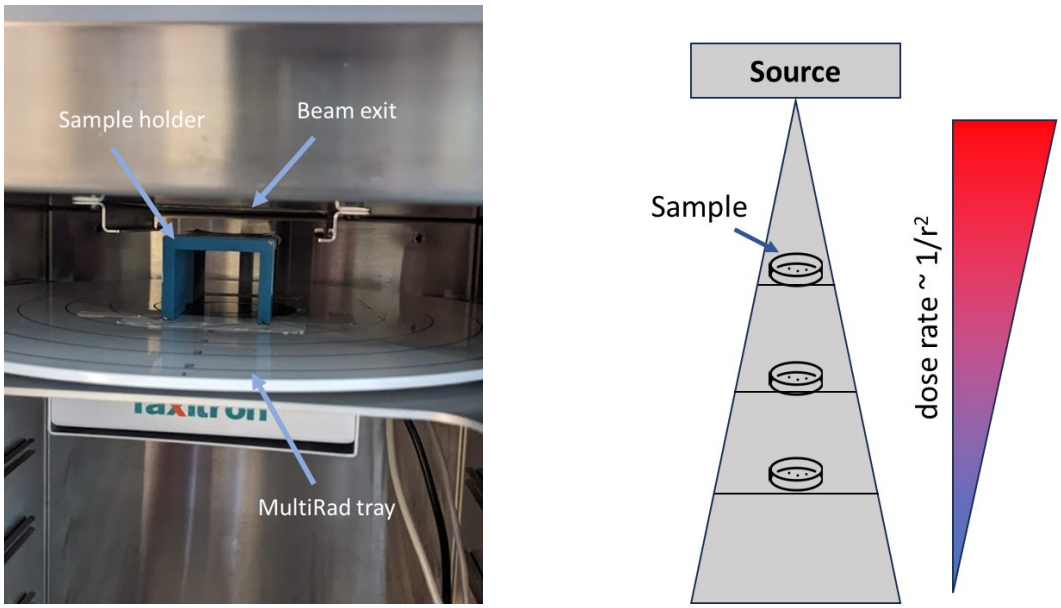

Figure 3.3: Irradiation setup for H_2O measurement using HDR in the MultiRad225. Left: Photograph of the experimental setup showing use of a holder to rise the sample closer to the x-ray tube exit. Right: Scheme showing the inverse square-law effect. Scheme modified from [51]

were prepared. The ORP was measured using the pH meter SevenDirect SD20 (Mettler Toledo) together with the ORP electrode InLab Redox Micro (Mettler Toledo) for all the dilutions. Each sample was measured at least 5 times to calculate an average value and the standard deviation. The cytosolic lysate was stirred in between measurements.

In parallel to the ORP measurements, the cell volumes where measured using microscope images. For this purpose, cells were placed in a glass slide and imaged using a Ti2 E microscope (Nikon), afterwards the cell diameter was obtained using the software NIS Elements (Nikon) for at least 50 cells.

Once all the measurements were performed, the ORP value was plotted as a function of the total cell volume fraction, and a logarithmic fit was performed (section 4.2). This fit let us extrapolate the ORP value of a unit of volume.

The ORP value obtained after the extrapolation was compared with the cells radiosensitivity. For this purpose the dose at 10% survival (D10) was calculated as:

$$D_{10} = \frac{-\alpha + \sqrt{\alpha^2 - 4 \cdot \beta \cdot ln(0.1)}}{2 \cdot \beta} \tag{3.1}$$

where the values for α and β are shown in Table 3.1.

3.4 *In vitro* Studies at High Dose Rate

The use of in vitro clonogenic assays provides an accessible framework for researching the FLASH effect, offering insights into optimal specific beam parameters and the conditions to investigate its underlying radiobiological mechanisms. In this study, an irradiation setup for photon delivery at the highest possible dose rate was optimized, with the goal of conducting clonogenic assays. Additionally, a commercially optimized electron beam irradiation setup for ultra-high dose rate (UHDR) irradiation was employed to conduct clonogenic assays in conjunction with a SOD inhibitor. This approach aims to gain a deeper understanding of the role of H_2O under these irradiation conditions.

3.4.1 Photons

During the course of the HDR experiments described in Section 3.2.3 several experimental challenges were identified, such as time limitations in irradiation that coincided with the inherent ramp-up time of the x-ray tube. Additionally, complications arose from field inhomogeneity due to the heel effect and the utilization of an extremely soft x-ray spectrum. This lead to the design and use of a new irradiation platform, from now referred to as shutter. The shutter (Figure 3.4) was designed to solve drawbacks encountered in the H_2O measurements described before.

The shutter allows to irradiate for times shorter than 1 second. The latter required the MultiRad225 irradiation timer to be set at 4 seconds. Two seconds into the irradiation period, the rotating mechanism was turned on, allowing to get rid of the ramp up influence and making every irradiation output consistent. The target consisted on a in-house modified 15.5 mm well placed on top of 3 brass plates. The brass plates increased the dose rate at the closest position by a factor of 1.5 times compared with air [68]. The positioning of the target was optimized using radiochromic films (RF), in this way the field inhomogeneity due to the heel effect was reduced.

Given that the rotating mechanism allowed for irradiation of fractions of seconds (0.1, 0.2 , 0.4 , 0.6 and 0.8 s), new dosimetric measurements were performed to evaluate the dose rate at the determined position. Additionally, since the irradiations were performed without Cu filter, the RF response to the change in photon spectrum had to be studied. To achieve this, RF measurements were compared with measurements performed using an

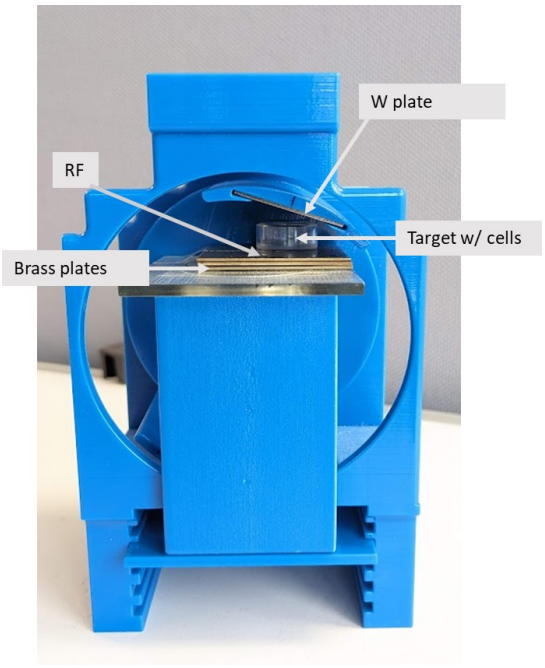

Figure 3.4: Shutter picture. Tungsten (W) plates were used to block the x-ray beam, the target consisted in a modified well on top of 3 brass plates. The shutter was fixed to the x-ray tube exit of the MultiRad225.

Advance Markus chamber 3118 at various depths under RW3 slabs, thereby identifying the change in RF response and its optimal usage, assuming minimal dependence of the IC to low energy spectrum. The cross-calibration of the Markus chamber with the reference chamber used by the DKFZ dosimetry department, and the RF response study to the unfiltered x-ray beam can be found in Appendix A.2.

To be able to quantify the dose that the cells received, the ratio between the dose measured under the bottom of the well and the one on top of it was calculated. This factor is referred to as in/out factor, full details on the measurement are available in Appendix A.3.

Clonogenic Assays

The clonogenic assays were conducted following a similar procedure as described in [63] using H460 and A549 cells. A day before the experiment 120,000 H460 cells or 100,000 A549 cells were seeded in a 15.5 mm diameter well. On the day of the experiment, cells were washed once using HBSS once and then 260 μL of HBSS were added to the well. Next, the well was covered with Parafilm previously sterilized by using ethanol and UV light. Immediately after, the well was positioned in the shutter and irradiated. The high

dose rate (HDR) irradiation was performed as mentioned above, and the conventional dose rate (CONV) was performed by setting the shutter to an open position and lowering the x-ray tube's current from 17.8 mA to 0.5 mA. Both irradiation configurations were performed with 225 kV as x-ray potential.

After irradiation, the HBSS was removed and the cells were washed with 200 μl of PBS and detached with 200 μl of TrypLE Express and a 9 minute incubation. Next, the TrypLE Express is diluted with 400 μl of complete medium. Then, the cells are collected and centrifuged at 1,200 rpm for 5 min. After centrifugation, cells were resuspended in complete medium per sample and the cells were counted. Depending on the irradiation condition, an appropriate number of cells was seeded in T25 flasks using 5 mL of complete medium, in triplicate.

After seeding, the flasks were incubated for 10 (H460) or 11 (A549) days. Subsequently, the colonies were fixed using 100% ethanol and stained using crystal violet. Surviving colonies were manually counted under a microscope, taking 50 cells as the minimum to be considered a colony.

3.4.2 Electrons

Due to the setbacks encountered in the optimization process of the x-ray beam for high dose rates, a new set of experiments was conducted using a FLASH-dedicated system called ElectronFlash (S.I.T. Sordina IORT Technologies). In addition to studying the cell survival dependence on dose rate, these experiments investigated the effect of a SOD1 inhibitor when combined with the change in dose rate.

The ElectronFlash linac addresses challenges faced by medical linacs adapted for ultra-high dose rates in FLASH radiation therapy research. It offers optimized fluence transmission and minimized leakage, achieved through radial focusing and defocusing quadrupoles[69]. It operates at 7 and 9 MeV, with adjustable pulse repetition frequencies and lengths, providing dose rates ranging from 0.0005 to 1500 Gy/s. Its rotating gantry allows vertical and horizontal positioning, with collimation using PMMA applicators and a dual dose monitoring system for FLASH and conventional modalities [69].

SOD1 activity reduction was achieved by using the compound known as ATN-224 (Figure 3.5, a choline salt of tetrathiomolybdate and a copper chelator [70].

The ElectronFlash (Figure 3.6), located at Antwerp University Hospital, Belgium,

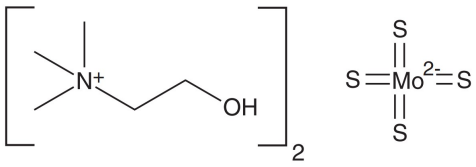

Figure 3.5: ATN molecular structure. Image taken from [70]

.

was used for both conventional (CONV) and FLASH modalities during the conducted in vitro experiments. 9 MeV electrons were employed, with the FLASH modality using a pulse repetition frequency of 200 Hz compared to 1 Hz for CONV, and pulse lengths of 1.4 μs for FLASH and 1 μs for CONV. These configurations resulted in dose rates ranging from 220 to 280 Gy/s for FLASH and 3.9 to 4.2 Gy/min for CONV, with doses per pulse varying from 1.1 to 1.4 Gy for FLASH and from 0.065 to 0.070 Gy for CONV. To ensure optimal field size and uniformity, a 120 cm PMMA collimator was fixed at the entrance of the beam. The beam was vertically oriented to accommodate cell flasks positioned on top of the collimator. Additionally, a modified 1 cm RW3 slab, attached to a 3D printed support, was placed to achieve a water equivalent thickness of 1.3 cm. This setup allowed for the placement of two T25 cell culture flasks side by side (Figure 3.6.

Figure 3.6: Photos of the experimental setup used in the ElectronFlash facility. Left: ElectronFlash linac. Right: T25 placement as irradiation, showing the use of EBT XD radiochromic films for dose measurements.

The experiment consisted in two parts: clonogenic assay for both irradiation modali-

ties (CONV and FLASH) using H460 and A549 cells, with and without ATN treatment, and SOD Activity measurements.

Clonogenic Assays

The cells were seeded one day before the experiment, with one T25 flask prepared for irradiation and treatment condition. Equal numbers of cells were seeded for each condition, maintaining similar confluency between cell lines and conditions on the day of the experiment.

On the experiment day, cells were washed with HBSS before treatment. ATN-224, at a concentration of 60 µM in complete medium, was chosen based on viability studies and SOD activity measurements previously performed [71]. Alternatively, cells were treated with complete medium alone for 1 hour.

After the treatment time was finished, cells were irradiated using 0, 2, 4, 10 and 14 Gy. Afterwards, cells from each sample were washed, detached, and counted. Seeding densities varied based on the expected survival fraction and plating efficiency, ensuring a comparable number of surviving colonies for each condition. Cells were seeded in 6-well plates, therefore ensuring six replicates per condition.

Cells were maintained in the incubator for 10-11 days, depending on the cell line (H460: 10 days, A549: 11 days), allowing colony formation. As before, after the incubation time cells were fixed using 100% ethanol and stained with crystal violet. Finally, the colonies, defined as containing more than 50 cells, were manually counted using a microscope.

SOD Activity

The SOD activity measurements were performed using the SOD Determination Kit (Sigma Aldrich) following the manufacturer's instructions [72]. Details on the use of the SOD activity kit can be found on the Appendix C.

3.5 Statistical Analysis

Statistical analyses were performed using the software Sigmaplot (Version 14.5).

The normality of groups was assessed using the Shapiro-Wilk test, and the Brown-Forsythe test was used to asses the equal variance between compared groups. A one-way ANOVA was used to determine the significance between all groups using the Holm-Sidak method multiple comparison test whenever indicated. Results were expressed as mean $\pm$ standard deviation. All analyses considered a value of $P \leq 0.05$ to be statistically significant.

Chapter 4

Results

4.1 Hydrogen Peroxide Assessment

The aim of this study was to quantify hydrogen peroxide (H_2O) production within the cell nucleus across various cell lines, radiation types, and dose rates. Understanding this phenomenon provides valuable insights into the role of H_2O in inducing cellular damage after radiation exposure, advancing our existing knowledge. To achieve this, the fluorescent H_2O marker known as Nuclear Peroxy Emerald 1 (NucPE1) was used. The key advantage of NucPE1 is its specific localization within the cell nucleus, enabling precise assessment of H_2O production within this organelle.

Several methodologies, including flow cytometry and microscopy, were explored to measure H_2O production during irradiation within the cell nucleus. However, due to the inherent instability of the fluorescent signal, our initial attempts yielded inconsistent results. To address this challenge, a new protocol was developed (described in section 3.2).

Given the reactive nature of H_2O, stability tests on the fluorescent signal obtained post-irradiation were performed, as detailed in [73]. Additionally, to account for variations in sample composition, a comparative study evaluating the fluorescent signal from three different regions of the nuclei solution samples was conducted. The results and discussion of these experiments are provided in Appendix B.

In this section the most relevant results from assessing H_2O production in cell nuclei following irradiation, considering various cellular environments, radiation types, and dose rates, are described.

4.1.1 H_2O production after x-ray irradiation in lung cancer cells

The response of H_2O production during x-ray irradiation, measured in nuclei, was examined in three lung cancer cell lines: H460, A549, and Calu-1 (Figure 4.1). This three cell lines are Non-Small Cell Lung Cancer, which accounts for approximately 85% of all lung cancers [74].

The fluorescence intensity (FI) per nucleus exhibited a dose-dependent increase across all cell lines. Interestingly, we observed cell line-specific behavior: for doses below 2 Gy, H460 displayed the highest signal, indicating greater susceptibility to H_2O, consistent with previous findings [63]. However, no significant difference was noted between Calu-1 and A549 within this dose range. Following a 2 Gy radiation dose, Calu-1 exhibited a larger increase in signal compared to A549, resulting in a significant difference between these cell lines. Notably, H460 maintained the highest H_2O production, suggesting a possible reduced capacity in counteracting H_2O production. For doses exceeding 2 Gy, Calu-1 exhibited the highest fluorescent signal, followed by H460 and A549 with the lowest signal. At the maximum dose of 16 Gy, all cell lines exhibited similar values, with no significant difference observed according to ANOVA testing, suggesting that under extreme radiation exposure cells may not be able to deal with the elevated H_2O levels leading to similar outcomes regardless of the cell type.

To further analyze the relationship between H_2O production and DNA damage, the formation of γH2AX foci, a marker of double-strand breaks (DSBs), 30 minutes post-irradiation (Figure 4.2) was plotted against the corresponding change in FI per nucleus (Figure 4.2). At 0 Gy, Calu-1 exhibited a higher baseline level of γH2AX foci compared to the other cell lines. Subsequent changes induced by H_2O were more pronounced in H460, as evidenced by the higher FI change. It was only after this point that Calu-1 exhibited radiation-induced damage. This suggests that for Calu-1, H_2O production may not be the primary cause of DSBs. Notably, all cell lines reached saturation levels of DSB markers at 8 Gy, with H460 and Calu-1 demonstrating similar values and A549 displaying lower levels. This may indicate the utility of NucPE1 as a damage marker, although individual differences in DNA damage repair mechanisms should be considered.

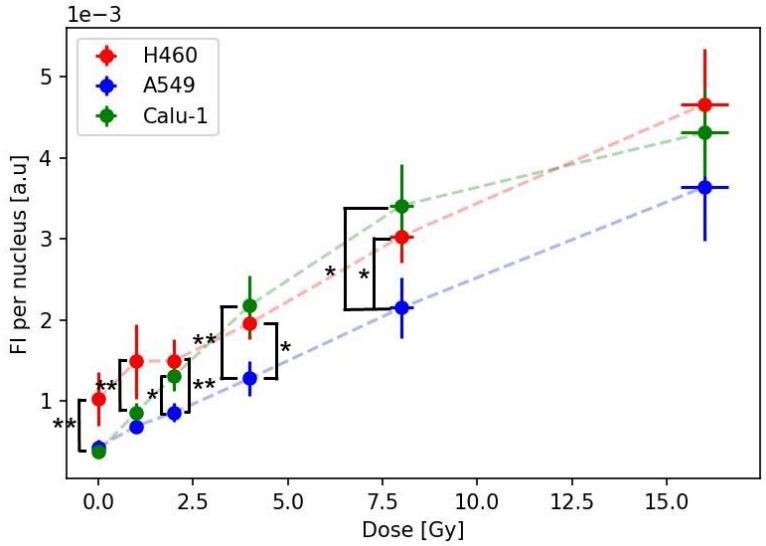

Figure 4.1: Fluorescence intensity (FI) measured normalized by the nuclei used per well as a function of dose for H460, A549 and Calu-1 cells. The data points represent average (n=3) and the error bar the standard deviation. The straight dashed line connecting points for visual guidance purposes. $\star p < 0.05$, $\star\star p < 0.01$

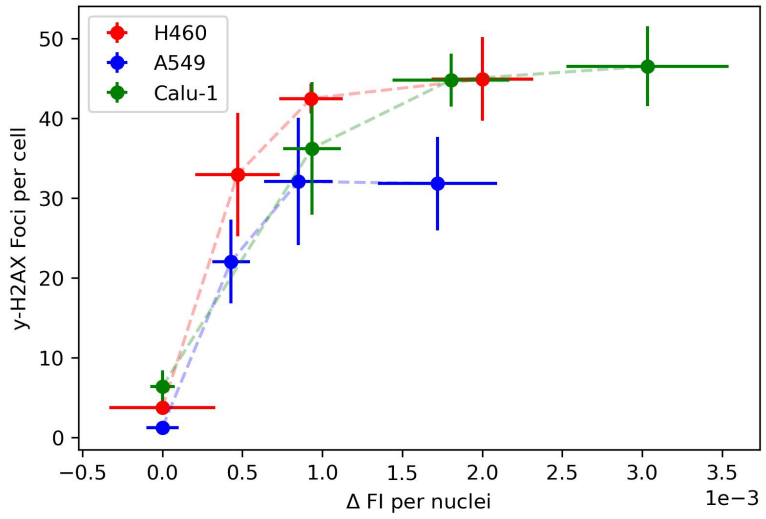

Figure 4.2: DSB damage marker γ-H2AX Foci per cell as a function of the change (Δ) of FI per nucleus for the 3 lung cell lines. Each data point correlated each of the magnitudes measured for the same dose after x-ray irradiation.

4.1.2 LET dependence

An identical approach to quantify H_2O production was employed to copmare differences observed when irradiating A549 cells with protons and helium ions, with the results obtained from x-ray irradiation. The outcomes of this investigation are shown in Figure 4.3.

An increase in H_2O production across all three types of radiation, though the extent

of the increase varied for each radiation type used. Interestingly, the baseline fluorescence intensity per nucleus remained consistent across the different irradiation setups. Notably, significant differences were observed in H_2O production between helium and x-ray irradiation for doses of 2 and 8 Gy. Conversely, no significant differences were found in the values obtained with protons compared to the other two irradiation setups. However, there appeared to be a trend towards an intermediate value, which was quantified using a linear fit to the data.

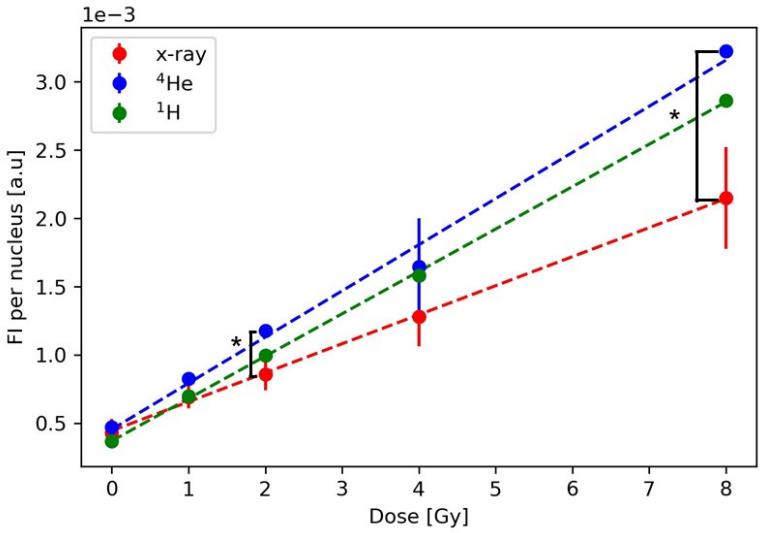

Figure 4.3: Fluorescence Intensity (FI) per nucleus obtained after irradiation using x-ray, Helium ions (^{4}He) and protons (^{1}H) using A549 cells. Each data point represent the average (n=2) and the error bar the standard deviation. The dashed lines represent a linear fit for each data set. $^\star p < 0.05$, $^{\star\star}p < 0.01$

In Figure 4.4, the slope of a linear fit to the data obtained in Figure 4.3 is plotted as a function of the Linear Energy Transfer (LET) measured with Fluorescent Nuclear Track Detectors (FNTDs). Here, it is demonstrated that the increase in H_2O production within the nuclei solution is 1.46 ± 0.03 and 1.59 ± 0.08 times higher for helium and protons irradiation, respectively, compared to the increase per Gy when using x-rays.

The results from the clonogenic assays performed under the same configuration as the 'H_2O measurements are shown in Figure 4.5. As expected, The findings indicated heightened sensitivity to helium ions and protons compared to x-ray irradiation. The latter is confirmed when calculating the dose value at 10% survival (Table 4.1). Using these measurements, the RBE values of 1.1 ± 0.1 and 1.3 ± 0.1 can be derived, taking the 200 kv x-ray as reference, for protons and helium ions, respectively.

For comparison with reported data in the literature [76], Figure 4.6 shows the Rel-

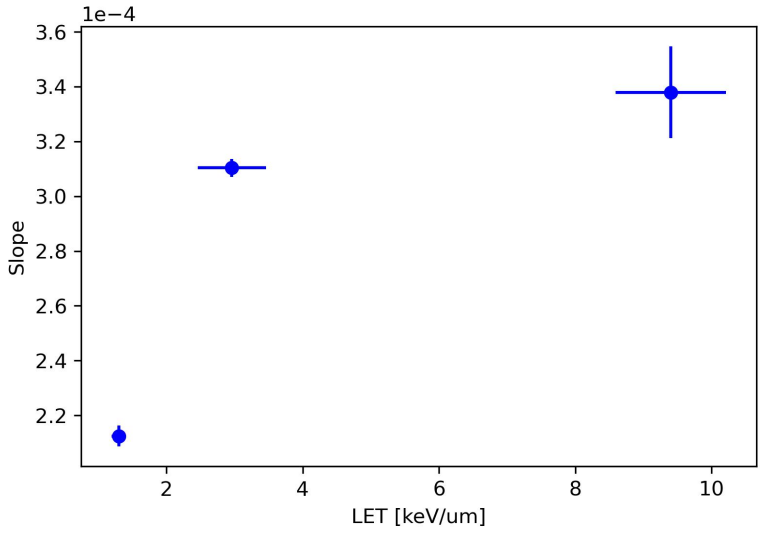

Figure 4.4: Slope from the linear fit to the curve showed in Figure 4.3 as a function of LET. LET values correspond to dose-average linear energy transfer measured for ^{4}He and ^{1}H. The x-ray LET was obtained from [75].

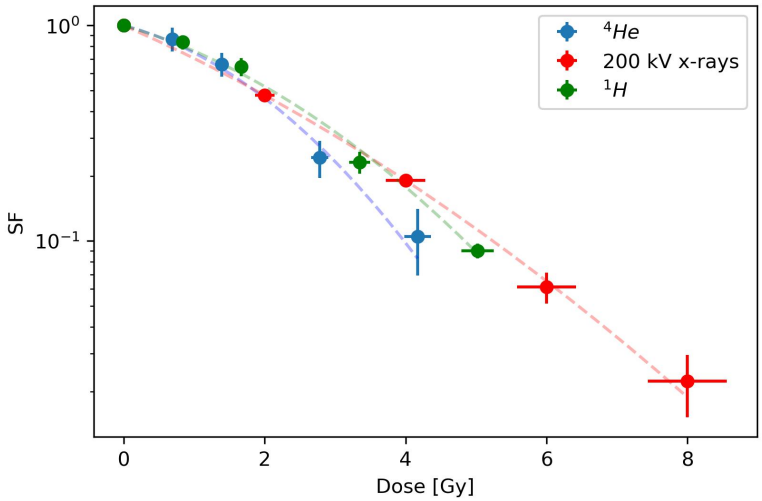

Figure 4.5: Clonogenic assays performed using different radiation sources: x-ray (red), helium ions (blue) and protons(green). Dashed line represents the fit of the LQM, the parameters alpha and beta are reported in table 4.1

ative Biological Effectiveness (RBE) calculated at 10% cell survival, with 6 MV x-rays serving as the reference radiation quality (data not shown), plotted alongside RBE values calcluated in the same manner for 71 MeV protons and 160 MeV protons, for A549 cells. The results obtained in this study align with the reported data.

Table 4.1: Alpha and beta parameters obtained after applying the LQM fit to the clonogenic data and dose at 10% survival for A549 cells.

	alpha [Gy^{-1}]	beta [Gy^{-2}]	d10 [Gy]
x-ray	0.331 ± 0.008	0.021 ± 0.002	5.2 ± 0.1
^{4}He	0.20 ± 0.07	0.10 ± 0.03	4.0 ± 0.5
^{1}H	0.22 ± 0.05	0.05 ± 0.01	4.8 ± 0.5

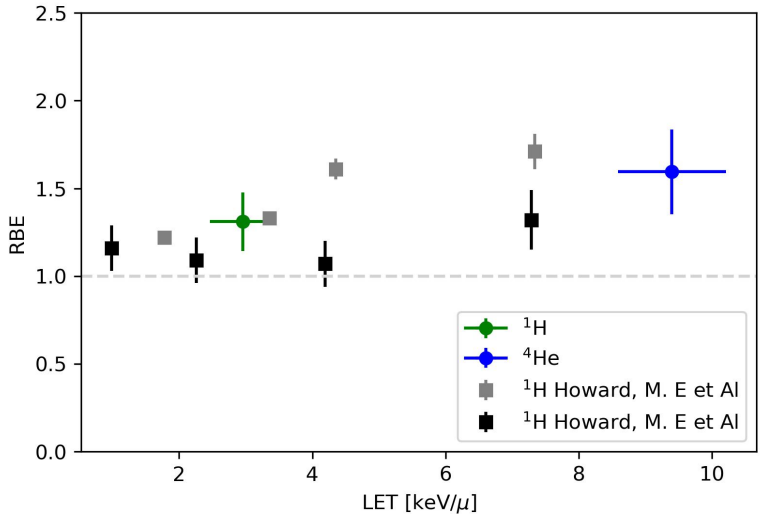

Figure 4.6: Plot of the RBE for helium (blue) and protons (green) calculated at the 10% cell survivals using A549 cells in this work, and RBE calculated at the same survival fraction, in gray (71 MeV) and blue (160 MeV) as a function of dose averaged LET. Additional data from [76].

4.1.3 H_2O dose rate dependence

FLASH radiotherapy (RT) is an emerging RT modality that makes use of ultra high dose rates, it has gain large interest in radiation oncology due to its potential to enhance in cancer treatment by preserving healthy tissue while maintaining comparable tumor control, also known as the FLASH effect. Understanding the mechanism (or mechanisms) behind the FLASH effect would allow to optimize potential patient treatments. Several mechanisms have been proposed, including the differential production of reactive oxygen species (ROS) at varying dose rates, referred as radical recombination [34, 46]. Recent measurements of H_2O production at different dose rates in water have shown a notable decrease with increasing dose rate, hinting at a potentially inverse relationship between dose rate and ROS production [36, 77]. To explore this hypothesis, experiments aimed to increase the dose rate available using a MultiRad225 were conducted. This was achieved by reducing the distance from the target to the exit of the x-ray tube and removing the

0.5 mm Cu filter that is routinely used. However, there was a time constraint of 1 second for irradiation in the setup designated as high dose rate (HDR).

Figure 4.7 illustrates the measured H_2O levels for high dose rate (>3 Gy/s) and conventional (CONV: 9 Gy/min) configurations. A linear fit was applied to all data points (dashed lines), revealing a potential decline in H_2O production at higher doses and dose rates, although with no statistical significance between the two configurations.

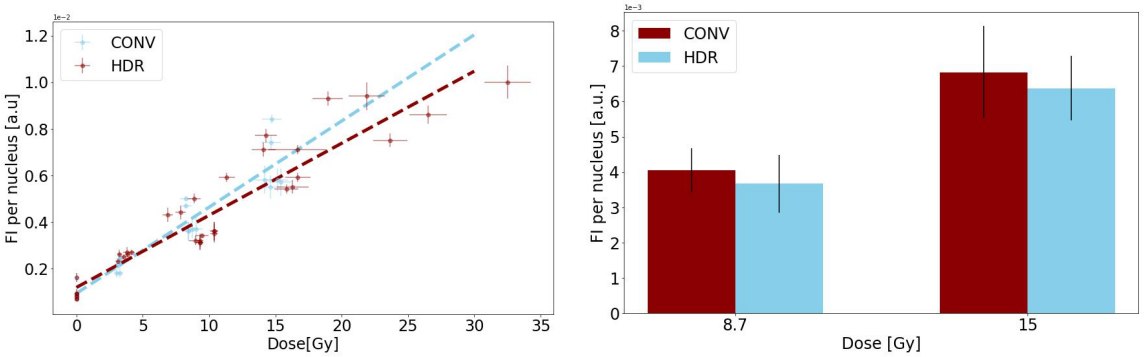

Figure 4.7: H_2O production in nuclei after x-ray irradiation using HDR and H460 cells. Left: data points obtained for both configurations at different dose values. For CONV, the dose rate used was 9 Gy/min, while for HDR, the dose rate was calculated as the dose per second due to the 1-second irradiation restriction. The dashed line represents a linear fit. Right: Comparison of average fluorescence intensity (FI) per nucleus values for doses of 8.7 Gy and 15 Gy.

4.2 Oxidation Reduction Potential

The oxidation-reduction potential (ORP) serves as an important parameter in numerous scientific and industrial applications [78, 79], providing insights into the redox state of a system.

ORP measures the balance between oxidizable and reducible compounds in a specific system [80]. Similar to how pH measures the activity of hydrogen ions, ORP indicates the activity of electrons within the medium [81]. This potential, expressed in millivolts (mV), results from the equilibrium between the electron activity in the sample and the adsorption/desorption processes at the surface of a metal electrode [80]. For a system at equilibrium, the ORP is determined by the Nernst equation:

$$E_h = E^0 + \frac{RT}{nF} \cdot \ln\left(\frac{[OX]}{[RED]}\right) \tag{4.1}$$

where E_h is the redox potential relative to the standard hydrogen electrode, E^0 is the

standard potential of the system at 25°C when the activities of all reactants are unity, R is the gas constant, T is the absolute temperature in Kelvin, and F is the Faraday constant.

In a cellular context, the cellular redox state is believed to play a crucial role in the effects of ionizing radiation, having an impact in ROS production during irradiation and potential oxidative stress. This effect was quantified in this work by measuring the ORP of cytosolic lysate and compared with the cell's radiosensitivity.

To this purpose, ORP measurements were conducted on various fractions of volume of cell cytosolic lysate, followed by extrapolation to estimate the ORP at a unit of cellular volume.

This process is shown in Figure 4.8, where the results of a single experiment for each cell line are shown, together with a logarithmic fit used to perform the extrapolation. Notably, the logarithmic fit reveals distinct behaviors per cell line, suggesting variations in the relationship between ORP values and total cell lysate volume fractions among different cell lines. Such differences may reflect differences in cellular metabolism, antioxidant capacity, or other factors influencing the redox state of the cells.

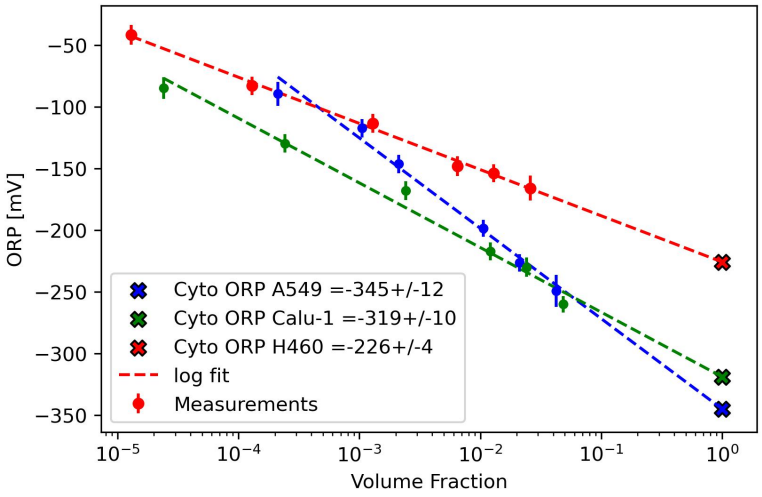

Figure 4.8: Example of the curves to calculate the ORP for the 3 lung cell lines.

The average results of the ORP measurement experiments are presented in Figure 4.9. The ORP values were -232 ± 18 mV for H460, -363 ± 28 mV for A549, and -319 ± 36 mV for Calu-1. Significant differences were observed when comparing H460 with the other two cell lines, whereas no significant difference was found between A549 and Calu-1.

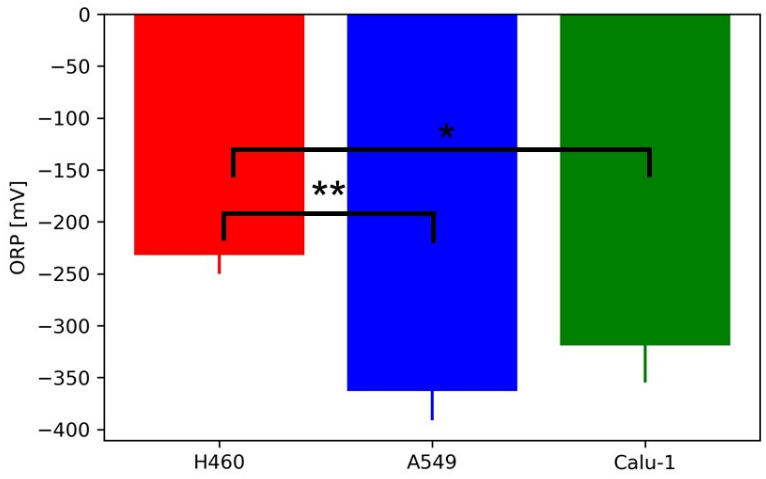

Figure 4.9: ORP values for the 3 lung cancer cell lines. Average of at least 3 different experiments. $^{\star}p < 0.05$, $^{\star\star}p < 0.01$

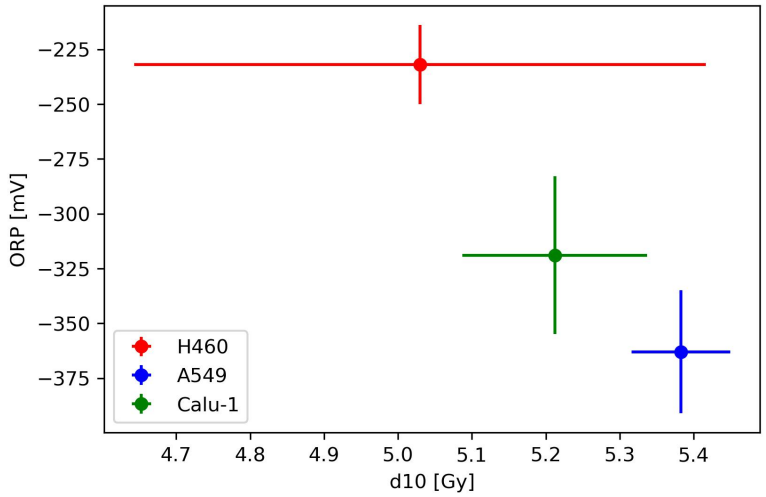

Figure 4.10: ORP measurements for the 3 lung cancer cell lines as a function as the dose at 10% survival (d10). Data points are average between experiments (n> 3) and error bar the standard deviation calculated by Gaussian propagation

Furthermore, the relationship with radiosensitivity by comparing it with the survival at 10% (d10) was explored, as presented in Figure 4.10. From these results it can be concluded that lower ORP values correlated with increased radioresistance.

4.3 *In vitro* Studies at High dose rate

4.3.1 Photons

Recent findings suggest that changes in reactive oxygen species (ROS), measured as H_2O production, could lead to an increased cellular survival in *in vitro* models when using

ultra high dose rates [36, 52]. To verify such findings, the shutter system described in section 3.4.1 was used.

In this section, the response to different dose rates was investigated using H460 cells. Dosimetry measurements provided dose rate values while using the shutter: a conventional dose rate (CONV) of 0.37 ± 0.02 Gy/s and a high dose rate (HDR) of 13.9 ± 0.7 Gy/s.

The clonogenic survival assay revealed a significant improvement in cell survival when using the HDR geometry compared to the CONV setup with the additional Cu filter, which provides a dose rate of 2.15 Gy/min. However, when cell survival in HDR mode was compared to CONV mode, in which the current of the x-ray tube was reduced and no additional filtration was used, the results matched those observed with the HDR.

It is expected that a lower-energy photon spectrum, present whenever the shutter was in use, would produce secondary electrons with higher linear energy transfer (LET), thereby causing greater damage and consequently reduced cellular survival. However, the results showed an increase in survival for doses greater than 5 Gy for the unfiltered configurations. For example, at a dose value of 8 Gy, the observed survival increment was approximately fourfold, as calculated based on the survival values obtained using the Linear-Quadratic Model (LQM), as despicted in figure 4.13.

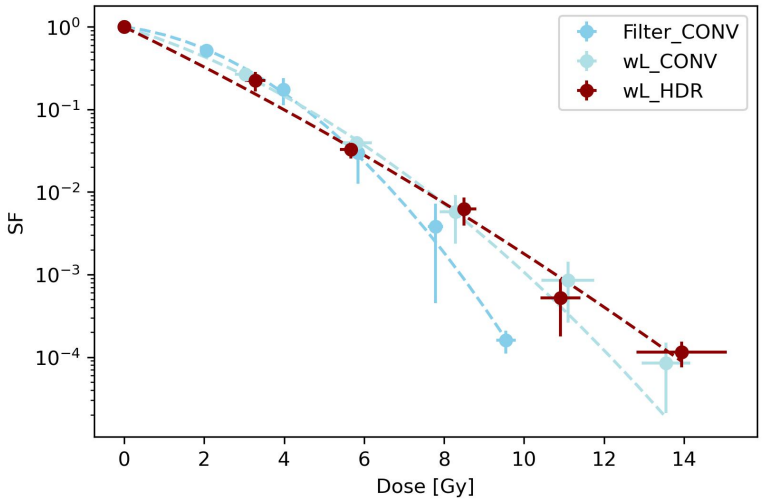

Figure 4.11: Clonogenic survival data obtained for H460 cells in the normal configuration (*Filter CONV:* 220 kV, 17.8 mA, additoinal 0.5 mm Cu filter, dose rate approx. 2.15 Gy/ min), and in the non filtered configurations achieved by the shutter. wL stands for *with liquid*, implying that HBSS was present during irradiation. Dashed lines represent the LQM fit.

The act of placing the sample closer to the x-ray tube makes the field smaller at

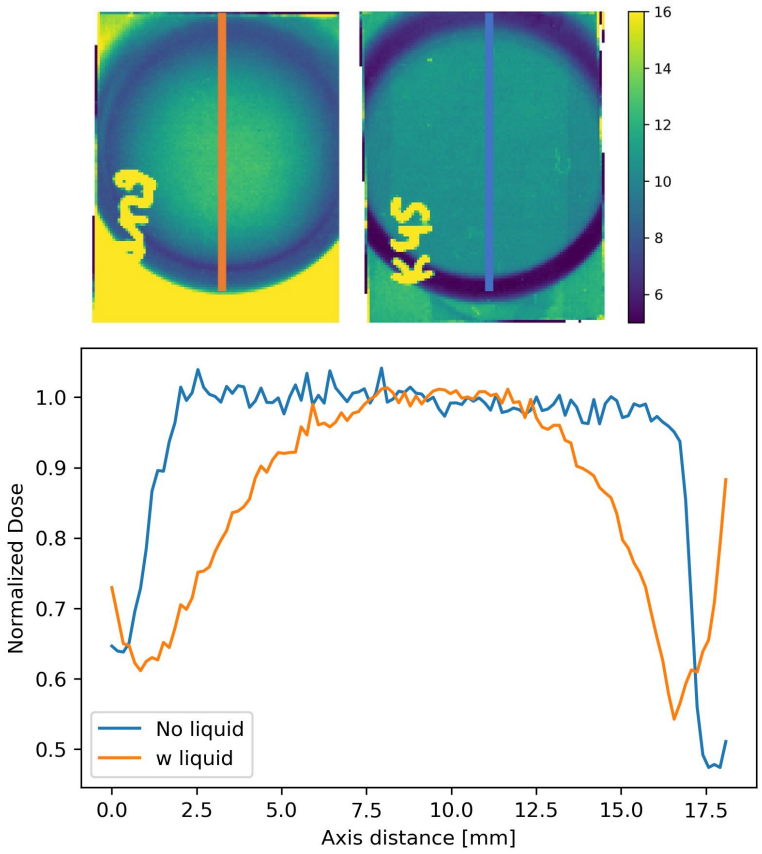

Figure 4.12: Field homogeneity assesment using RF for the shutter experiments. The profiles displayed above illustrate the measurements normalized by the average dose value scored in 3 mm located in the center of the profile.

the given position, increasing the radiation field's inhomogeneity due to the heel effect. So even though improvements were made to enhance irradiation field homogeneity by reducing field size by using a small well as a target, it became evident that further investigations to solve such discrepancies were necessary. Therefore, new measurements of irradiation field homogeneity were conducted. This time, the volume of the liquid inside the well where the cells were seeded was taken into account. The results of these measurements are depicted in Figure 4.12.

Remarkably, the irradiation field was found to be heterogeneous within the well. Analyzing the profiles shown in Figure 4.12, considering the total area of the zone within the well, only 25% of the area was irradiated within a 5% error margin. In contrast, in the profile measured without liquid inside the well, over 90% of the area was uniformly irradiated with the same level of error. Consequently, the clonogenic studies were repeated, this time removing the liquid within the well during irradiation, in order to ensure a homogeneous radiation delivery.

The results of the clonogenic experiments conducted for the H460 and A549 cell lines without liquid in the well during irradiation are shown in Figures 4.13 and 4.14. In this experimental setting,the survival in both cell lines was lower for doses below 10 Gy compared to the results obtained using the copper filter. In particular, in H460 cells, a different behavior was observed between the two dose rates under the shutter configuration. In fact, the survival rate in HDR conditions was up to 9 times lower than that obtained in CONV mode for doses of 2 Gy, 6 Gy, and 10 Gy. However, for doses of 4 Gy and 14 Gy, the values were not distinguishable within uncertainties.

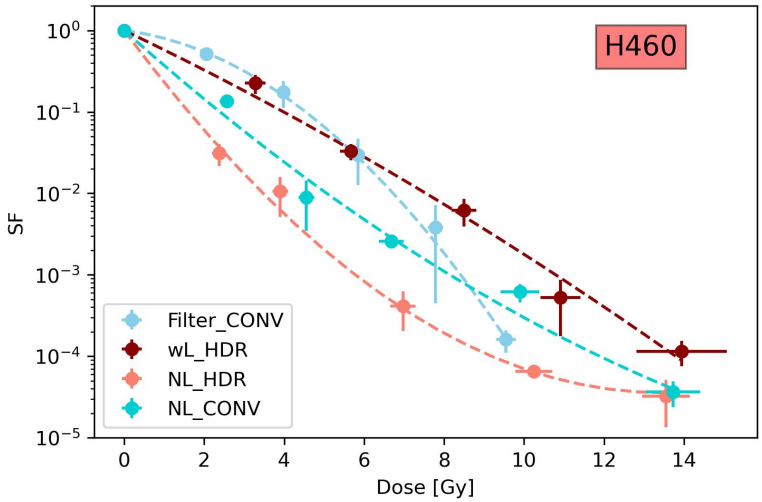

Figure 4.13: Survival assays in H460 cells performed with the shutter compared with the filtered conventional x-ray irradiation. Dashed lines represent LQM fit. *wl = with liquid*, referring to the presence of HBSS in the well during irradiation; *NL* = no liquid, referring to the absence of HBSS during irradiation.

In contrast to H460, no differences were observed for the survival fractions obtained for the A549 cell line (Figure 4.14). Additionally, both setups resulted in lower survival rates compared to the conventional setup, which used the copper filter, for all the studied dose values.

It is important to note that this experiment was conducted only once for each cell line. However, the combination of absence of liquid when irradiating and an unfiltered x-ray beam used with the shutter configuration resulted in an unusual shape of sruvival curves reminiscent of clonogenic assays in hypoxia [63]. Due to these unusual findings, it was decided not to pursue further experimentation with the current shutter setup. However, these preliminary experiments yielded unexpected results, which require further in-depth investigation. Currently, efforts are underway to optimize the shutter setup and improve

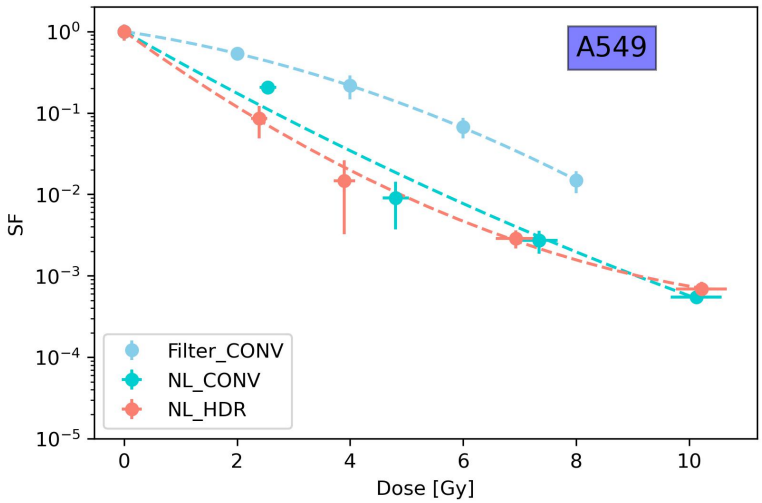

Figure 4.14: Survival assays in A549 cells performed with the shutter compared with the filtered conventional x-ray irradiation. Dashed lines represent LQM fit. *wl* = *with liquid*, referring to the presence of HBSS in the well during irradiation; *NL* = no liquid, referring to the absence of HBSS during irradiation.

dosimetric protocols for improved performances.

4.3.2 Electrons

In order to better analyze cell survival within a more controlled system delivering HDR irradiation, a new set of experiments was performed using the ElectronFlash linac at Antwerp University Hospital. The experimental plan was composed of two studies: (i) SOD activity assays on A549 and H460 cells and (ii) clonogenic survival assays using the same cell lines. In this study, cells were treated with ATN-224, under both CONV and FLASH dose rates.

Preclinical studies provide compelling evidence of ATN-224's mechanism of action, demonstrating its ability to inhibit SOD1 activity [82]. This compound exerts a dual impact on tumor cells. It induces prooxidant effects by elevating superoxide levels while also acting as an antioxidant by diminishing H_2O levels [83]. Moreover, extensive research underscores its notable antitumor and antiangiogenic properties in animal models [84, 85, 86].

The ATN-224 treatment protocol was stablished by following previous research in our group, where different ATN-224 concentrations were tested to reduce SOD activity while maintaining viability [71]. Consequently, a concentration of 60 μM was used for both cell lines, with a treatment duration of 1 hour before irradiation. The samples were

irradiated including the ATN-224 treatment.

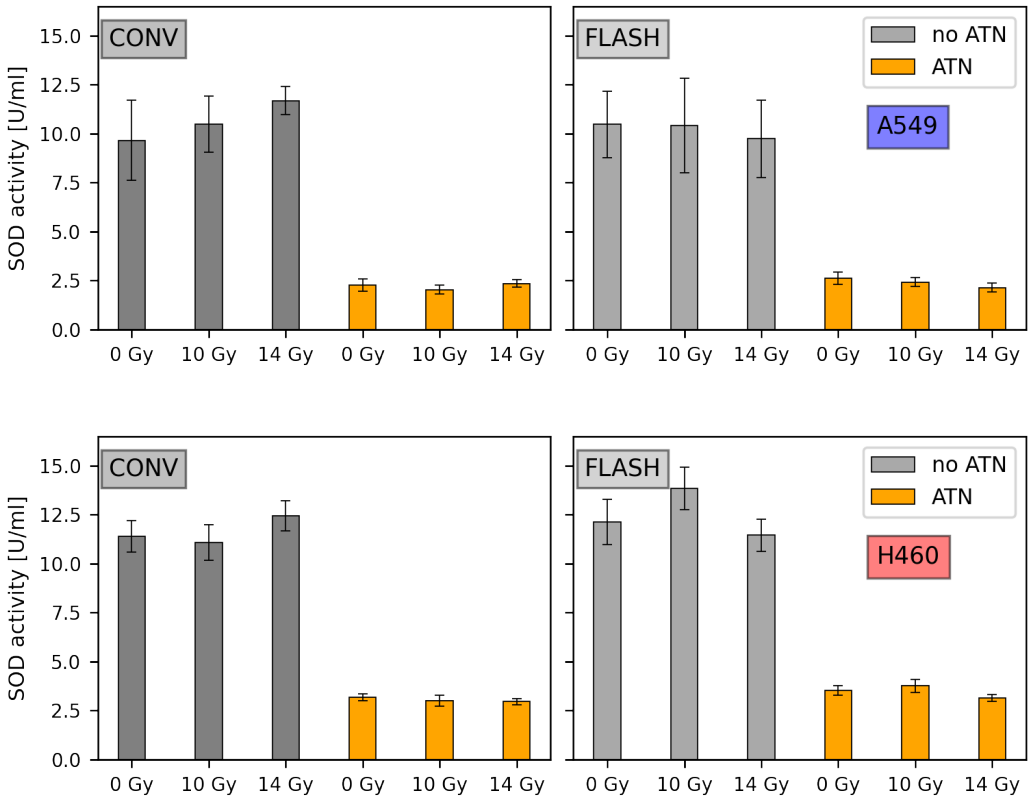

Figure 4.15: SOD activity for the two cell lines A549 and H460 in different conditions. ATN-224 treated samples were treated with 60 µM for 1h (both cell lines).

The SOD activity assessments were performed only for the doses of 0, 10, and 14 Gy, and the results are presented in Figure 4.15. There were no significant differences in SOD activity observed between the two irradiation modes for either cell line. Additionally, within each configuration, there were no significant differences between irradiated samples and the untreated controls. This evidence confirmed that during the irradiation time the inhibition of SOD activity by ATN-224 was present, resulting in more than a 70% reduction in SOD activity for both cell lines. The inhibition was consistent across doses, with no significant differences between the treated 0, 10, and 14 Gy samples. Thus, these results indicate that SOD was equally inhibited during irradiation in both dose rate configurations.

On the other hand, the clonogenic assay results for A549 and H460 cells tested under the four different conditions: untreated and ATN-224-treated cells with either CONV or FLASH electron irradiation, are shown in Figure 4.16. Doses of 2, 5, 10, and 14 Gy were planned in the clonogenic assays. Nevertheless, survival information for 14 Gy was not

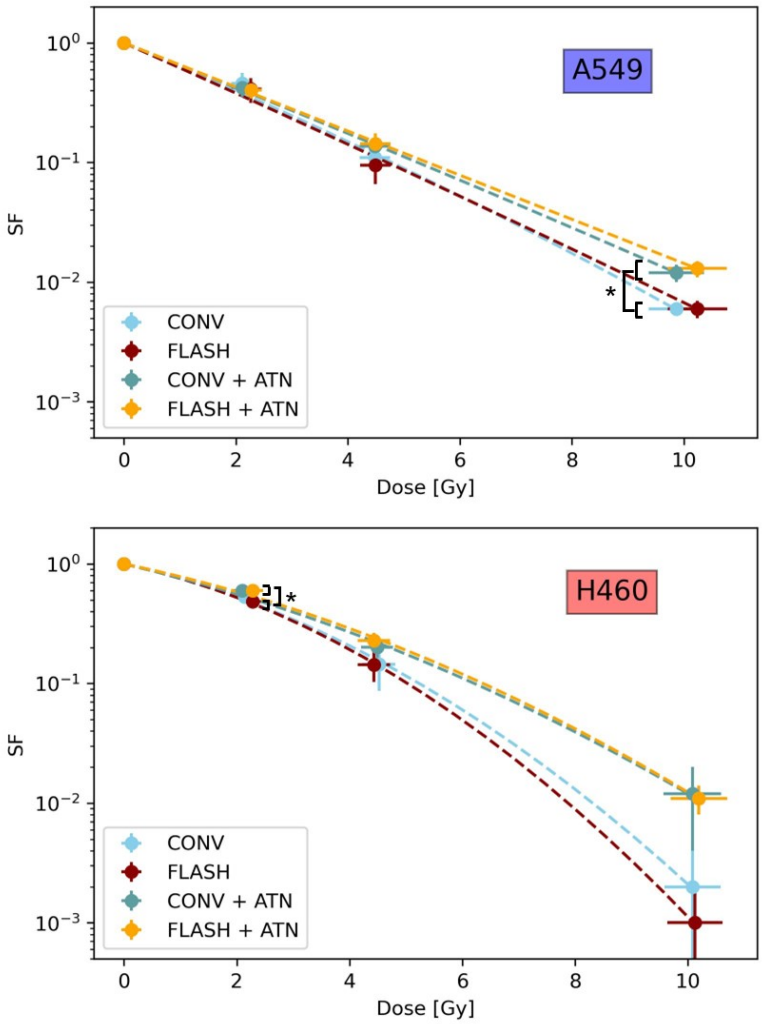

Figure 4.16: Survival curves for untreated and ATN-224 treated (60 µM, 1h, in DMEM) A549 (top) and H460 (bottom) cells, irradiated with electrons in conventional and FLASH dose rate. Average survival from 3 independent experiments are shown.The error bar shown represents the standard deviation from the average values obtained in every experiment.The survival curves were fitted to these according to the LQM, and it is shown by the dashed lines.

possible to assess due to a high survival, making the colony quantification impossible.

For A549 cells, the survival curves for the four tested conditions, fitted with the linear-quadratic model (figure 4.16, top), revealed a significant radioprotective increase in survival at higher doses for the ATN-treated CELLS compared to untreated SAMPLES. In fact, an approximately a 2-fold increase in survival at 10 Gy for both dose rate modes was observed. However, no differences in survival levels were noticed, which could be attributable to the dose rate differences.

For H460 cells, the survival information obtained for all four examined conditions showed no differences between dose rate configurations when comparing the same treatment conditions (Figure 4.16, bottom). Lower cell survival was observed for the untreated

group compared to the ATN-treated groups. Particularly significant differences were also noted between these groups at a dose value of 2 Gy. Given the large uncertainties encountered for 10 Gy, no significance was observed. Nevertheless, the fold-change between the average survival at this dose level between treated and untreated groups was 6 and 11 times for CONV and FLASH dose rates, respectively.

Overall, the protective impact of ATN-224 against radiation was validated through electron irradiation in both conventional and FLASH modes across the examined cell lines. This observation aligns with prior findings from x-ray experiments conducted in conventional mode [71], thus corroborating anticipated outcomes. . The evidence that inhibiting SOD enzyme, responsible for H_2O dismutation, induces higher cell survival in *in vitro* experiments suggests a potential role for this enzyme in protecting cells from irradiation. Additionally, the results here presented show no dose rate survival dependence was observed for neither cell line indicating that similar cancer cell control in vitro could be achieved irrespective of the delivery modality for X-ray and electron irradiation.

Chapter 5

Discussion

Radiotherapy is a widely used cancer treatment, with more than half of all cancer patients requiring it at some stage of the treatment, according to the World Health Organization (WHO). Reactive Oxygen Species (ROS) play a significant role in the cell-killing effect of radiotherapy. This thesis introduces a novel method for assessing hydrogen peroxide (H_2O) production in cell nuclei during irradiation, which serves as a marker for ROS levels, using a H_2O fluorescent marker. The method was validated across varying dose rates and Linear Energy Transfer (LET) levels. Furthermore, the thesis compares the levels of H_2O obtained with existing DNA damage data across three distinct cell lines. Additionally, oxidation-reduction potential (ORP) measurements were utilized to assess the cellular redox state and its impact on cell radioresistance. Finally, the study explores how altering redox states, through the use of a compound that influences the cell's capacity to neutralize superoxide anions, impacts cell survival during UHDR irradiation. Specifically, it examines the potential reduction of hydrogen peroxide production during irradiation by decreasing the activity of the SOD.

5.1 Measuring Hydrogen Peroxide Production during IR in nuclei solution

In the initial phase of this thesis, the production of H_2O during irradiation was evaluated using stained nuclei in solution under varying conditions. To accomplish this, a novel protocol was developed, which led to quantifying the fluorescent intensity of the

supernatant component within the nuclei solution after irradiation.

Previous studies have demonstrated NucPE1's excellent specificity to H_2O and its ability to localize within the cell's nucleus [58]. Recently, it has been used to measure H_2O levels at 30 min, and 24hrs post-irradiation in various lung cancer cell lines [63, 87]. Additionally, comparisons were made between H_2O levels in the nucleus and cytosol with the number of γH2AX foci. In fact, examining H_2O impact on DNA damage can provide information on radiation resistance and antioxidant and pro-oxidant capacities. To enable comparisons between different measurement methods, it is essential first to investigate the quality of the new protocol. This is particularly important considering that the measurements reported in [63] were conducted using nuclei stained and extracted after irradiation. Notably, both studies utilized the same cell lines and irradiation conditions, providing consistency for a comparative analysis.

To validate the effectiveness of the new protocol, data obtained from different components of the nuclei solution (see appendix B) for H460 cells were compared. The results demonstrated that the acquired data accurately reflected the hydrogen peroxide production within the nuclei. Additionally, measuring only the supernatant component of the nuclei solution mitigates any dependence on variations in nuclei size. In addition, by comparing the basal levels of H_2O among the non-irradiated three non-small lung cancer cell lines—H460, Calu-1, and A549—it becomes apparent that H460 cells exhibit a higher basal H_2O level compared to both Calu-1 and A549 cell lines (Figure 4.1). This behavior was in agreement with our previous results reported in Dr. Hanley's Ph.D. Thesis [87]. The higher basal H_2O level observed in H460 cells, as indicated by both protocols, is significant. In Dr. Hanley's thesis, the protocol involved the direct measurement quantification of H_2O in the nuclei by means of flow cytometry, which allows to assess, the fluorescence intensity of individual cells (or nuclei in this case). In contrast, the new method here developed focuses on the supernatant part of the nuclei solution measured using a micro plate reader, which simultaneously allows the detection of the fluorescence intensity from different samples in smaller volumes. It was crucial to demonstrate this approach yielded consistent results to those obtained by directly measuring nuclei.

The findings showed that H_2O increase during irradiation was cell line dependent (Figure 4.1). As mentioned, H460 cells exhibited a higher basal H_2O compared to A549 and Calu-1 cells. Compared to the latter two cell lines, H460 has been proved to have

reduced levels of catalase [87, 88], the enzyme that neutralizes H_2O by descomposing it into water and molecular oxygen, which could explain the latter phenomena.

ROS, particularly H_2O, are known to induce various forms of DNA damage, in particular double-strand breaks (DSBs). DSBs are considered to be more difficult to repair, increasing the probability of cell death, mutation, and transformation [89, 90, 91, 92]. To assess their impact on cell survival, the relationship between DNA DSBs, measured by the formation of γH2AX foci, the hydrogen peroxide production in the nuclei solution (Figure 4.1), and radiosensitivity (Figure 3.2) for the three used cell lines has been examined. Results showed that H460 cells experienced a higher number of γH2AX foci linked with a lower number of H_2O signal, compared with the other two cell lines, and were the most radiosensitive cell line; meanwhile, A549, the most radioresistant cell lines, exhibit the lowest overall DSBs when correlated with the H_2O production. For Calu-1 cells, an intermediate behavior was observed. In fact, at lower doses, the H_2O production hinted to an intermediate damage potential, and the number of γH2AX foci correlated with the levels of H_2O production, thus showing a similar behavior to the one observed in H460 cells. However, at higher doses, although a linear quadratic relationship between hydrogen peroxide and the number of DSBs has been reported in Chinese hamster ovary (CHO) cells [89], here this correlation in nuclei was not inferable, due to the evident saturation effect for the higher dose for both quantities at the higher dose (Figure 4.2).
.

The damaging potential of H_2O can also be observed in the results obtained with increasing the LET by irradiating with protons and helium ions. In this experiment, the results showed that higher LET induced a higher amount of H_2O production (Figure 4.4, and a lower cell survival (Figure 4.5). The increase in relative biological effectiveness (RBE)obtained due to the increased dose averaged LET was found to be in accordance with literature values. The higher H_2O production with increased LET has been previously reported in the literature [64, 65, 93, 94]. It can be explained by the spur theory [65, 95], which posits that for low LET radiation, the reactive intermediates are formed within spurs. These spurs represent small localized regions of energy deposition resulting from the primary particle and secondary electrons; in the high LET case, the spurs are combined to form cylindrical tracks, which increases the probability of combining OH$\cdot$ radicals to form H_2O. However, for LET values larger than 100 keV/μm, a decrease in

the yield of H_2O begins due to intra-track reactions occurring at high LET [65].

The reduced ROS production has been suggested as the determinant factor in protecting adult mouse brains and in the development of Zebrafish embryos exposed to ultra-high dose-rate irradiation [36]. In this work, the quantificatoin of H_2O production in A549 nuclei solution upon high dose rate (HDR) irradiation was performed using a commercial x-ray irradiator. In order to obtain a high dose rate, the copper filter used to harden the photon spectrum have been removed. Due to the known low-energy dependence of the EBT family films [96, 97, 98], the accuracy of the dose measurements was investigated (Appendix A.2. The results from this analysis led to the conclusion that when films are irradiated under a water-equivalent depth of aproximately 2 mm, the dose quantification is adequate within a 5% margin of error, for details refer to Appendix A.3). This might be due to the 8.9 keV tungsten characteristic x-ray. In Figure 5.1, an illustrative reduction of this peak is shown by using available x-ray spectrum data [99] and calculated by attenuation using the linear attenuation coefficient database from NIST [100].

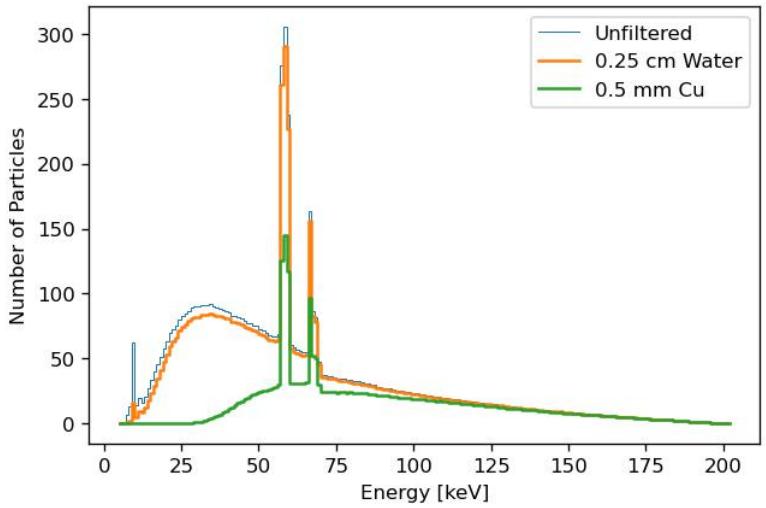

Figure 5.1: Comparison measured spectrum for a 200 kV x-ray tube. Data from [99].

After having a reliable dosimetry protocol, the experiments at HDR were performed. In the setup employed, a high dose rate value limit of approximately 35 Gy/s was obtained (Figure 4.7). This limit was set due to the 1-second irradiation restriction given by the MultiRad 225 available at DKRZ and the positioning of the 35 mm Petri dish. The comparison between a fair non-filtered conventional dose rate configuration, achieved by placing the sample at the longest distance from the x-ray tube exit possible inside

the irradiator, and the HDR irradiation resulted in a decreasing H_2O production trend with increasing dose rate. Nevertheless, a significant difference in H_2O production was not obtained. Indeed, many challenges were encountered that could have influenced the results. First, differences in H_2O amount have been reported at higher doses and dose rates compared to those obtained in the present work. For example, in the work reported by Montay-Gruel et al. [36], a significant difference in H_2O generation was encountered at 80 Gy using a dose rate higher than 100 Gy/s. Additional factors to take into account include the dose inhomogeneity due to the heel effect and variations attributable to the low energy spectrum.

In this section, we have explored the potential of H_2O generation as a marker for radiation-induced damage and its relevance in understanding radiosensitivity. However, it is essential to recognize that relying solely on damage measurements overlooks the importance of damage recognition and repair mechanisms post-radiation [87, 92, 101, 102]. Further research in this area could provide valuable insights into elucidating the complex cellular responses to radiation treatments, thereby advancing our comprehension of radiotherapy efficacy.

5.2 ORP and radiosensitivity

The results presented in Section 4.2 showed an inverse relationship between oxidation-reduction potential (ORP)measured in cell cytosolic extracts and the cell line's radioresistance. While ORP measuring techniques have been previously employed in various contexts, including as an indicator of oxidative status in cellular and bacterial growth media [80, 103], their application in cellular systems poses significant challenges due to their inherent non-specificity. Unlike precise thermodynamic measurements, ORP reflects the overall oxidation-reduction capacity of the system [80]. In addition, the dynamic nature of biological systems, characterized by continuous fluxes and non-equilibrium conditions, makes ORP measurements as stationary potentials rather than thermodynamically accurate values [80]. Finally, factors such as pH, dissolved oxygen concentration, and temperature further influence the oxidative reduction potential [80].

Cancer cells are known for their redox imbalance driven by alterations in endogenous oxidants and antioxidants, therefore exhibiting increased oxidative stress [80]. Cancer

cells employ robust antioxidant defense mechanisms to counteract excessive reactive oxygen species (ROS) and maintain redox homeostasis [80]. Glutathione plays a vital role in this regard, existing in equilibrium between its reduced (GSH) and oxidized form (GSSG) and influencing the thiol redox potential of the cell [104]. The ratio GSH/GSSG has been established as a tool to determine the extent of oxidative stress in the cell [105]; when cells experience more oxidative stress, there is an accumulation of GSSG, leading to a decrease in the GSH/GSSG ratio.

In our previous work [63], the GSH/GSSG ratio was measured for H460, A549, and Calu-1 cell lines in normoxic and hypoxic conditions, obtaining values of 6.9 ($\pm$ 0.53), 6.64 ($\pm$ 0.98), and 12.87 ($\pm$ 0.28) for H460, A549, and Calu-1, respectively. Assuming that both ORP measurements and GSH/GSSG ratios provide equivalent information about the cellular redox status, we anticipate A549 and H460 to exhibit similar ORP values, with Calu-1 displaying a lower value. However, the ORP measurements revealed that A549 and Calu-1 exhibited similar values, whereas H460 had a higher ORP. This illustrates that ORP values represent a broader measure of oxidation-reduction potential. In contrast, the GSH/GSSG ratio explicitly reflects a single enzyme's contribution to the cell antioxidant defense system. Additionally, these differences in ORP values may better explain the observed radiosensitivity variations among the cell lines, with A549 and Calu-1 exhibiting similar radioresistance profiles and H460 displaying a higher radiosensitivity.

While the methodology employed may not yield exact ORP measurements, it does provide a robust qualitative analysis. This approach could be expanded to investigate responses in diverse environments, such as hypoxia, where an increase in GSH/GSSG ratio was observed for the three lung cancer cell lines [63]. Furthermore, ongoing efforts are underway to enhance our understanding of the ORP methodology.

5.3 Optimization of a high dose rate platform for the MultiRad225

As detailed in Section 4.3.1, a shutter was designed to address the challenges encountered while utilizing the MultiRad225 irradiator for high dose rate delivery. Of particular significance was the 1-second irradiation limitation, as this duration is insufficient for the ramp-up period during which the dose rate escalates from zero to the steady-state output

[106], resulting in inconsistent output for every delivery. The shutter facilitated irradiations for 0.1, 0.2, 0.4, 0.6, 0.8, and 1-second intervals. It is important to note that the copper filter was removed during irradiation with the shutter. For irradiation with a potential of 225 kV, the sample was positioned 80.6 mm distant from the source, obtaining a conventional dose rate measurement of 0.37 ± 0.02 Gy/s by lowering the current of the x-ray tube to 0.5 mA, while the high dose rate configuration (HDR) a dose rate of 13.9 ± 0.7 Gy/s was obtained, using a current of 17.8 mA. To address the inconsistent output, a decision was made to irradiate for 4 seconds and activate the shutter's rotating mechanism at the two-second mark. In order to mitigate inhomogeneity attributed to the heel effect present in x-ray tubes [7], the target size was reduced by using sectioned single circular wells, with a diameter of 15.7 mm, derived from a 24-well plate.

Interest arose in investigating the radioprotective effect of FLASH radiotherapy which has been observed in *in vitro* models [107] using the MultiRad225 irradiator. Consequently, clonogenic experiments were conducted using the shutter and irradiating cells seeded in wells containing a small volume of liquid (HBSS). These initial experiments revealed increased cell survival for H460 in both HDR and Conv configurations compared to the ones obtained with a filtered x-ray beam (Figure 4.11). This observation was attributed to the utilization of an unfiltered beam. Contrary to expectations, the anticipated decrease in cell survival was not observed. This was surprising given the low-energy photon spectrum produced by irradiating without the Cu filter. This spectrum yields low-energy secondary electrons which have a higher Linear Energy Transfer (LET) compared to the filtered configuration. The higher LET is thought to contribute to decreased cell survival. However, the observed results did not align with this hypothesis

The experiment outcomes mentioned in the last paragraph prompted a reevaluation of the dosimetry and a reassessment of field homogeneity. Given the use of a very low energy photon spectrum and previous dosimetric assessments performed during the RF study (Appendix A.2), concerns were raised regarding the potential impact of attenuation by the HBSS present in the well during irradiation. Subsequent analysis revealed ongoing field inhomogeneity (Figure 4.12), with only 25% of the area irradiated within a 5% error margin. Indeed, the observed inhomogeneity was associated with a meniscus effect, characterized by a higher volume of HBSS present along the walls of the well compared to the central region.

To mitigate the field inhomogeneity and ensure uniform irradiation in the clonogenic assays (Figure 4.12), these were conducted without liquid by removing the HBSS immediately before irradiation. The assays were then performed under these conditions for H460 and A549 cell lines (Figure 4.13 and 4.14), revealing decreased cell survival for unfiltered configurations compared to filtered one for both cell lines. Notably, the A549 cell line exhibited no differences in the survival fraction with changes in dose rate. On the other hand, H460 experienced a higher cell survival for the Conv configuration for doses lower than 12 Gy. Additionally, no difference was observed for the highest dose (14 Gy) in both configurations (CONV and HDR) for H460 cells. The behavior observed for H460, contrary to the expected dose rate dependence, is noteworthy. Typically, the protective effect of the FLASH effect reported in vitro is observed at high doses during ultra high dose rate irradiation [36, 108, 109, 110], which aligns with findings from in vivo models [111, 112, 113]. These preliminary observations seem promising, however additional research is necessary to validate the initial findings and potentially provide a more comprehensive understanding of the mechanisms underlying these effects.

While ensuring field homogeneity, the expected LET dependence was observed, indicating higher radiosensitivity with the unfiltered spectrum than the filtered one for both cell lines; despite this observation, improvements are required for the irradiation platform. The current dose rate remains significantly lower than that established for the FLASH effect, sometimes defined as exceeding 100 Gy/s [34]. Furthermore, utilizing a non-filtered beam introduces dosimetric complexities and potential irradiation inhomogeneities. Nevertheless, similar irradiation platforms based on orthovoltage x-ray tubes have demonstrated advancements in dose rate capabilities [113, 114, 115], highlighting potential pathways for improvement in our system.

5.4 ATN-224 with electron irradiation in conventional and UHD dose rates

The experiment conducted using the ElectronFlash linac at Antwerp University Hospital provided valuable insights into the impact of ATN-224 treatment in combination with electron irradiation delivered in both CONV and FLASH modes on the SOD activity and clonogenic survival of A549 and H460 lung cancer cell lines.

Superoxide dismutase activity assays revealed a consistent inhibition of SOD activity by using 60 μM ATN-224 in both A549 and H460 cell lines during the irradiation time. Moreover, this inhibition was irrespective of the irradiation mode (CONV or FLASH) or the dose administered. This inhibition underscores the potential of ATN-224 in modulating the cellular redox environment, which is crucial for mitigating oxidative stress induced by radiation therapy.

Furthermore, clonogenic survival assays demonstrated a radioprotective effect of ATN-224 treatment, particularly at higher doses, for both A549 and H460 cells. The observed radioprotective effect of ATN-224 was independent of the dose rate and suggests its efficacy in enhancing cell survival under various irradiation conditions.

The radioprotection may be attributed, in part, to the ability of ATN-224 to inactivate the enzyme SOD1 [82], therefore diminishing the amount of H_2O produced due to water radiolysis. This would lead to a higher accumulation of superoxide ($O_2^{\cdot -}$), which could be differently reduced to hydrogen peroxide, or it could act as a reductant and converted to oxygen [116].

Furthermore, ATN-224 role as a copper chelator could further contribute to its radioprotective effects. By chelating copper ions, ATN-224 could inhibit Fenton-like reactions within the cells. These reactions involve the generation of hydroxyl radicals from hydrogen peroxide in the presence of transition metals such as iron or copper [117]. Hydroxyl radicals are highly reactive and can cause extensive damage to cellular components, including DNA, lipids, and proteins, leading to cell death [118]. Therefore, by inhibiting Fenton-like reactions, ATN-224 may reduce the production of hydroxyl radicals and mitigate the damaging potential of radiation-induced oxidative stress.

When comparing the effectiveness of ATN-224 treatment in protecting against radiation, a greater increase in survival in the H460 cell line compared to the A549 cells was observed. This difference may be attributed to the greater sensitivity of H460 cells to hydrogen peroxide (H_2O), as indicated by their lower catalase levels [87, 88, 119]. The reduction in hydrogen peroxide production would likely have a more significant impact on H460 cells, given their increased vulnerability to H_2O accumulation, resulting in a greater improvement in their survival after irradiation.

When comparing the effectiveness of ATN-224 treatment in protecting against radiation, we noticed a more significant benefit in the H460 cell line compared to the A549

cells. It could be speculated that this difference may be attributed to the similar levels of GSH/GSSG ratio levels between the two cell lines, suggesting comparable antioxidant capacity. However, H460 cells have lower catalase levels [87, 88, 119], which could make them more vulnerable to H_2O accumulation during radiatoin treatments. On the contrary, when treated with ATN-224, the increased sensitivity of H460 cells to H_2O might contribute to the greater radioprotection.

The comparison of the effects of UHDR and conventional irradiation, both with and without ATN-224 treatment, was based on evidence suggesting distinct H_2O production dynamics during UHDR irradiation, which could align with the mechanism of action of the SOD1 inhibitor and could give insights into the FLASH effect mechanism. However, the results did not reveal any noticeable differences between UHDR and conventional irradiation in treated or untreated scenarios. There could be several explanations for these findings, For example, it is suggested that factors such as low pulse doses, the specific focus on tumor cells, and the atmospheric oxygen levels in laboratory conditions might contribute to the lack of a dose rate effect *in vitro* [120]. Additionally, it has been theorized that the dose-rate needed for a FLASH sparing effect may vary depending on the tissue, model or assay being used [113].

The radioprotective effects of ATN-224 remained consistent across the two irradiation modes. Therefore, further research is required to elucidate the specific impacts of dose rate and ATN-224 treatment on cell survival. Future experiments should aim to compare the extent of radioprotection conferred by dose rate alone versus that provided by ATN-224 treatment, allowing for a better understanding of their respective impacts on cell survival.

Chapter 6

Conclusions

Radiotherapy is a fundamental component in cancer treatment, relying on generating reactive oxygen species (ROS) to induce cell death. This thesis focuses on studying the role of reactive oxygen species in the cellular response to radiation.

The initial phase of this project involved developing and validating a novel method for assessing H_2Oproduction in cell nuclei solution during irradiation. This method utilized the H_2Ofluorescent nuclear marker NucPE1, which is a reliable tool for quantifying ROS levels across different cell lines and irradiation conditions. The results demonstrated cell line-dependent variations in radiation-induced H_2O production. Specifically, H460 cells exhibited a higher H_2O increase rate than A549 and Calu-1 cells for lower doses, indicating potentially poorer protection against H_2O production.

The correlation between H_2O levels and DNA damage, as indicated by γH2AX foci formation, provided insights into the relationship between ROS production and radiosensitivity. We found that H460 cells, characterized by higher H_2O levels, exhibited increased DNA damage and greater radiosensitivity compared to A549 and Calu-1 cells. These findings highlight the importance of ROS in modulating cellular responses to radiation and confirm the relevance of H_2O as a potential biomarker for ROS-induced damage.

The assessment method for H_2O was evaluated using two distinct approaches. It is known that the yield of H_2O production in water under radiation exposure can be influenced by the Linear Energy Transfer (LET) and the dose rate. As expected, higher LET led to increased H_2O production in the nuclei solution, attributed to variations in chemical spur formation. Furthermore, considering the reported decrease in H_2O production with increasing dose rates, the irradiation procedure was modified using a

commercial x-ray tube, thereby achieving higher dose rates by removing the additional filtration typically used and decreasing the distance between the tube and the sample. While this study did not yield conclusive outcomes, it revealed a consistent trend aligning with expected behavior.

Additionally, the research on the cellular redox state, as measured by oxidation-reduction potential (ORP), revealed an inverse relationship between ORP and radioresistance. Cancer cells with higher ORP values, indicative of increased oxidative stress, displayed greater radiosensitivity. This association between redox status and radiosensitivity highlights the complex interplay between ROS, antioxidant defenses, and cellular response mechanisms.

Significant advancements were made in HDR delivery using the MultiRad225, particularly with the optimization of the first irradiation platform. However, challenges were encountered when using a very low photon spectrum to irradiate cells in vitro, underscoring the critical importance of addressing this aspect in future research.

Finally, the findings presented in this thesis revealed potential implications for radioresistance driven by changes in hydrogen peroxide (H_2O) production in response to electron irradiation, observed in the use of the superoxide dismutase (SOD) inhibitor compound ATN-224. ATN-224's ability to inhibit SOD activity and modulate cellular redox balance demonstrated efficacy in mitigating radiation-induced toxicity.

Looking ahead, the insights gained from this thesis serves as a foundation for ongoing research topics. Future investigations include exploring live-cell imaging using the NucPE1 marker during irradiation, extending the predictive potential of ORP to different cell lines and hypoxic conditions, and assessing the impact of ROS production in the context of FLASH radiotherapy. These efforts aim to advance our understanding of ROS-mediated responses to radiation and the improvement of therapeutic strategies to enhance cancer treatment outcomes.

Appendix

A Radiochromic Film Dosimetry

The radiochromic film (RF) is a dosimeter considered essential in clinical dosimetry due to its relative energy independence, water equivalence, and high spatial resolution [121]. Its operation is based on reactions which lead to the discoloration of the active medium by radiation absorption.

When the RF is exposed to ionizing radiation, a polymerization reaction occurs in its active layer, leading to darkening of the film. This opacity is quantified using a light transmission factor and measured through optical density, defined as:

$$OD = log_{10}\frac{I_0}{I} \tag{1}$$

where I_0 is the pixel value obtained in a region of interest (ROI) when digitizing the RF before irradiation, and I is the pixel value obtained following the same procedure for the irradiated RF [121], when evaluated with a flatbed scanner.

A.1 Handling and calibration

As RFs are a type of passive dosimeter, they require calibration before use [122]. During calibration, a given number of films from the same batch are exposed to known dose levels, followed by a mathematical adjustment process. For this purpose, EBT-XD films, lot number 01182201 (Ashland), were cut to 1.5 cm x 2 cm. Based on experimental results, it is suitable to use radiochromic EBT-XD films for dose rates up to 2×10^4 Gy/s without adjustments to the response required [123], which suits all the experiments realized in this work. Before irradiation and 24 hrs after the cutting process, the films were digitized using an EPSON Expression 10000XL scanner in TIFF format with a resolution of 150

dpi and 48-bit color, in portrait orientation with color correction disabled. The flatbed scanner was warmed up for 1 hour before every use.

To ensure reproducibility in the positioning of the radiochromic film when being scanned, cardboard frames were employed. These frames served as templates or masks to consistently position the film in the same section of the scanner's surface (Figure 1). International recommendations for handling radiochromic films [124, 125], were followed, both in calibration and dosimetric measurements. Among the recommendations followed were:

- RF handled by the edges, preferably with gloves to avoid leaving fingerprints.
- Avoid pressing them onto non-uniform surfaces as they can be easily scratched.
- Minimum waiting time after cutting the films of 24 hours was allowed before using them.
- RF were stored in a dark environment whenever not in use.
- After IR, films are left to develop for at least 24.
- Stick to the same procedure followed during film calibration to perform dosimetric measurements.

After scanning, the digitized film images were analyzed using Fiji [126] by splitting the image data into individual color channels (red, green, and blue). A square region of interest of 7 mm^2 was used to extract the mean pixel value (I_0) and its standard deviation (σ_{I_0}).

Figure 1: Photos of the irradiation setup for RF calibration (left) and the scanning process (right).

The Semiflex ionization chamber (IC) 31010 (SN 007734) was used to measure the dose rate at a reference position based on the calibration geometry taken from the calibration certificate. In short, dose measurements were obtained for different irradiation times using 200 kV, with 5 mm Cu filtering and x-rays. IC measurements were performed following international protocols [127]; in particular, the readings were corrected by the influence of temperature pressure and polarity.

Once the dose rate was obtained, the RFs were placed in the same position as the reference point of the IC and irradiated using doses ranging from 0 to 30 Gy. For each radiation dose, three films were individually irradiated. After irradiation, the films were stored in a dark environment and left to develop for at least 24 hours before being digitized.

After scanning the films, the same analysis using ImageJ was performed. The pixel value I and the standard deviation σ_I are obtained in this case.

The calibration is based in the method proposed by Devic *et al.* [128], where the net optical density ($netOD$) is calculated for each ROI as:

$$netOD = OD_{after} - OD_{before} = log_{10}\frac{I_0}{I}, \tag{2}$$

with the uncertainty calculated by Gaussian propagation:

$$\sigma_{netOD} = \frac{1}{ln(10)}\sqrt{\left(\frac{\sigma_{I_0}}{I_0}\right)^2 + \left(\frac{\sigma_I}{I}\right)^2}, \tag{3}$$

For each dose value, three films were individually irradiated. Therefore an average $netOD$ ($\overline{netOD}$) was calculated, and the uncertainty was defined as

$$\sigma_{\overline{netOD}} = \sqrt{\left(\sum_{i=1}^{3}\frac{\sigma^i_{netOD}}{3}\right)^2 + \sigma^2_{film-flim}}, \tag{4}$$

where the superscript i refers to the i-th film irradiated with the same dose and $\sigma^2_{film-flim}$ is the variance between the different $netOD$ obtained for the same dose.

After obtaining the net optical density values, a fit was adjusted using the non-linear least squares method *curve fit* from the *scipy.optimize* Python package, as a function of the dose, using the following expression:

$$D(a, b, n, netOD) = a \cdot netOD + b \cdot netOD^n \tag{5}$$

Moreover, its uncertainty was calculated as follows:

$$\sigma_D = \sqrt{netOD^2 \cdot \sigma_a^2 + netOD^{2n} \cdot \sigma_b^2 + (a + n \cdot b \cdot netOD^{n-1})^2 \cdot \sigma_{netOD}^2}, \tag{6}$$

where the parameters a, b, and n where left as free parameters during the fitting process.

Figure 2 shows the results from one of the multiple calibrations performed during this work. After obtaining the parameters a, b, and n for each channel (red, blue, and green) using Equation 5, one can determine the preferred channel by comparing the relative uncertainty and the difference between measurements of the same dose value with both the RF and the IC (see Figure 3). In our case, the red channel was the best option; therefore, all dosimetric measurements were used using this channel. The detailed comparison between channel responses can be found elsewhere [73]

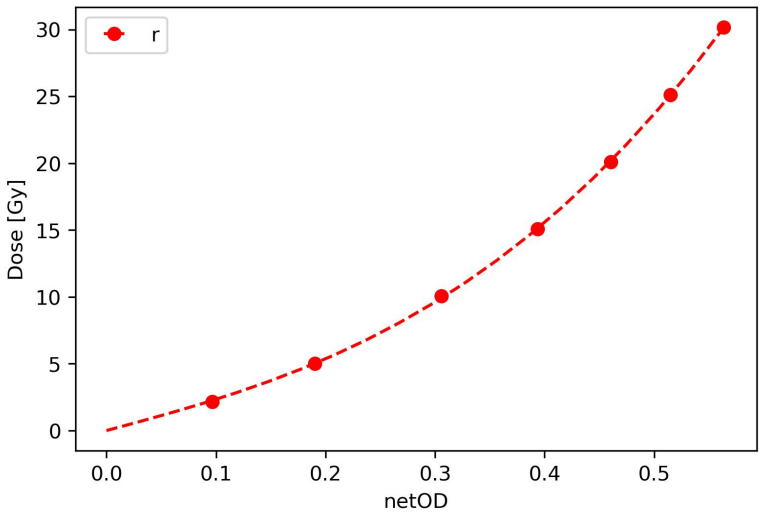

Figure 2: Example of a dose-response curve. Dose as a function of netOD measured by the radiochromic films for the red channel. Modified from [73]

Given the relationship obtained by Equation 5, dose measurements within 4% standard deviation (k = 1) can be performed in the 2 - 30 Gy dose range. The methods described previously can be applied to other radiation qualities with prior knowledge of the dose on a defined geometry.

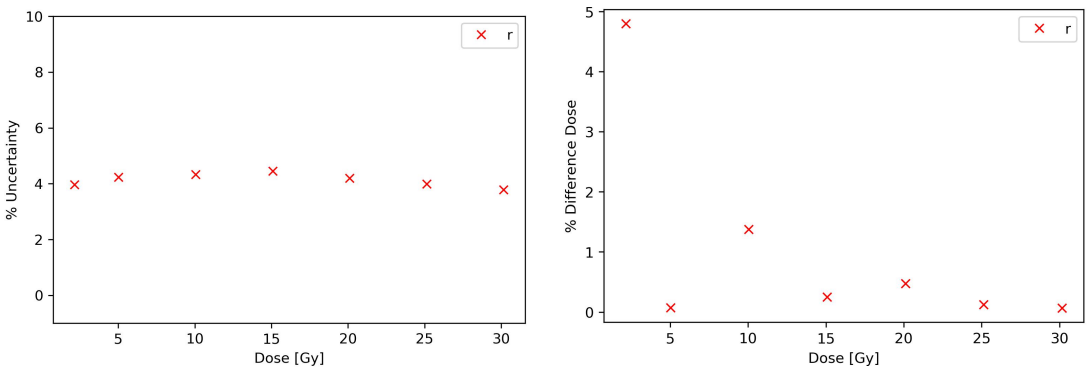

Figure 3: Total dose uncertainty in percentage (left) and the difference between dose measurements with the radiochromic films and the reference ionization chamber (right) obtained for the red channel. Modified from [73].

A.2 RF response Study to an unfiltered x-ray beam

Due to the interest in performing experiments using an unfiltered x-ray beam and the low energy dependence [97], and the need for accurate dosimetric measurements, a comparison between the RF dose measurements and the ones performed with a Markus Plane-Parallel Ion Chamber (model N23343) was carried out.

Markus Chamber Cross Calibration

First, the Markus Chamber was cross-calibrated against a Semiflex Chamber 0.125 cm^3 Type 31010 dosimeter used as a reference by the DKFZ dosimetry team. Based on the $N_{D,w}$ formalism followed by international protocols to measure absorbed dose [127, 129], the calibration factor in terms of absorbed dose to water for the field ionization chamber is given by:

$$N_{D,w}^{field} = \frac{M_{ref}}{M_{field}} N_{D,w}^{ref}, \tag{7}$$

where M_{ref} and M_{field} are the readings per unit of time for the reference and field chambers. respectively, and corrected for the influence quantities $k_{T,p}$ and k_{ion}.

The measurements (M_{ref} and M_{field}) were performed by positioning the reference point of each detector at a depth equivalent to 5 cm of water by using RW3 slabs as shown in Figure 4. The irradiations were performed for three different irradiation times using 200 kV x-rays with an additional 0.5 mm Cu filtration.

The calibration factor obtained for the Markus Chamber was 5.911 x 10^8 Gy/C with

a combined uncertainty of 4% (k = 1).

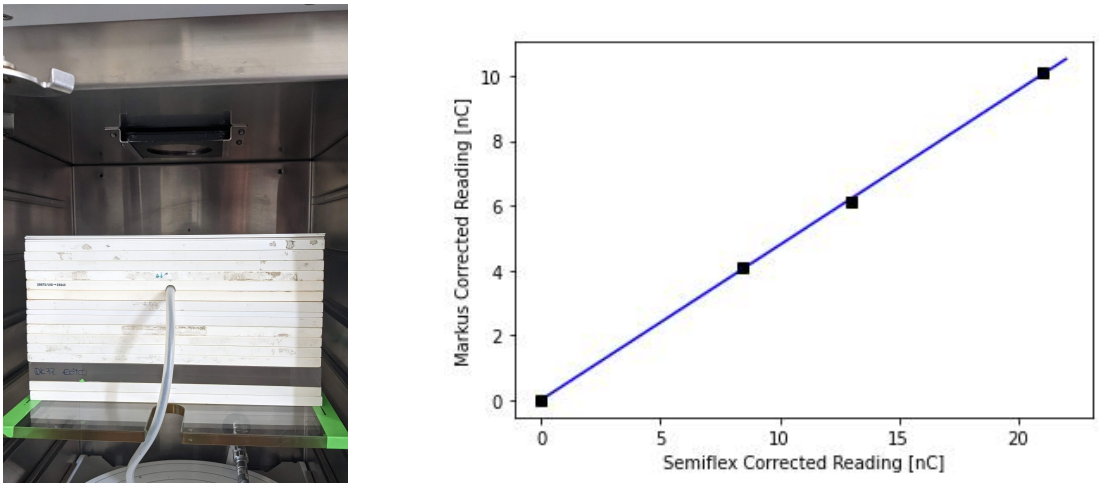

Figure 4: Cross calibration Markus Chamber. Left: Experimental setup used for the cross-calibration. Right: Linear relationship between corrected readings acquired for different irradiation times.

Response Study

Once the Markus Chamber was cross-calibrated, absolute dose measurements at different RW3 depths were performed with both RF and the Markus Chamber, irradiating with 200 kV x-rays without additional filtering. The RF calibration was performed as described in Appendix A.1. Due to the possible energy dependence of the Markus chamber, an extra 1.5% type B uncertainty was added as suggested in [127]. The results are shown in Figure 5. In order to expand the comparison to a submilimetric level, an interpolation was performed using CubicSpline function in Python (version 3).

In Figure 6 the difference in percentage of the interpolated data is plotted. A difference in the range of 5% was encountered in the depth range of 1.5 to 3 mm, equivalent to approximately 1.6 to 3.1 mm of water.

The cell experiments that were conducted using 35 mm Petri dishes, and the 15.5 mm wells were irradiated as illustrated on the left side of Figure 6. In order to score the dose that the cells received, a RF was positioned under the the container. The water-equivalent depth where the measurement is usually performed lies in this region. Therefore, the expected error from the dose measurements performed with the RF is within its uncertainties.

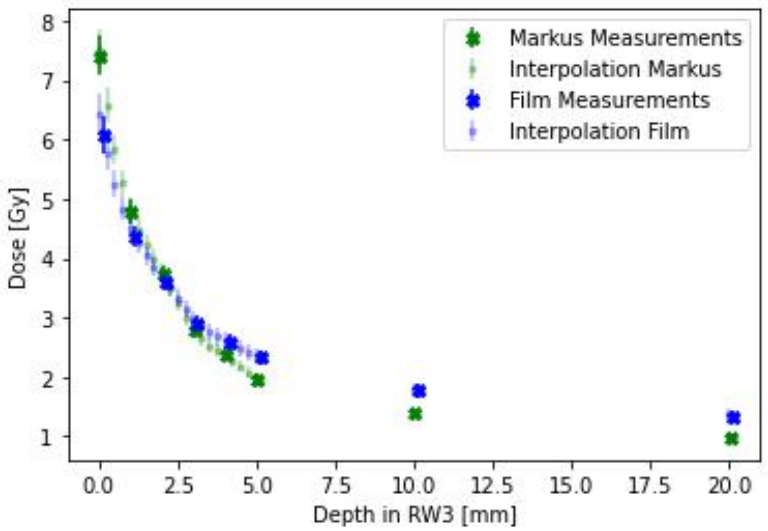

Figure 5: Absolute dose measurements at different RW3 depths performed with EBT XD RF and the Markus Chamber. Interpolation points using the CubicSpline function at intermediate depths are also shown.

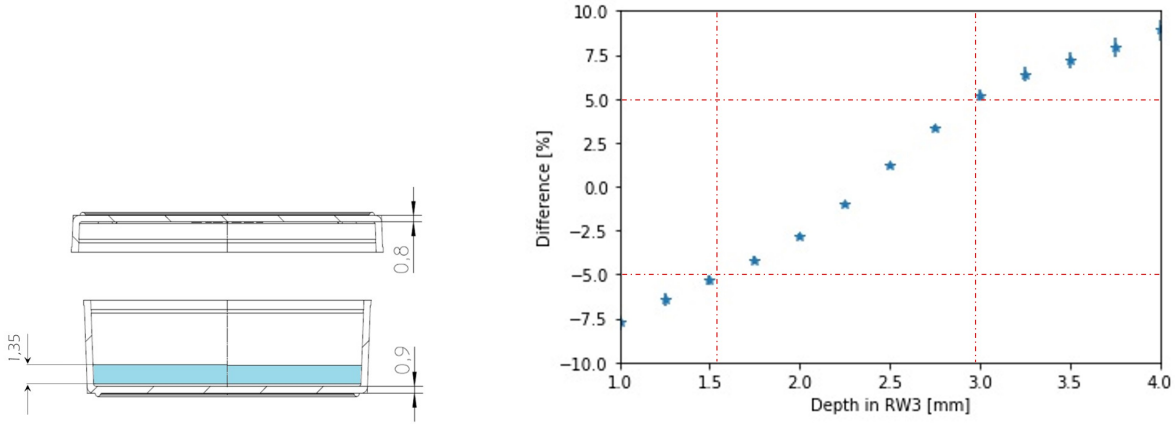

Figure 6: Cross calibration Markus Chamber. Left: Experimental setup used for the cross-calibration. Right: Linear relationship between corrected readings acquired for different irradiation times.

A.3 In/Out Factor

To estimate the dose received by the cells, a conversion factor was calculated by measuring the dose on the inside and outside surface of the bottom of the container using RF. This conversion factor is referred to as in/out factor. It was calculated by a linear fit to the dose measured outside the bottom of the Petri as a function as the one measured inside it (Figure 7).

The value in/out factor for the 35 mm Petri dishes using 1.3 mL of HBSS was calculated to be 1.28 ± 0.03. This factor was used for all the experiments in this thesis when HBSS was used in the irradiated container.

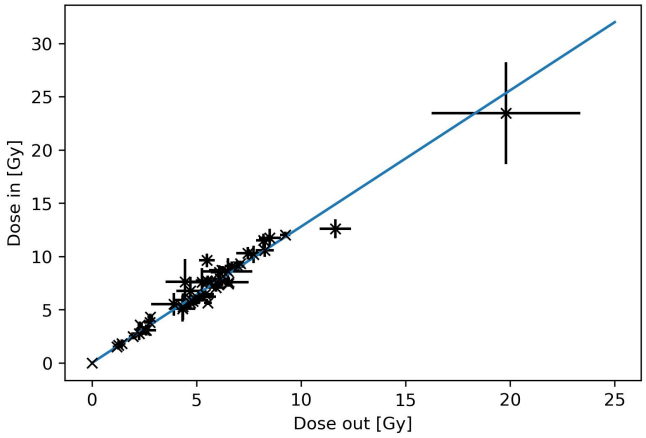

Figure 7: In/out factor. Dose measurements were performed with RF positioned at the inside bottom surface as a function of measurements performed on the outside bottom surface of a petri dish. The in/out factor was calculated as the slope of the linear fit.

B NucPE1 Signal Study

The protocol outlined in Section 3.2 involves nuclei extraction following NucPE1 incubation. Previous experience using NucPE1 has employed various techniques to quantify its fluorescence signal immediately after irradiation. For example, Figure 8 displays cell images taken by a confocal microscope. However, these techniques presented challenges, primarily due to signal weakening or bleaching, leading to inconsistent outcomes.

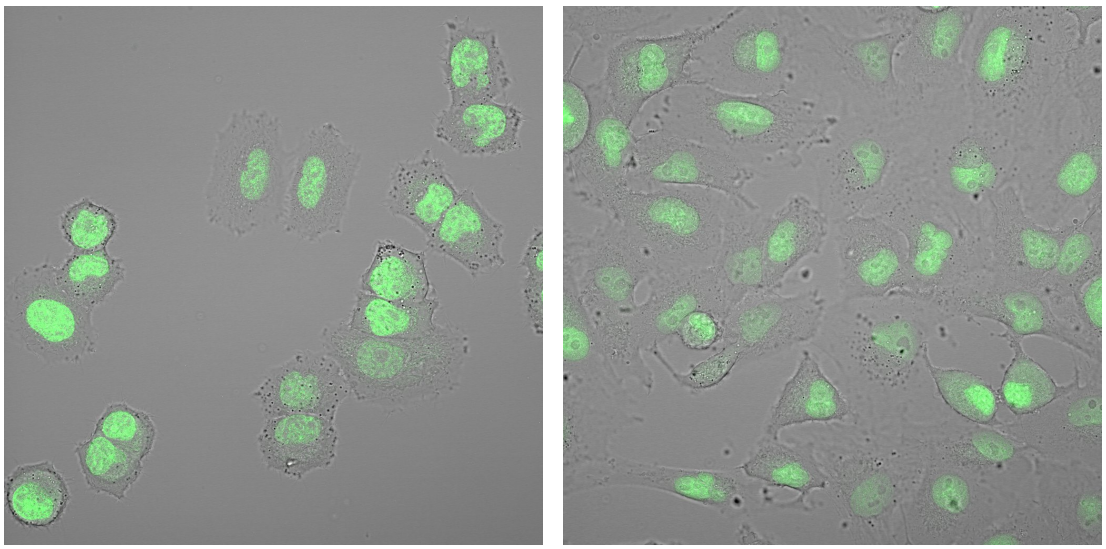

Figure 8: Cells stained with NucPE1. Confocal Images were taken for H460 (left) and Calu-1 (right) cells using 10 μM NucPE1 for 20 minutes.

Since the goal was to measure H_2Oproduction during irradiation, the staining had to be performed before. It was hypothesized that since the H_2O removal in cells is

mediated by very efficient enzymes, the dye's reaction rates were too slow to compete against them. Therefore, whole-cell techniques could be inadequate to monitor the H_2O production. Thus, the new protocol involving nuclei extraction (Figure 9) after staining was developed (Section 3.2).

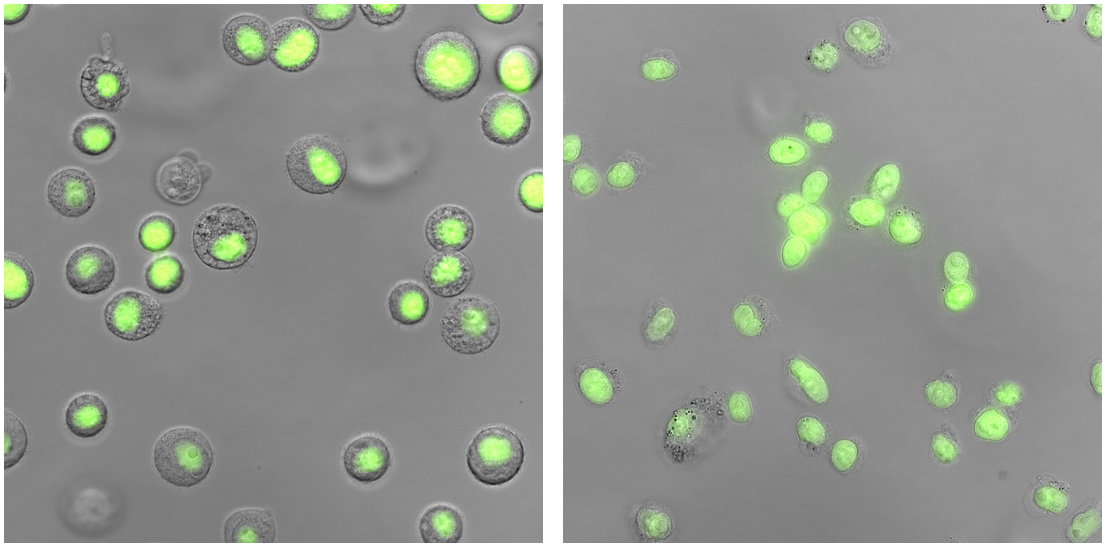

Figure 9: NucPE before and after nuclei extraction. Fluorescence images were taken before (left) and after (right) nuclei extraction for H460 cells.

B.1 Stability over time

After the implementation of the protocol it was essential to investigate the effect of the time that the nuclei solution rests after irradiation, until all samples are irradiated. All samples were kept in a dark environment and under a controlled temperature during the resting time.

The effect was quantified by comparing the fluorescent signal after different resting times for an irradiated sample (4 Gy using 200 kV x-ray with 5 mm Cu additional filtration) and an unirradiated sample. The results in Figure 10 indicate no dependency on resting time for any sample. Therefore, different resting times for the various dose values studied following the protocol do not influence the fluorescence measurements.

Additionally, an increase in signal over time is observed for samples left inside the 96-well plate. This phenomenon may be attributed to fluctuations in temperature and exposure to light during the measurement process.

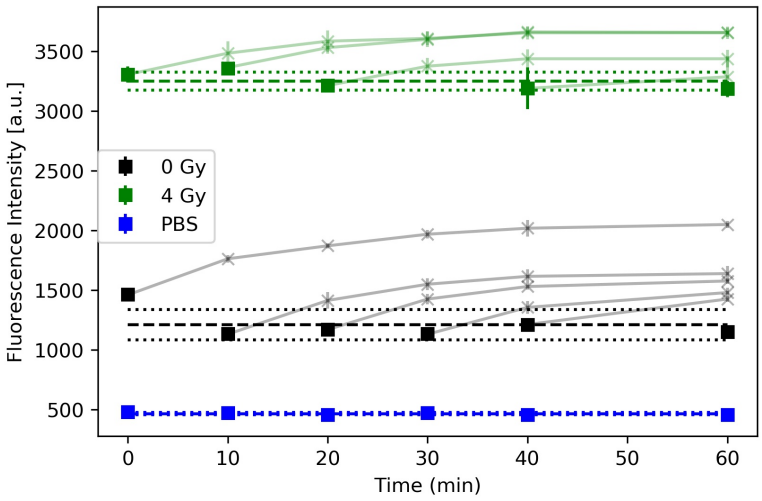

Figure 10: NucPE1 Signal over time. Square data points are the first measurement after a given resting time after irradiation. "x" data points are the measurements of the evolution of the squared measurements over time. Dashed lines are the average values of the square measurements for each sample, and dotted lines are the standard deviation limits of each average.

B.2 Supernatant Study

The protocol involves measuring the supernatant after irradiating and centrifuging nuclei solutions. Since this measurement excludes the presence of nuclei in the wells, it's crucial to determine if this "*regular*" protocol yields comparable results to when nuclei are present in the wells during fluorescence measurement. In simpler terms, the question is whether the measurements of the supernatant alone provide meaningful information or if they're just picking up background noise. This background could potentially arise from DNA damage caused by the nuclei extraction protocol.

For this purpose, the sample after nuclei extraction was prepared in three ways (Figure 11). The first method, labeled as the "*regular*", follows the protocol described in Section 3.2. The second method involved the same preparation as the regular protocol, except for the last step, where the nuclei were resuspended and added into the wells after the final centrifugation, ensuring measuring the nuclei contribution within the nuclei solution. The third method involved centrifugation of the nuclei solution before irradiation, ensuring only the supernatant component of the nuclei solution was irradiated and then measured. The subsequent analysis followed the procedure outlined in Section 3.2.

In Figure 12, the difference in Fluorescence Intensity (FI) per nucleus is compared between the "*regular*" protocol and two alternative methods. A constant difference is

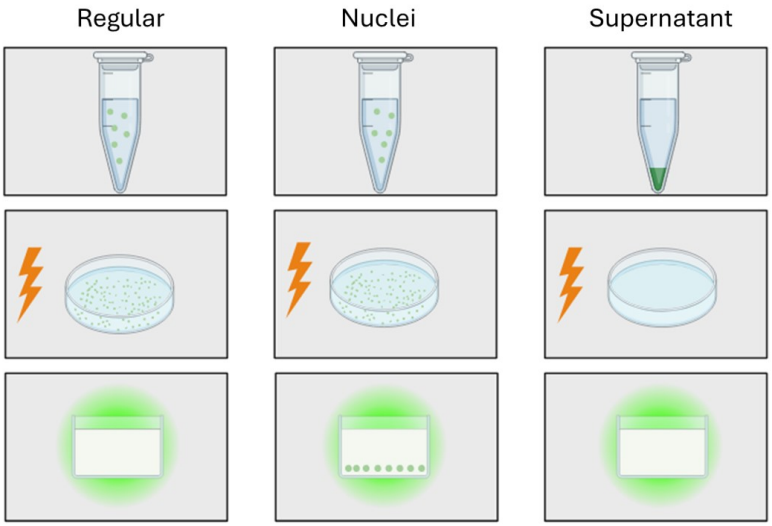

Figure 11: Supernatant Study. To evaluate the influence of the two components of the nuclei solution by modifying the last steps of the method described in Section 3.2. Read the text for detailed information

observed when measuring nuclei versus only the supernatant, likely due to the presence of nuclei during fluorescence measurement. However, a dose-dependent increase is noted compared to the supernatant protocol. This suggests that the protocol accurately reflects the influence of nuclei when irradiated. The similar dose dependence between the regular and nuclei protocols may be attributed to DNA fragmentation [130] or rapid DNA repair processes [131, 132] , although further clarification is needed.

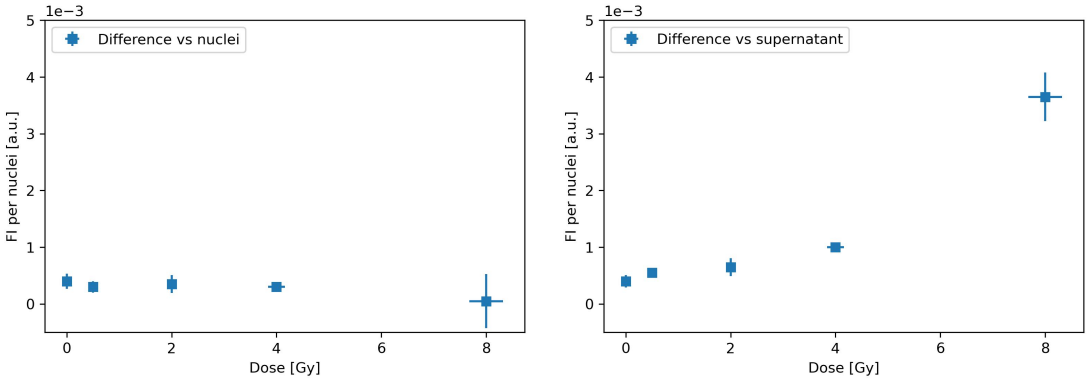

Figure 12: Difference between preparations in the supernatant study. Difference in Fluorescence Intensity (FI) normalized by the number of nuclei measured between the *regular* protocol and measuring nuclei (left) or measuring only supernatant (right).

In conclusion, the combination of NucPE1's nuclear localization and the utilization of a nuclei solution allowed for the avoidance of competition with the cell's antioxidant system, responsible for the removal of H_2O. In addition, the measurement of only the supernatant part after nuclei centrifugation avoids a nucleus size dependence while de-

scribing the nuclei effect during irradiation.

C SOD Activity Measurement

Following the treatment with ATN-224, the SOD Activity in A549 and H460 cells was measured using the SOD activity determination kit (Sigma-Aldrich). The operational principle of the kit (Figure 13, left) is based on the soluble salt WST-1, which generates a water-soluble dye called formazan when it undergoes reduction by superoxide ions ($O_2^{\cdot -}$). This reduction rate is directly proportional to the activity of xanthine oxidase (XO). In the presence of superoxide dismutase (SOD), $O_2^{\cdot -}$ is scavenged, resulting in reduced production of WST-1 formazan dye.

In order to quantitatively determine the SOD Activity (U/mL), a reference calibration curve was established using SOD standard solutions spanning a range from 0.02 U/mL to 818 U/mL (Figure 13, right).

This curve was fitted to a sigmoid function:

$$SOD_{IR} = \frac{L}{1 + e^{(-k(log_{10}(SOD_A)-b)}}, \tag{8}$$

where SOD_{IR} refers to the SOD inhibation rate, a quantity that is calculated by:

$$SOD_{IR}[\%] = \frac{(A_{blank1} - A_{blank2}) - (A_{sample} - A_{blank2})}{(A_{blank1} - A_{blank2})} x100, \tag{9}$$

in this case, A is the absorbance measured with a plate reader at 450 nm from the *sample* of interest or three *blanks* that define the assay's working limits: *Blank1* is composed by water, WST and the enzyme (XO), meanwhile *blank3* is formed by water and WST. In addition, *blank2* corrects the sample measurement by any inherent coloration, and it is prepared with the sample and WST, on the contrary the *sample* is composed by adding XO and WST.

Finally, the SOD Activity in U/mL can be calculated by solving eq. 9 for SOD_A.

In the experiments described in Section 3.4.2 the SOD inhibition was assessed after irradiation. Alliquots of 900.000 cells were taken from the 0, 10 and 14 Gy samples and lysed with a commercial RIPA lysis buffer (Cell signaling technology) completed with 0.01% protease inhibitor. Given that the experiment took place in Antwerp, Belgium,

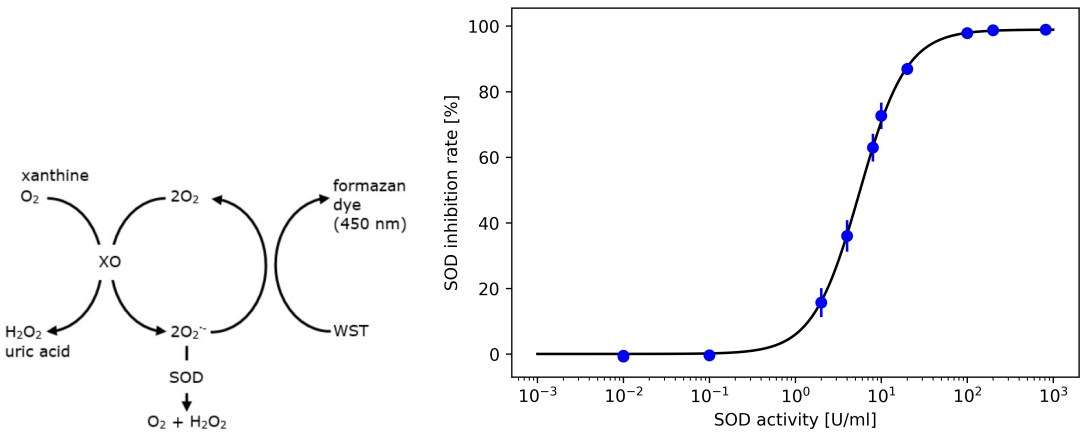

Figure 13: Process of WST formazan dye production, working principle of the SOD activity Kit (Left) and SOD activity calibration curve (Right).

the lyzed samples were kept at -20 °C, and processed a week later in the DKFZ.

List of Figures

Scientific Contributions

Publications

- Muñnoz, I. D., **Garcia-Calderon, D.**, Félix-Bautista, R., Burigo, L. N., Christensen, J. B., Brons, S., Runz, A., Häring, P., Greilich, S., Seco, J., & Jäkel, O. (2024, In Press). Linear energy transfer measurements and estimation of relative biological effectiveness in proton and helium-ion beams using fluorescent nuclear track detectors. International Journal of Radiation Oncology Biology Physics.

- Tirinato, L., Onesto, V., **Garcia-Calderon, D.**, Pagliari, F., Spadea, M. F., Seco, J., & Gentile, F. (2023). Human Cancer Cell Radiation Response Investigated through Topological Analysis of 2D Cell Networks. Annals of Biomedical Engineering, 1-13.

- Hanley, R., Pagliari, F., **Garcia-Calderón, D.**, Fernandes Guerreiro, J., Genard, G., Jansen, J., ... & Seco, J. (2023). Radio-resistance of hypoxic tumors: exploring the effects of oxygen and x-ray radiation on non-small lung cancer cell lines. Radiation Oncology, 18(1), 81.

- Zhang, T., **García-Calderón, D.**, Molina-Hernández, M., Leitão, J., Hesser, J., & Seco, J. (2023). A theoretical study of H2O2 as the surrogate of dose in minibeam radiotherapy, with a diffusion model considering radical removal process. Medical Physics.

- Tirinato, L., Onesto, V., **Garcia-Calderon, D.**, Pagliari, F., Spadea, M. F., Seco, J., & Gentile, F. (2022). Human lung-cancer-cell radioresistance investigated through 2D network topology. Scientific Reports, 12(1), 12980.

- Jansen, J., Beyreuther, E., **García-Calderón, D.**, Karsch, L., Knoll, J., Pawelke,

J., ... & Seco, J. (2022). Changes in Radical Levels as a Cause for the FLASH effect: Impact of beam structure parameters at ultra-high dose rates on oxygen depletion in water. Radiotherapy and Oncology, 175, 193-196.

- Nisticò, C., Pagliari, F., Chiarella, E., Fernandes Guerreiro, J., Marafioti, M. G., Aversa, I., **Garcia-Calderon, D.**, ... & Seco, J. C. (2021). Lipid droplet biosynthesis impairment through DGAT2 inhibition sensitizes MCF7 breast cancer cells to radiation. International journal of molecular sciences, 22(18), 10102.

- Tirinato, L., Marafioti, M. G., Pagliari, F., Jansen, J., Aversa, I., Hanley, R.,**Garcia-Calderon,D.**, ... & Seco, J. (2021). Lipid droplets and ferritin heavy chain: a devilish liaison in human cancer cell radioresistance. Elife, 10, e72943.

Bibliography

[1] Joiner, M. C., & van der Kogel, A. J. (2018). *Basic clinical radiobiology*. CRC press.

[2] Podgorsak, E. B. (2005). *Radiation oncology physics: A handbook for teachers and students*. International Atomic Energy Agency.

[3] Berger, M., Hubbell, J., Seltzer, S., Chang, J., Coursey, J., Sukumar, R., Zucker, D., & Olsen, K. (n.d.). XCOM: Photon cross sections database. *NIST Standard Reference Database 8*. https://doi.org/10.18434/T48G6X

[4] Workman, R. L., et al. (2022). Review of Particle Physics. *PTEP*, *2022*, 083C01. https://doi.org/10.1093/ptep/ptac097

[5] Thomas, D. J. (2011). ICRU report 85: Fundamental quantities and units for ionizing radiation. *11*. https://doi.org/10.1093/jicru/ndr012

[6] Kaiser, A., Eley, J. G., Onyeuku, N. E., Rice, S. R., Wright, C. C., McGovern, N. E., Sank, M., Zhu, M., Vujaskovic, Z., Simone 2nd, C. B., et al. (2019). Proton therapy delivery and its clinical application in select solid tumor malignancies. *JoVE (Journal of Visualized Experiments)*, (144), e58372. https://doi.org/10.3791/58372

[7] Khan, F. M. (2010). *The physics of radiation therapy*. Lippincott Williams & Wilkins.

[8] Attix, F. H. (2008). *Introduction to radiological physics and radiation dosimetry*. John Wiley & Sons.

[9] Weber, U., & Kraft, G. (2009). Comparison of carbon ions versus protons. *The Cancer Journal*, *15*(4), 325–332. https://doi.org/10.1097/PPO.0b013e3181b01935

[10] von Sonntag, C. (1987). The chemical basis of radiation biology. *(No Title)*.

[11] Lodish, H. F. (2008). *Molecular cell biology*. Macmillan.

[12] Sanvictores, T., & Davis, D. D. (2023). Histology, rough endoplasmic reticulum. In *Statpearls [internet]*. StatPearls Publishing.

[13] Hall, E. J., & Giaccia, A. J. (2006). *Radiobiology for the radiologist* (Vol. 6). Philadelphia.

[14] Geacintov, N. E., Broyde, S., et al. (2010). *The chemical biology of dna damage*. Wiley Online Library.

[15] von Sonntag, C. (2006). *Free-radical-induced dna damage and its repair*. Springer.

[16] Ward, J. F. (1998). Nature of lesions formed by ionizing radiation. In *Dna damage and repair: Volume 2: Dna repair in higher eukaryotes* (pp. 65–84). Springer. https://doi.org/10.1007/978-1-59259-455-9_5

[17] Han, W., & Yu, K. (2010). Ionizing radiation, dna double strand break and mutation. *Advances in Genetics research*, *4*, 197–210.

[18] Sies, H. (2021). Oxidative eustress: On constant alert for redox homeostasis. *Redox Biology*, *41*, 101867. https://doi.org/10.1016/j.redox.2021.101867

[19] Dayal, R., Singh, A., Pandey, A., & Mishra, K. P. (2014). Reactive oxygen species as mediator of tumor radiosensitivity. *Journal of cancer research and therapeutics*, *10*(4), 811–818. https://doi.org/10.4103/0973-1482.146073

[20] Ma, Q. (2013). Role of NRF2 in oxidative stress and toxicity. *Annual review of pharmacology and toxicology*, *53*, 401–426. https://doi.org/10.1146/annurev-pharmtox-011112-140320

[21] Puck, T. T., & Marcus, P. I. (1956). Action of x-rays on mammalian cells. *The Journal of experimental medicine*, *103*(5), 653–666. https://doi.org/10.1084/jem.103.5.653

[22] Franken, N. A., Rodermond, H. M., Stap, J., Haveman, J., & Van Bree, C. (2006). Clonogenic assay of cells in vitro. *Nature protocols*, *1*(5), 2315–2319. https://doi.org/10.1038/nprot.2006.339

[23] Deacon, J., Peckham, M., & Steel, G. (1984). The radioresponsiveness of human tumours and the initial slope ofthe cell survival curve. *Radiotherapy and Oncology*, *2*(4), 317–323. https://doi.org/10.1016/S0167-8140(84)80074-2

[24] Fertil, B., & Malaise, E. (1985). Intrinsic radiosensitivity of human cell lines is correlated with radioresponsiveness of human tumors: Analysis of 101 published

survival curves. *International Journal of Radiation Oncology* Biology* Physics*, *11*(9), 1699–1707. https://doi.org/10.1016/0360-3016(85)90223-8

[25] Fertil, B., Dertinger, H., Courdi, A., & Malaise, E. (1984). Mean inactivation dose: A useful concept for intercomparison of human cell survival curves. *Radiation research*, *99*(1), 73–84. https://doi.org/10.2307/3576448

[26] Fertil, B., & Malaise, E.-P. (1981). Inherent cellular radiosensitivity as a basic concept for human tumor radiotherapy. *International Journal of Radiation Oncology* Biology* Physics*, *7*(5), 621–629. https://doi.org/10.1016/0360-3016(81)90377-1

[27] Chang, D. S., Lasley, F. D., Das, I. J., Mendonca, M. S., Dynlacht, J. R., Chang, D. S., Lasley, F. D., Das, I. J., Mendonca, M. S., & Dynlacht, J. R. (2021). Radiation survival models, sld, pld, and dose rate. *Basic Radiotherapy Physics and Biology*, 243–253. https://doi.org/10.1007/978-3-030-61899-5_23

[28] McMahon, S. J. (2018). The linear quadratic model: Usage, interpretation and challenges. *Physics in Medicine & Biology*, *64*(1), 01TR01. https://doi.org/10.1088/1361-6560/aaf26a

[29] Lea, D. E. (1946). Actions of radiations on living cells. *Actions of radiations on living cells.*

[30] Lea, D., & Catcheside, D. (1942). The mechanism of the induction by radiation of chromosome aberrations in tradescantia. *Journal of genetics*, *44*, 216–245.

[31] *Relative biological effectiveness in ion beam therapy.* (2008). INTERNATIONAL ATOMIC ENERGY AGENCY. https://www.iaea.org/publications/7682/relative-biological-effectiveness-in-ion-beam-therapy

[32] Borghini, A., Labate, L., Piccinini, S., Panaino, C. M. V., Andreassi, M. G., & Gizzi, L. A. (2024). Flash radiotherapy: Expectations, challenges, and current knowledge. *International Journal of Molecular Sciences*, *25*(5), 2546. https://doi.org/10.3390/ijms25052546

[33] Favaudon, V., Caplier, L., Monceau, V., Pouzoulet, F., Sayarath, M., Fouillade, C., Poupon, M.-F., Brito, I., Hupé, P., & Bourhis, J. (2014). Ultrahigh dose-rate FLASH irradiation increases the differential response between normal and tumor tissue in mice. *Science translational medicine*, *6*(245), 245ra93–245ra93. https://doi.org/10.1126/scitranslmed.3008973

[34] Limoli, C. L., & Vozenin, M.-C. (2023). Reinventing radiobiology in the light of flash radiotherapy. *Annual Review of Cancer Biology*, *7*, 1–21. https://doi.org/10.1146/annurev-cancerbio-061421-022217

[35] Dewey, D., & Boag, J. (1959). Modification of the oxygen effect when bacteria are given large pulses of radiation. *Nature*, *183*(4673), 1450–1451. https://doi.org/10.1038/1831450a0

[36] Montay-Gruel, P., Acharya, M. M., Petersson, K., Alikhani, L., Yakkala, C., Allen, B. D., Ollivier, J., Petit, B., Jorge, P. G., Syage, A. R., et al. (2019). Long-term neurocognitive benefits of flash radiotherapy driven by reduced reactive oxygen species. *Proceedings of the National Academy of Sciences*, *116*(22), 10943–10951. https://doi.org/10.1073/pnas.1901777116

[37] Montay-Gruel, P., Acharya, M. M., Gonçalves Jorge, P., Petit, B., Petridis, I. G., Fuchs, P., Leavitt, R., Petersson, K., Gondré, M., Ollivier, J., et al. (2021). Hypofractionated flash-rt as an effective treatment against glioblastoma that reduces neurocognitive side effects in mice. *Clinical Cancer Research*, *27*(3), 775–784. https://doi.org/10.1158/1078-0432.CCR-20-0894

[38] Simmons, D. A., Lartey, F. M., Schüler, E., Rafat, M., King, G., Kim, A., Ko, R., Semaan, S., Gonzalez, S., Jenkins, M., et al. (2019). Reduced cognitive deficits after flash irradiation of whole mouse brain are associated with less hippocampal dendritic spine loss and neuroinflammation. *Radiotherapy and Oncology*, *139*, 4–10. https://doi.org/10.1016/j.radonc.2019.06.006

[39] Liljedahl, E., Konradsson, E., Gustafsson, E., Jonsson, K. F., Olofsson, J. K., Ceberg, C., & Redebrandt, H. N. (2022). Long-term anti-tumor effects following both conventional radiotherapy and flash in fully immunocompetent animals with glioblastoma. *Scientific Reports*, *12*(1), 12285. https://doi.org/10.1038/s41598-022-16612-6

[40] Alaghband, Y., Cheeks, S. N., Allen, B. D., Montay-Gruel, P., Doan, N.-L., Petit, B., Jorge, P. G., Giedzinski, E., Acharya, M. M., & Vozenin, M.-C. (2020). Neuroprotection of radiosensitive juvenile mice by ultra-high dose rate flash irradiation. *Cancers*, *12*(6), 1671. https://doi.org/10.3390/cancers12061671

[41] Chabi, S., Van To, T. H., Leavitt, R., Poglio, S., Jorge, P. G., Jaccard, M., Petersson, K., Petit, B., Roméo, P.-H., & Pflumio, F. (2021). Ultra-high-dose-rate

flash and conventional-dose-rate irradiation differentially affect human acute lymphoblastic leukemia and normal hematopoiesis. *International Journal of Radiation Oncology* Biology* Physics*, *109*(3), 819–829. https://doi.org/10.1016/j.ijrobp.2020.10.012

[42] Jin, J.-Y., Gu, A., Wang, W., Oleinick, N. L., Machtay, M., et al. (2020). Ultra-high dose rate effect on circulating immune cells: A potential mechanism for flash effect? *Radiotherapy and Oncology*, *149*, 55–62. https://doi.org/10.1016/j.radonc.2020.04.054

[43] Konradsson, E., Liljedahl, E., Gustafsson, E., Adrian, G., Beyer, S., Ilaahi, S. E., Petersson, K., Ceberg, C., & Redebrandt, H. N. (2022). Comparable long-term tumor control for hypofractionated flash versus conventional radiation therapy in an immunocompetent rat glioma model. *Advances in Radiation Oncology*, *7*(6), 101011. https://doi.org/10.1016/j.adro.2022.101011

[44] Cunningham, S., McCauley, S., Vairamani, K., Speth, J., Girdhani, S., Abel, E., Sharma, R. A., Perentesis, J. P., Wells, S. I., Mascia, A., et al. (2021). FLASH proton pencil beam scanning irradiation minimizes radiation-induced leg contracture and skin toxicity in mice. *Cancers*, *13*(5), 1012. https://doi.org/10.3390/cancers13051012

[45] Velalopoulou, A., Karagounis, I. V., Cramer, G. M., Kim, M. M., Skoufos, G., Goia, D., Hagan, S., Verginadis, I. I., Shoniyozov, K., Chiango, J., et al. (2021). FLASH proton radiotherapy spares normal epithelial and mesenchymal tissues while preserving sarcoma response. *Cancer research*, *81*(18), 4808–4821. https://doi.org/10.1158/0008-5472.CAN-21-1500

[46] Lin, B., Huang, D., Gao, F., Yang, Y., Wu, D., Zhang, Y., Feng, G., Dai, T., & Du, X. (2022). Mechanisms of flash effect. *Frontiers in Oncology*, *12*, 995612. https://doi.org/10.3389/fonc.2022.995612

[47] Marcu, L. G., Bezak, E., Peukert, D. D., & Wilson, P. (2021). Translational research in flash radiotherapy—from radiobiological mechanisms to in vivo results. *Biomedicines*, *9*(2), 181. https://doi.org/10.3390/biomedicines9020181

[48] Bogaerts, E., Macaeva, E., Isebaert, S., & Haustermans, K. (2022). Potential molecular mechanisms behind the ultra-high dose rate "flash" effect. *Interna-*

tional Journal of Molecular Sciences, *23*(20), 12109. https://doi.org/10.3390/ijms232012109

[49] Weiss, H., Epp, E., Heslin, J., Ling, C., & Santomasso, A. (1974). Oxygen depletion in cells irradiated at ultra-high dose-rates and at conventional dose-rates. *International Journal of Radiation Biology and Related Studies in Physics, Chemistry and Medicine*, *26*(1), 17–29. https://doi.org/10.1080/09553007414550901

[50] Epp, E. R., Weiss, H., Djordjevic, B., & Santomasso, A. (1972). The radiosensitivity of cultured mammalian cells exposed to single high intensity pulses of electrons in various concentrations of oxygen. *Radiation research*, *52*(2), 324–332. https://doi.org/10.2307/3573572

[51] Jansen, J., Knoll, J., Beyreuther, E., Pawelke, J., Skuza, R., Hanley, R., Brons, S., Pagliari, F., & Seco, J. (2021). Does flash deplete oxygen? experimental evaluation for photons, protons, and carbon ions. *Medical physics*, *48*(7), 3982–3990. https://doi.org/10.1002/mp.14917

[52] Adrian, G., Konradsson, E., Beyer, S., Wittrup, A., Butterworth, K. T., McMahon, S. J., Ghita, M., Petersson, K., & Ceberg, C. (2021). Cancer cells can exhibit a sparing flash effect at low doses under normoxic in vitro-conditions. *Frontiers in oncology*, *11*, 686142. https://doi.org/10.3389/fonc.2021.686142

[53] Spitz, D. R., Buettner, G. R., Petronek, M. S., St-Aubin, J. J., Flynn, R. T., Waldron, T. J., & Limoli, C. L. (2019). An integrated physico-chemical approach for explaining the differential impact of flash versus conventional dose rate irradiation on cancer and normal tissue responses. *Radiotherapy and oncology*, *139*, 23–27. https://doi.org/10.1016/j.radonc.2019.03.028

[54] Labarbe, R., Hotoiu, L., Barbier, J., & Favaudon, V. (2020). A physicochemical model of reaction kinetics supports peroxyl radical recombination as the main determinant of the flash effect. *Radiotherapy and Oncology*, *153*, 303–310. https://doi.org/10.1016/j.radonc.2020.06.001

[55] Cooper, C. R., Jones, D. J., Jones, G. D., & Petersson, K. (2023). Comet assay profiling of flash-induced damage: Mechanistic insights into the effects of flash irradiation. *International Journal of Molecular Sciences*, *24*(8), 7195. https://doi.org/10.3390/ijms24087195

[56] Le Gal, K., Schmidt, E. E., & Sayin, V. I. (2021). Cellular redox homeostasis. *Antioxidants*, *10*(9), 1377. https://doi.org/10.3390/antiox10091377

[57] Chaiswing, L., St. Clair, W. H., & St. Clair, D. K. (2018). Redox paradox: A novel approach to therapeutics-resistant cancer. *Antioxidants & redox signaling*, *29*(13), 1237–1272. https://doi.org/10.1089/ars.2017.7485

[58] Dickinson, B. C., Tang, Y., Chang, Z., & Chang, C. J. (2011). A nuclear-localized fluorescent hydrogen peroxide probe for monitoring sirtuin-mediated oxidative stress responses in vivo. *Chemistry & biology*, *18*(8), 943–948. https://doi.org/10.1016/j.chembiol.2011.07.005

[59] Baldacchino, G., Brun, E., Denden, I., Bouhadoun, S., Roux, R., Khodja, H., & Sicard-Roselli, C. (2019). Importance of radiolytic reactions during high-let irradiation modalities: Let effect, role of o2 and radiosensitization by nanoparticles. *Cancer Nanotechnology*, *10*(1), 1–21. https://doi.org/10.1016/j.nimb.2014.11.100.

[60] Zielonka, J., Cheng, G., Zielonka, M., Ganesh, T., Sun, A., Joseph, J., Michalski, R., O'Brien, W. J., Lambeth, J. D., & Kalyanaraman, B. (2014). High-throughput assays for superoxide and hydrogen peroxide: Design of a screening workflow to identify inhibitors of nadph oxidases. *Journal of Biological Chemistry*, *289*(23), 16176–16189. https://doi.org/10.1074/jbc.M114.548693

[61] Bai, X., Ng, K. K.-H., Hu, J. J., Ye, S., & Yang, D. (2019). Small-molecule-based fluorescent sensors for selective detection of reactive oxygen species in biological systems. *Annual Review of Biochemistry*, *88*, 605–633. https://doi.org/10.1146/annurev-biochem-013118-111754

[62] Nabbi, A., & Riabowol, K. (2015). Rapid isolation of nuclei from cells in vitro. *Cold Spring Harbor Protocols*, *2015*(8), pdb–prot083733. https://doi.org/10.1101/pdb.prot083733

[63] Hanley, R., Pagliari, F., Garcia-Calderón, D., Fernandes Guerreiro, J., Genard, G., Jansen, J., Nisticò, C., Marafioti, M. G., Tirinato, L., & Seco, J. (2023). Radio-resistance of hypoxic tumors: Exploring the effects of oxygen and x-ray radiation on non-small lung cancer cell lines. *Radiation Oncology*, *18*(1), 81. https://doi.org/10.1186/s13014-023-02275-8

[64] Pastina, B., & LaVerne, J. A. (1999). Hydrogen peroxide production in the radiolysis of water with heavy ions. *The Journal of Physical Chemistry A*, *103*(11), 1592–1597. https://doi.org/10.1021/jp984433o

[65] Wasselin-Trupin, V., Baldacchino, G., Bouffard, S., & Hickel, B. (2002). Hydrogen peroxide yields in water radiolysis by high-energy ion beams at constant let. *Radiation Physics and Chemistry*, *65*(1), 53–61. https://doi.org/10.1016/S0969-806X(01)00682-X

[66] Muñoz, I. D., Burigo, L. N., Gehrke, T., Brons, S., Greilich, S., & Jäkel, O. (2023). Sensitivity correction of fluorescent nuclear track detectors using alpha particles: Determining let spectra of light ions with enhanced accuracy. *Medical Physics*, *50*(4), 2385–2401. https://doi.org/10.1002/mp.16083

[67] Muñoz, I. D., Garcia-Calderon, D., Félix-Bautista, R., Burigo, L. N., Christensen, J. B., Brons, S., Runz, A., Häring, P., Greilich, S., Seco, J., & Jäkel, O. (2024, In Press). Linear energy transfer measurements and estimation of relative biological effectiveness in proton and helium-ion beams using fluorescent nuclear track detectors. *International Journal of Radiation Oncology Biology Physics*.

[68] Theodoridou, E. (2023). *"backscattering effect on flash dosimetry for filtered and no-filtered x-ray beam* [Bachelor Thesis]. Aristotle University of Thessaloniki.

[69] Di Martino, F., Barca, P., Barone, S., Bortoli, E., Borgheresi, R., De Stefano, S., Di Francesco, M., Grasso, L., Linsalata, S., Marfisi, D., et al. (2020). Flash radiotherapy with electrons: Issues related to the production, monitoring, and dosimetric characterization of the beam. *Frontiers in Physics*, *8*, 570697. https://doi.org/10.3389/fphy.2020.570697

[70] *Atn-224 product sheet*. (n.d.). Chayman Chemical. https://cdn.caymanchem.com/cdn/insert/23553.pdf

[71] von Samson Himmelstierna, M. J. (2023). *An in vitro investigation of a proposed enzymatic flash mechanism employing x-ray irradiation of non-small-cell lung cancer cell lines* [Master Thesis]. Heidelberg University.

[72] *19160 sod determination kit*. (n.d.). Sigma-Aldrich. https://www.sigmaaldrich.com/deepweb/assets/sigmaaldrich/product/documents/254/301/19160dat.pdf

[73] Batkai, B. (2023). *Comparison of H_2O_2 concentration in nuclei supernatant between high dose rate and conventional dose rate x-ray irradiation* [Bachelor Thesis]. Heidelberg University.

[74] Ettinger, D. S., Akerley, W., Bepler, G., Blum, M. G., Chang, A., Cheney, R. T., Chirieac, L. R., D'Amico, T. A., Demmy, T. L., Ganti, A. K. P., et al. (2010). Non-small cell lung cancer. *Journal of the national comprehensive cancer network*, *8*(7), 740–801. https://doi.org/10.6004/jnccn.2010.0056

[75] Bruce, W., Pearson, M., & Freedhoff, H. S. (1963). The linear energy transfer distributions resulting from primary and scattered x-rays and gamma rays with primary hvl's from 1.25 mm cu to 11 mm pb. *Radiation Research*, *19*(4), 606–620. https://doi.org/10.2307/3571481

[76] Howard, M. E., Beltran, C., Anderson, S., Tseung, W. C., Sarkaria, J. N., & Herman, M. G. (2017). Investigating dependencies of relative biological effectiveness for proton therapy in cancer cells. *International journal of particle therapy*, *4*(3), 12–22. https://doi.org/10.14338/IJPT-17-00031.1

[77] Kacem, H., Psoroulas, S., Boivin, G., Folkerts, M., Grilj, V., Lomax, T., Martinotti, A., Meer, D., Ollivier, J., Petit, B., et al. (2022). Comparing radiolytic production of h2o2 and development of zebrafish embryos after ultra high dose rate exposure with electron and transmission proton beams. *Radiotherapy and oncology*, *175*, 197–202. https://doi.org/10.1016/j.radonc.2022.07.011

[78] Agarwal, A., & Bui, A. D. (2017). Oxidation-reduction potential as a new marker for oxidative stress: Correlation to male infertility. *Investigative and clinical urology*, *58*(6), 385–399. https://doi.org/10.4111/icu.2017.58.6.385

[79] Suslow, T. V. (2004). *Oxidation-reduction potential (orp) for water disinfection monitoring, control, and documentation*. https://doi.org/10.3733/ucanr.8149

[80] Hwang, C., & Sinskey, A. J. (1991). The role of oxidation-reduction potential in monitoring growth of cultured mammalian cells. In *Production of biologicals from animal cells in culture* (pp. 548–568). Elsevier. https://doi.org/10.1016/B978-0-7506-1103-9.50104-9

[81] Kjaergaard, L., & Joergensen, B. (1981). The redox potential, a hitherto seldom used parameter in fermentation systems. In *Scientific and engineering principles* (pp. 371–376). Elsevier. https://doi.org/10.1016/B978-0-08-025383-1.50067-9

[82] Juarez, J. C., Betancourt Jr, O., Pirie-Shepherd, S. R., Guan, X., Price, M. L., Shaw, D. E., Mazar, A. P., & Doñate, F. (2006). Copper binding by tetrathiomolybdate attenuates angiogenesis and tumor cell proliferation through the inhibition of superoxide dismutase 1. *Clinical Cancer Research*, *12*(16), 4974–4982. https://doi.org/10.1158/1078-0432.CCR-06-0171

[83] Juarez, J. C., Manuia, M., Burnett, M. E., Betancourt, O., Boivin, B., Shaw, D. E., Tonks, N. K., Mazar, A. P., & Doñate, F. (2008). Superoxide dismutase 1 (sod1) is essential for h2o2-mediated oxidation and inactivation of phosphatases in growth factor signaling. *Proceedings of the National Academy of Sciences*, *105*(20), 7147–7152. https://doi.org/10.1073/pnas.0709451105

[84] Khan, M. K., Miller, M. W., Taylor, J., Gill, N. K., Dick, R. D., Van Goled, K., Brewert, G. J., & Merajver, S. D. (2002). Radiotherapy and antiangiogenic tm in lung cancer. *Neoplasia*, *4*(2), 164–170. https://doi.org/10.1038/sj.neo.7900218

[85] Cox, C., Teknos, T. N., Barrios, M., Brewer, G. J., Dick, R. D., & Merajver, S. D. (2001). The role of copper suppression as an antiangiogenic strategy in head and neck squamous cell carcinoma. *The Laryngoscope*, *111*(4), 696–701. https://doi.org/10.1097/00005537-200104000-00024

[86] Pan, Q., Kleer, C. G., van Golen, K. L., Irani, J., Bottema, K. M., Bias, C., De Carvalho, M., Mesri, E. A., Robins, D. M., Dick, R. D., et al. (2002). Copper deficiency induced by tetrathiomolybdate suppresses tumor growth and angiogenesis. *Cancer research*, *62*(17), 4854–4859. https://aacrjournals.org/cancerres/article-pdf/62/17/4854/2496292/ch1702004854.pdf

[87] Hanley, R. (2022). *Radio-resistance of hypoxic tumours: The effects of oxygen and radiation on cancer cell metabolism, oxidative stress, and dna repair* [PhD Thesis]. Heidelberg University. https://doi.org/10.11588/heidok.00031345

[88] Kang, M., Kim, H., Piao, C., Lee, K., Hyun, J., Chang, I., & You, H. (2013). The critical role of catalase in prooxidant and antioxidant function of p53. *Cell Death & Differentiation*, *20*(1), 117–129. https://doi.org/10.1038/cdd.2012.102

[89] Dahm-Daphi, J., Sass, C., & Alberti, W. (2000). Comparison of biological effects of dna damage induced by ionizing radiation and hydrogen peroxide in cho cells. *International journal of radiation biology*, *76*(1), 67–75. https://doi.org/10.1080/095530000139023

[90] Cannan, W. J., Tsang, B. P., Wallace, S. S., & Pederson, D. S. (2014). Nucleosomes suppress the formation of double-strand dna breaks during attempted base excision repair of clustered oxidative damages. *Journal of Biological Chemistry*, *289*(29), 19881–19893. https://doi.org/10.1074/jbc.M114.571588

[91] Rothkamm, K., & Lobrich, M. (2002). Misrepair of radiation-induced dna double-strand breaks and its relevance for tumorigenesis and cancer treatment. *International journal of oncology*, *21*(2), 433–440. https://doi.org/10.3892/ijo.21.2.433

[92] Olive, P. L. (1998). The role of dna single-and double-strand breaks in cell killing by ionizing radiation. *Radiation research*, *150*(5s), S42–S51. https://doi.org/10.2307/3579807

[93] Schwarz, H. A., Caffrey Jr, J. M., & Scholes, G. (1959). Radiolysis of neutral water by cyclotron produced deuterons and helium ions1. *Journal of the American Chemical Society*, *81*(8), 1801–1809. https://doi.org/10.1021/ja01517a008

[94] Burns, W. G., & Sims, H. E. (1981). Effect of radiation type in water radiolysis. *Journal of the Chemical Society, Faraday Transactions 1: Physical Chemistry in Condensed Phases*, *77*(11), 2803–2813. https://doi.org/10.1039/F19817702803

[95] Samuel, A. H., & Magee, J. L. (1953). Theory of radiation chemistry. ii. track effects in radiolysis of water. *The Journal of Chemical Physics*, *21*(6), 1080–1087. https://doi.org/10.1063/1.1699113

[96] Richter, C., Pawelke, J., Karsch, L., & Woithe, J. (2009). Energy dependence of ebt-1 radiochromic film response for photon and electron beams readout by a flatbed scanner. *Medical physics*, *36*(12), 5506–5514. https://doi.org/10.1118/1.3253902

[97] Massillon-JL, G., Chiu-Tsao, S.-T., Domingo-Munoz, I., & Chan, M. F. (2012). Energy dependence of the new gafchromic ebt3 film: Dose response curves for 50 kv, 6 and 15 mv x-ray beams. https://doi.org/10.4236/ijmpcero.2012.12008

[98] Khachonkham, S., Dreindl, R., Heilemann, G., Lechner, W., Fuchs, H., Palmans, H., Georg, D., & Kuess, P. (2018). Characteristic of ebt-xd and ebt3 radiochromic film dosimetry for photon and proton beams. *Physics in Medicine & Biology*, *63*(6), 065007. https://doi.org/10.1088/1361-6560/aab1ee

[99] Ankerhold, U. (2000). Catalogue of x-ray spectra and their characteristic data-iso and din radiation qualities, therapy and diagnostic radiation qualities, unfiltered x-ray spectra. https://doi.org/10.7795/110.20190315B

[100] Hubbell, J., & Seltzer, S. M. (n.d.). X-ray mass attenuation coefficients. *NIST Standard Reference Database 126*. https://doi.org/10.18434/T4D01F

[101] Seong, K. M., Kim, C. S., Jeon, H. Y., Oh, S.-H., Nam, S. Y., Yang, K. H., Kim, J.-Y., & Jin, Y.-W. (2010). Intrinsic radiosensitivity correlated with radiation-induced ros and cell cycle regulation. *Molecular & cellular toxicology*, *6*(1), 1–7. https://doi.org/10.1007/s13273-010-0001-x

[102] Srinivas, U. S., Tan, B. W., Vellayappan, B. A., & Jeyasekharan, A. D. (2019). Ros and the dna damage response in cancer. *Redox biology*, *25*, 101084. https://doi.org/10.1016/j.redox.2018.101084

[103] Kjaergaard, L. (2006). The redox potential: Its use and control in biotechnology. *Advances in Biochemical Engineering, Volume 7*, 131–150. https://doi.org/10.1007/BFb0048444

[104] Winterbourn, C. C., & Hampton, M. B. (2008). Thiol chemistry and specificity in redox signaling. *Free Radical Biology and Medicine*, *45*(5), 549–561. https://doi.org/10.1016/j.freeradbiomed.2008.05.004

[105] Zitka, O., Skalickova, S., Gumulec, J., Masarik, M., Adam, V., Hubalek, J., Trnkova, L., Kruseova, J., Eckschlager, T., & Kizek, R. (2012). Redox status expressed as gsh: Gssg ratio as a marker for oxidative stress in paediatric tumour patients. *Oncology letters*, *4*(6), 1247–1253. https://doi.org/10.3892/ol.2012.931

[106] Heales, J., Harrett, A., & Blake, S. (1998). Timer error and beam quality variation during" ramp-up" of a superficial x-ray therapy unit. *The British Journal of Radiology*, *71*(852), 1306–1309. https://doi.org/10.1259/bjr.71.852.10319006

[107] Adrian, G., Ruan, J.-L., Paillas, S., Cooper, C. R., & Petersson, K. (2022). In vitro assays for investigating the flash effect. *Expert Reviews in Molecular Medicine*, *24*, e10. https://doi.org/10.1017/erm.2022.5

[108] Adrian, G., Konradsson, E., Lempart, M., Bäck, S., Ceberg, C., & Petersson, K. (2020). The flash effect depends on oxygen concentration. *The British journal of radiology*, *92*(1106), 20190702. https://doi.org/10.1259/bjr.20190702

[109] Town, C. (1967). Effect of high dose rates on survival of mammalian cells. *Nature*, *215*(5103), 847–848. https://doi.org/10.1038/215847a0

[110] Tessonnier, T., Mein, S., Walsh, D. W., Schuhmacher, N., Liew, H., Cee, R., Galonska, M., Scheloske, S., Schömers, C., Weber, U., et al. (2021). Flash dose rate helium ion beams: First in vitro investigations. *International Journal of Radiation Oncology* Biology* Physics*, *111*(4), 1011–1022. https://doi.org/10.1016/j.ijrobp.2021.07.1703

[111] Kacem, H., Almeida, A., Cherbuin, N., & Vozenin, M.-C. (2022). Understanding the flash effect to unravel the potential of ultra-high dose rate irradiation. *International journal of radiation biology*, *98*(3), 506–516. https://doi.org/10.1080/09553002.2021.2004328

[112] Vozenin, M.-C., Hendry, J. H., & Limoli, C. (2019). Biological benefits of ultra-high dose rate flash radiotherapy: Sleeping beauty awoken. *Clinical oncology*, *31*(7), 407–415. https://doi.org/10.1080/09553002.2021.2004328

[113] Wilson, J. D., Hammond, E. M., Higgins, G. S., & Petersson, K. (2020). Ultra-high dose rate (flash) radiotherapy: Silver bullet or fool's gold? *Frontiers in oncology*, *9*, 1563. https://doi.org/10.3389/fonc.2019.01563

[114] Cecchi, D. D., Therriault-Proulx, F., Lambert-Girard, S., Hart, A., Macdonald, A., Pfleger, M., Lenckowski, M., & Bazalova-Carter, M. (2021). Characterization of an x-ray tube-based ultrahigh dose-rate system for in vitro irradiations. *Medical Physics*, *48*(11), 7399–7409. https://doi.org/10.1002/mp.15234

[115] Rezaee, M., Iordachita, I., & Wong, J. W. (2021). Ultrahigh dose-rate (flash) x-ray irradiator for pre-clinical laboratory research. *Physics in Medicine & Biology*, *66*(9), 095006.

[116] Andrés, C. M. C., Pérez de la Lastra, J. M., Andrés Juan, C., Plou, F. J., & Pérez-Lebeña, E. (2023). Superoxide anion chemistry—its role at the core of the innate immunity. *International Journal of Molecular Sciences*, *24*(3), 1841. https://doi.org/10.3390/ijms24031841

[117] Bokare, A. D., & Choi, W. (2014). Review of iron-free fenton-like systems for activating h2o2 in advanced oxidation processes. *Journal of hazardous materials*, *275*, 121–135. https://doi.org/10.1016/j.jhazmat.2014.04.054

[118] Sies, H. (1997). Oxidative stress: Oxidants and antioxidants. *Experimental Physiology: Translation and Integration*, *82*(2), 291–295. https://doi.org/10.1113/expphysiol.1997.sp004024

[119] Wang, Q., Chen, W., Bai, L., Chen, W., Padilla, M. T., Lin, A. S., Shi, S., Wang, X., & Lin, Y. (2014). Receptor-interacting protein 1 increases chemoresistance by maintaining inhibitor of apoptosis protein levels and reducing reactive oxygen species through a microrna-146a-mediated catalase pathway. *Journal of Biological Chemistry*, *289*(9), 5654–5663. https://doi.org/10.1074/jbc.M113.526152

[120] Pawelke, J., Brand, M., Hans, S., Hideghéty, K., Karsch, L., Lessmann, E., Löck, S., Schürer, M., Szabó, E. R., & Beyreuther, E. (2021). Electron dose rate and oxygen depletion protect zebrafish embryos from radiation damage. *Radiotherapy and Oncology*, *158*, 7–12. https://doi.org/10.1016/j.radonc.2021.02.003

[121] Butson, M. J., Peter, K., Cheung, T., & Metcalfe, P. (2003). Radiochromic film for medical radiation dosimetry. *Materials Science and Engineering: R: Reports*, *41*(3-5), 61–120. https://doi.org/10.1016/S0927-796X(03)00034-2

[122] Devic, S., Seuntjens, J., Sham, E., Podgorsak, E. B., Schmidtlein, C. R., Kirov, A. S., & Soares, C. G. (2005). Precise radiochromic film dosimetry using a flat-bed document scanner. *Medical physics*, *32*(7Part1), 2245–2253.

[123] Szpala, S., Huang, V., Zhao, Y., Kyle, A., Minchinton, A., Karan, T., & Kohli, K. (2021). Dosimetry with a clinical linac adapted to flash electron beams. *Journal of Applied Clinical Medical Physics*, *22*(6), 50–59. https://doi.org/10.1002/acm2.13270

[124] Niroomand-Rad, A., Chiu-Tsao, S.-T., Grams, M. P., Lewis, D. F., Soares, C. G., Van Battum, L. J., Das, I. J., Trichter, S., Kissick, M. W., Massillon-JL, G., et al. (2020). Report of AAPM task group 235 radiochromic film dosimetry: An update to TG-55. *Medical physics*, *47*(12), 5986–6025. https://doi.org/10.1002/mp.14497

[125] Arráns, R., Miras, H., Ortiz-Seidel, M., Terrón, J., Macías, J., & Ortiz-Lora, A. (2009). Dosimetría con películas radiocrómicas. *Rev Fis Med*, *10*(2), 83–104.

[126] Schindelin, J., Arganda-Carreras, I., Frise, E., Kaynig, V., Longair, M., Pietzsch, T., Preibisch, S., Rueden, C., Saalfeld, S., Schmid, B., et al. (2012). Fiji: An open-source platform for biological-image analysis. *Nature methods*, *9*(7), 676–682. https://doi.org/10.1038/nmeth.2019

[127] *Absorbed dose determination in external beam radiotherapy.* (2001). INTERNATIONAL ATOMIC ENERGY AGENCY. https://www.iaea.org/publications/5954/absorbed-dose-determination-in-external-beam-radiotherapy

[128] Devic, S., Tomic, N., & Lewis, D. (2016). Reference radiochromic film dosimetry: Review of technical aspects. *Physica Medica*, *32*(4), 541–556. https://doi.org/10.1016/j.ejmp.2016.02.008

[129] Ma, C.-M., Coffey, C., DeWerd, L., Liu, C., Nath, R., Seltzer, S., & Seuntjens, J. (2001). AAPM protocol for 40–300 kv x-ray beam dosimetry in radiotherapy and radiobiology. *Medical physics*, *28*(6), 868–893. https://doi.org/10.1118/1.1374247

[130] Xue, L.-Y., Friedman, L., Oleinick, N., & Chiu, S.-M. (1994). Induction of DNA damage in γ-irradiated nuclei stripped of nuclear protein classes: Differential modulation of double-strand break and dna—protein crosslink formation. *International journal of radiation biology*, *66*(1), 11–21. https://doi.org/10.1080/09553009414550901

[131] Frankenberg-Schwager, M. (1989). Review of repair kinetics for dna damage induced in eukaryotic cells in vitro by ionizing radiation. *Radiotherapy and Oncology*, *14*(4), 307–320. https://doi.org/10.1016/0167-8140(89)90143-6

[132] de Laat, W. L., Jaspers, N. G., & Hoeijmakers, J. H. (1999). Molecular mechanism of nucleotide excision repair. *Genes & development*, *13*(7), 768–785.

Acknowledgments

First, I would like to thank my supervisor, Prof. Dr. Joao Seco, for giving me the opportunity to work at the DKFZ's Biomedical Physics in Radiation Oncology group.

I am sincerely thankful to Prof. Dr. Christian Karger for revising this work and for being part of my Thesis Advisor Committee (TAC). On the same note, thanks to Dr. Michael Hausmann and Dr. Francesca Pagliari for being part of my TAC.

Special thanks to Dr. Francesca Pagliari and Dr. Géraldine Genard for your guidance and support throughout all the stages of this project. Thank you also for all your advice and words of encouragement.

Thanks to all the people at the Biomedical Physics in Radiation Oncology group and the REZ building for the friendly and welcoming working environment. Especially to all my PhD-colleagues with whom I've had the honor of sharing this experience. I am avoiding writing a list of names since I am terribly afraid of missing a name. Please believe me when I say everyone has a special place in my life.

I want to thank all the Master's and Bachelor's students I've had worked with. I hope that I was good enough to leave some knowledge behind. I've definitely learned a lot in the past years working with all of you.

On a more personal note, this part of my life would not be complete without Gabriela. Thanks for all the support and care for all of these years. Thanks to my family for cheering from the distance.

Finally, this work was only possible thanks to the economic support of the DAAD: German Academic Exchange Service under the Graduate School Scholarship Programme, 2019 (57450037).